NASA JSC-09241
ERIM 102800-40-F

NASA CR-
141690

Final Report

MULTISPECTRAL SCANNER DATA APPLICATIONS EVALUATION

Volume II — Sensor System Study

Honeywell Radiation Center

DECEMBER 1974

Prepared for

NATIONAL AERONAUTICS AND SPACE ADMINISTRATION

Lyndon B. Johnson Space Center
NAS9-13386-CCA2
M. J. Harnage

ENVIRONMENTAL
RESEARCH INSTITUTE OF MICHIGAN
FORMERLY WILLOW RUN LABORATORIES, THE UNIVERSITY OF MICHIGAN
BOX 618 • ANN ARBOR • MICHIGAN 48107

NOTICE

Sponsorship. The work reported herein was conducted by the Environmental Research Institute of Michigan for the National Aeronautics and Space Administration, Johnson Space Center, Houston, Texas 77058, under Contract NAS9-13386-CCA2. Mr. M. Jay Harnage was Project Manager. Contracts and grants to the Institute for the support of sponsored research are administered through the Office of Contracts Administration.

Availability Notice. Requests for copies of this report should be referred to:

National Aeronautics and Space Administration
Scientific and Technical Information Facility
P.O. Box 33
College Park, Maryland 20740

FINAL REPORT

SENSOR SYSTEM STUDY

Prepared for

Environmental Research Institute of Michigan

by

Honeywell Radiation Center
2 Forbes Road
Lexington, Massachusetts 02173

FOREWORD

This report describes part of a comprehensive program concerned with advancing the state-of-the-art in remote sensing of the environment from aircraft and satellite. The research was carried out for the National Aeronautics and Space Administration's Lyndon B. Johnson Space Center, Houston, Texas by the Environmental Research Institute of Michigan (ERIM), Ann Arbor, Michigan, and by the Honeywell Radiation Center, Lexington, Massachusetts.

The Multispectral Scanner Data Applications Study consisted of two tasks: task 1, a User Application Study reported in Volume I; and task 2, the Sensor System Study, reported herein. The integrated results of tasks 1 and 2 are presented in an Executive Summary, published as a separate document.

TABLE OF CONTENTS

SECTION 1

INTRODUCTION AND SUMMARY

Generally, any earth orbiting data collecting instrument represents a compromise between the performance desired by the scientific and/or user community and the hardware limitations due to state-of-the-art technology, launch capabilities and funding levels.

This report presents data developed by the Honeywell Radiation Center, Lexington, Massachusetts, under Honeywell Subcontract No. 1 to the Environmental Research Institute of Michigan (ERIM) required for cost vs benefit studies to define a multispectral thematic mapper for earth resources applications. This effort is in support of ERIM under NASA/JSC Contract No. NAS9-13386.

At the inception of the contract, the objective was to define one or more instruments that would be capable of meeting the user data requirements. During the course of the contract it became obvious that establishing a commonality of requirements among the various prospective users was considerably more difficult than anticipated. Accordingly, the study objective was modified. Instead of presenting completely defined instruments, various parametric charts were developed. These charts allow the reader to assess the impact on instrument design of the various user requirements. In addition, discussions of state-of-the-art technology in various areas critical to the design of a multispectral radiometer are presented in a set of appendixes.

The requisite information was developed in the following manner. First, a baseline instrument was developed. To do this, each of the three EOS point design instruments were analyzed in detail to determine whether it met the baseline performance specification set forth in "GSFC Specification for an Earth Observation Scanning Spectro-Radiometer Experiment (SSR)", GSFC 73-15012, March 1973. Critical or high risk areas in each design were identified to determine whether new technology would have to be developed for the instrument to meet the stated performance requirements. The final conclusion of this activity was that each design was capable of meeting the baseline performance specification without new technology. The conical image plane scanner exhibited the least mechanical complexity while the linear image plane scanner produced a scan pattern most nearly resembling the current ERTS scan pattern. The object plane scanner had the largest telescope entrance pupil collecting area (for the given dimensional constraints of 36 inches x 36 inches x 78 inches) as well as the greatest potential for a high resolution thermal band.

The second phase of the program was to characterize a representative radiometer to serve as a baseline for the generation of performance tradeoff curves. This was done by averaging instrument parameters for the three EOS point design instruments to arrive at a value for the hypothetical instrument. A system performance equation was developed and tradeoff curves generated for the hypothetical instrument. A set of worst case (most demanding) performance specifications were obtained from ERIM and overlaid on the performance curves. The results indicate that there would be considerable impact on instrument design if the worst case specifications are indeed representative of user community needs.

The third phase of the study was to examine critical areas of technology to predict the probable state-of-the-art in the 1977-78 time period. The one technology bearing most heavily on multispectral radiometer design is that of detector performance. This is especially true as the number of detectors per spectral band is increased to improve instrument sensitivity.

Charge-coupled linear arrays offer considerable potential in reducing electronic and packaging complexities. Hybrid arrays consisting of infrared detector arrays coupled to CCD shift registers will be a viable alternative to hard-wired infrared arrays within several years and will reduce the heatloading and interference problems associated with detectors for the near and far infrared.

Finally, based on the results of the tradeoff analysis activity, a pushbroom multispectral radiometer was configured to assess the practicality of such an instrument. Currently, there are several unsolved problems associated with optical design and low frequency radiometric stability (dc restoration) as well as the large number of detectors required per spectral band. The rapid evolution of CCD technology could solve the detector problem with the pushbroom configuration becoming an attractive alternative to the scanning radiometer for the thematic mapper application.

This report was prepared under the cognizance and general guidance of John G. N. Braithwaite of the Environmental Research Institute of Michigan and his assistance in providing needed information and his support are gratefully acknowledged.

SECTION 2

TRADEOFF ANALYSIS

Optimization of a data acquisition system such as the Thematic Mapper for the earth resources application requires some index of cost vs performance against which the requirements of the user community can be evaluated. In Section 2.2 a series of performance tradeoff charts are developed and in Section 2.3 the cost impact is presented. Section 2.1 presents a set of baseline radiances and performance levels on which the trade-off charts of Section 2.2 are based. Section 2.4 discusses other aspects of the influence of user requirements on instrument performance.

2.1 BASELINE RADIANCE LEVELS

As will be shown in the following section the radiometric performance of a radiometer is a function of the radiance level. Accordingly it is necessary to have a baseline set of radiance levels to be used during the generation of performance trade-off charts. Selection of a suitable set of radiance levels is not a trivial task for various reasons, not the least of which is the fact that the actual parameter of interest to the user community is the reflectivity at certain wavelengths of the material being observed. The radiance observed by a radiometer is a function of viewing conditions such as local weather, time of day and year, and atmospheric scattering, as well as the reflectivity of the viewed material. To scope the potential magnitude of the impact of user requirements on radiometer design, it was decided to work with worst case conditions. Accordingly, ERIM supplied a set of radiances, spectral bands, and noise equivalent radiances (NEL). The NEL is a minimum detectable change in radiance and is a good indicator of radiometric performance. Included in the ERIM data were two cases which represented the most demanding requirements for two potential orbits. Two values of NEL were supplied corresponding to a desired NEL and a maximum acceptable NEL. This information is tabulated in Table 1. The spectral bands, radiances, and noise equivalent radiances specified in the EOS point design specification (GSFC 73-15012) are included for reference.

There are several points that are immediately obvious when one compares the worst case performance requirements with the EOS requirements. One point is that the number of spectral bands required to satisfy the requirements of the majority of potential users has increased from seven to eleven. This implies an increase in detector count and data bandwidth by a factor of 1.57 if all other para-

TABLE 1

COMPARISON OF EOS AND ERIM WORST CASE RADIANCES
(all radiances in milliwatts/cm^2-steradian-micron)

EOS Point Design Radiances

Spectral Band $\lambda_1 - \lambda_2$ (μm)	Minimum Radiance min	Noise Equivalent Radiance NEL
0.5 - 0.6	2.2	0.22
0.6 - 0.7	1.9	0.25
0.7 - 0.8	1.6	0.32
0.8 - 1.1	1.0	0.20
1.55 - 1.75	0.4	0.09
2.1 - 2.35	0.12	0.02
10.4 - 12.6	300 KBB	0.5°K

ERIM Worst Case Radiances
(22 December 30° Latitude)

Spectral Band $\lambda_1 - \lambda_2$ (μm)	0930 Hrs Orbit Radiance, L		Noise Equivalent Radiance		1200 Hrs Orbit Radiance, L		Noise Equivalent Radiance	
	Maximum	Minimum	Desirable	Acceptable	Maximum	Minimum	Desirable	Acceptable
0.42 - 0.48	9.35	4.79	.017	.042	24.86	4.54	.024	.061
0.48 - 0.52	10.32	4.80	.024	.061	21.57	3.97	.035	.087
0.50 - 0.54	8.81	4.19	.025	.099	18.65	3.70	.035	.142
0.52 - 0.58	21.45	3.68	.025	.063	32.47	3.27	.036	.090
0.58 - 0.64	7.21	2.59	.026	.026	12.22	2.48	.037	.037
0.62 - 0.68	20.27	2.22	.025	.064	27.28	2.14	.036	.090
0.69 - 0.74	9.98	1.61	.024	.060	15.08	1.70	.033	.084
0.80 - 1.1	10.74	1.10	.031	.061	18.73	1.09	.058	.115
1.55 - 1.75	4.71	1.43	.011	.011	6.31	0.68	.022	.022
2.0 - 2.3	1.44	0.11	.004	.008	1.78	0.12	.007	.013
10.4 - 12.4	340°K BB	250°K BB	0.25°K	1.0°K	340°K BB	250°K BB	0.25°K	1.0°K

meters are held constant. Another point is that the spectral bandwidths are narrower; therefore, the radiant power within a given band has been reduced by a factor of up to 2.5. For example, the power in the 0.50-0.54 micron band is about 40% of the power in the 0.5-0.6 micron band. Still another point of difference is that the NEL's decrease by an order of magnitude.

The relative difficulty of achieving the desired performance in each of the spectral bands between 0.4 and 2.3 micron can be determined by taking the product of the spectral bandwidth, the noise equivalent radiance, system transmission, and detector responsivity to arrive at a relative noise equivalent current. Table 2 presents the results of this calculation in normalized form. The optical system transmission was considered independent of wavelength except at the blue end of the spectrum (0.42-0.48 micron) where the reflectivity of the enhanced silver coating commonly used on mirrors decreases rapidly. The detector responsivities are characteristic of silicon for the 0.42-1.1 micron region and InSb for the 1.65 and 2.2 micron bands. The high quantum efficiency of silicon results in better performance than achievable with photomultiplier tubes for the radiances listed in Table 1.

It can be seen from the last column in Table 2 that the signal current for Band 1 (0.42-0.48 micron) is only half the value of the current for the 0.48-0.52 micron band. This means that an instrument designed to provide the desired performance in the 0.42-0.48 micron band would require between 40% and 100% more optical collecting area than an instrument designed to provide the desired performance in the 0.48-0.52 micron band but not the 0.42-0.48 micron band. Scanning the balance of the last column, it can be seen that the 0.48-0.52 micron band is the second most difficult band for meeting the desired performance. It was decided to generate performance tradeoff charts for both Band 2 (0.48-0.52 micron) and Band 1 (0.42-0.48 micron). This would allow the assessment of the added cost of achieving performance in the 0.42-0.48 micron band.

2.2 PERFORMANCE TRADEOFF ANALYSIS

The smallest difference in the reflectivity ($NE\Delta\rho$) of an observed material that can be sensed by a radiometer is determined by the irradiance of the material, the viewing geometry, and the various noise sources associated with the radiometer. Of these three

Table 2

REQUIRED PERFORMANCE EVALUATION

Spectral Band $\lambda_1 - \lambda_2$ (μm)	Bandwidth $\Delta\lambda$ (μm)	NEL mW/cm^2-sr-μm)	Transmission τ_o	Detector Responsivity R_λ (AW^{-1})	Normalized Current
0.42 - 0.48	.06	.017	.23	.22	1
0.48 - 0.52	.04	.024	.35	.30	1.9
0.50 - 0.54	.04	.025	.35	.31	2.1
0.52 - 0.58	.06	.025	.35	.33	3.3
0.58 - 0.64	.06	.026	.35	.35	3.7
0.62 - 0.68	.06	.025	.35	.38	3.8
0.69 - 0.74	.05	.024	.35	.42	3.4
0.8 - 1.1	.30	.031	.35	.23	14.4
1.55 - 1.75	.20	.011	.35	.65	9.6
2.0 - 2.3	.30	.004	.35	.89	7.2

variables, the first and second are determined by the properties of the sun and atmosphere, the geographical location of the viewed material, and the time of day and year. Limited control over these parameters can be had by varying the orbital properties such as altitude and time of day (e.g., an 0930 vs a 1200 hrs orbit). Ultimately, the instrument parameters have to be adjusted to reduce the noise sources associated with the radiometer to a point where the noise power is no larger than the change in radiant power resulting from a change in reflectivity corresponding to the desired $NE\Delta\rho$. This section discusses the various noise sources and relates a measure of noise power, the instrument noise equivalent radiance (NEL), to various instrument and orbital parameters.

The NEL of a radiometer is defined as that change in radiance which would produce a change in output signal just equal to the rms noise associated with the output signal. Thus the NEL is equal to the radiance divided by the output peak signal to rms noise ratio. This ratio is equal to the signal to noise ratio (S/N) at the output of the preamplifier for a properly designed radiometer. The signal level is determined by various instrument parameters and is given in Equation 2.1

$$I_s = RL\Delta\lambda A\alpha^2\tau_o\gamma \qquad (2.1)$$

where

I_s = signal current

R = detector responsibility (amperes/watt)

L = apparent scene radiance (W/cm^2 steradian micron)

$\Delta\lambda$ = spectral bandwidth (micron)

A = effective telescope collecting area (cm^2)

α = nominal angular instantaneous field of view (radians)

τ_o = optical transmission including filters, etc.

γ = ratio of nominal IFOV to the field of view subtended by the detector active area (often referred to as capture efficiency)

The value of α is equal to the ground resolved distance divided by the line-of-sight distance to the ground (h).

here are three general sources of noise associated with a well esigned radiometer·

1. The statistical variation in the photon flux inpinging on the detector.

2. Noise mechanism associated with the detector such as thermal (Johnson) noise.

3. Noise associated with the detector preamplifier.

hese various noise sources have been discussed in detail in the arious EOS point design study reports and only the results will e reproduced here in a form suitable for the generation of the radeoff charts. The noise current associated with a photovoltaic etector and associated preamplifier is given by:

$$I_n = f_n^{1/2}\left[(5.65\ V_A\ C_T\ f_n)^2 + \frac{4kT}{R} + 2eI_s + I_d^2 + I_A^2\right]^{1/2} \qquad (2.2)$$

here

I_n = rms noise current within the band defined by f_n

f_n = equivalent noise bandwidth (Hertz)

V_A = equivalent noise voltage per root Hertz of the pre-amplifier (V/Hz)

C_T = the total shunt capacitance at the input to the preamplifier (farad)

k = Boltzmann's constant

T = temperature in degrees Kelvin

R = equivalent shunt resistance at the input to the preamplifier (ohms)

e = electronic charge (coulomb)

I_s = signal current as defined by Equation 2.1 (Amperes)

I_D = equivalent detector noise current per root Hertz (Amperes/Hertz)

I_A = preamplifier equivalent input noise current per root Hertz (amperes/Hertz$^{1/2}$)

The equivalent noise bandwidth is given by

$$f_n = \frac{0.635\ W\ v}{\eta n\ (GRD)^2} \qquad (2.3)$$

where

W = ground swath width (kilometers)

v = velocity of the nadir point (km/second)

η = scan efficiency

n = number of lines scanned in parallel

GRD = ground resolved distance (the linear distance on the ground corresponding to the nominal IFOV)

The constant 0.635 is based on a second order Butterworth filter with the corner frequency adjusted to given an 80% response at the temporal frequency corresponding to the spatial frequency of one cycle per two (IFOV). The value of n is equal to the number of detectors per spectral band.

Inspection of Equations 2.1 through 2.3 reveals the various parameters that can be adjusted to obtain the signal to noise ratio (I_s/I_n) necessary to meet a particular NEL requirement. For any given application many of the instrument parameters are determined by constraints such as maximum size and weight, required ground coverage, and state-of-the-art component performance. For the purpose of this study, a composite of the EOS point design instruments was taken as a baseline instrument and such parameters as size (telescope aperture collecting area) transmission, scan efficiency, etc, were considered typical of a scanning radiometer for the Thematic Mapper application. Detector and preamplifier parameters were also taken from the EOS point design studies as representative of current state-of-the-art. Table 3 lists the values of all the fixed parameters used to evaluate Equations 2.1 through 2.3 for the tradeoff charts.

After eliminating all the parameters that are fixed for one reason or another, only the orbital altitude, the size of the ground resolution, and the number of detectors per spectral band are left

Table 3

REFERENCE INSTRUMENT PARAMETERS
(Symbols defined in text)

$R = 0.22$ A/W	$0.42<\lambda<0.48$
$= 0.3$ A/W	$0.48<\lambda<0.52$
$A = 10^3$ cm^2	
$\tau_o = 0.23$	$0.42<\lambda<0.48$
$= 0.35$	$0.48<\lambda<0.52$
$\gamma = 0.8$	
$V_A = 2.2 \times 10^{-9}$ volts	
$C_T = 7 \times 10^{-12}$ farad	
$T = 300$ °K	
$R = 10^{10}$ ohm	
$I_D = 3 \times 10^{-15}$ A/Hz$^{1/2}$	
$I_A = 6 \times 10^{-16}$ A/Hz$^{1/2}$	
$W = 182.5$ km	
$V = 6.47$ km/s	900 km orbit
$= 6.745$ km/s	716 km orbit
$\eta = 0.8$	

for parametric variation. Decreasing the orbital altitude increases the solid angle subtended by the radiometer of a scene element thereby increasing the collected power and instrument performance. Increasing the size of the ground resolution increases the power on the detector which also improves performance. Finally, increasing the number of detectors per spectral band allows the radiometer to scan more slowly. This results in a lower electrical bandwidth and less integrated (rms) noise appears at the output of the radiometer. Tradeoff relationships between these three parameters are presented in Figures 1 to 8 for an 0930 orbit (Figures 1 to 4) and a 1200 orbit (Figures 5 to 8). On each graph the bounds on radiometer performance are indicated by dashed horizontal lines. The upper line represents the maximum NEL acceptable (least sensitivity) while the lower dashed line indicates the desired NEL (desired sensitivity). The upper and lower bounds represent approximately 0.5% and 0.2% change in reflectivity respectively. Each graph presents the relationship between performance (NEL) and the number of detectors per spectral band as a function of ground resolution for a particular spectral band and orbital condition. Each graph defines the combination of instrument parameters that will produce acceptable or desirable performance for a particular spectral band and orbital condition. For example, Figure 1 shows that in the 0.48-0.52 micron band with an 0930, 900 km orbit, acceptable performance at 30 meter ground resolution can be obtained by scanning 360 lines in parallel (360 detectors per spectral band). It if is desirable to limit the radiometer to 16 detectors per spectral band, then the ground resolution would have to be increased to about 57 meters to obtain acceptable radiometric performance.

Several interesting features are illustrated by these graphs. The first is the change in the slope of the line which is most pronounced for the 30-meter ground resolution. This change in slope reflects the transition from preamplifier or detector limited performance to noise-in-signal (statistical variation of the signal) limited performance as the number of detectors per spectral band is increased (lower electrical bandwidth) and/or the ground resolution is increased (total power on the detector increased). A second observation is that performance improves rapidly as the ground resolution is increased. Looking at the complete set of eight graphs the following observations can be made:

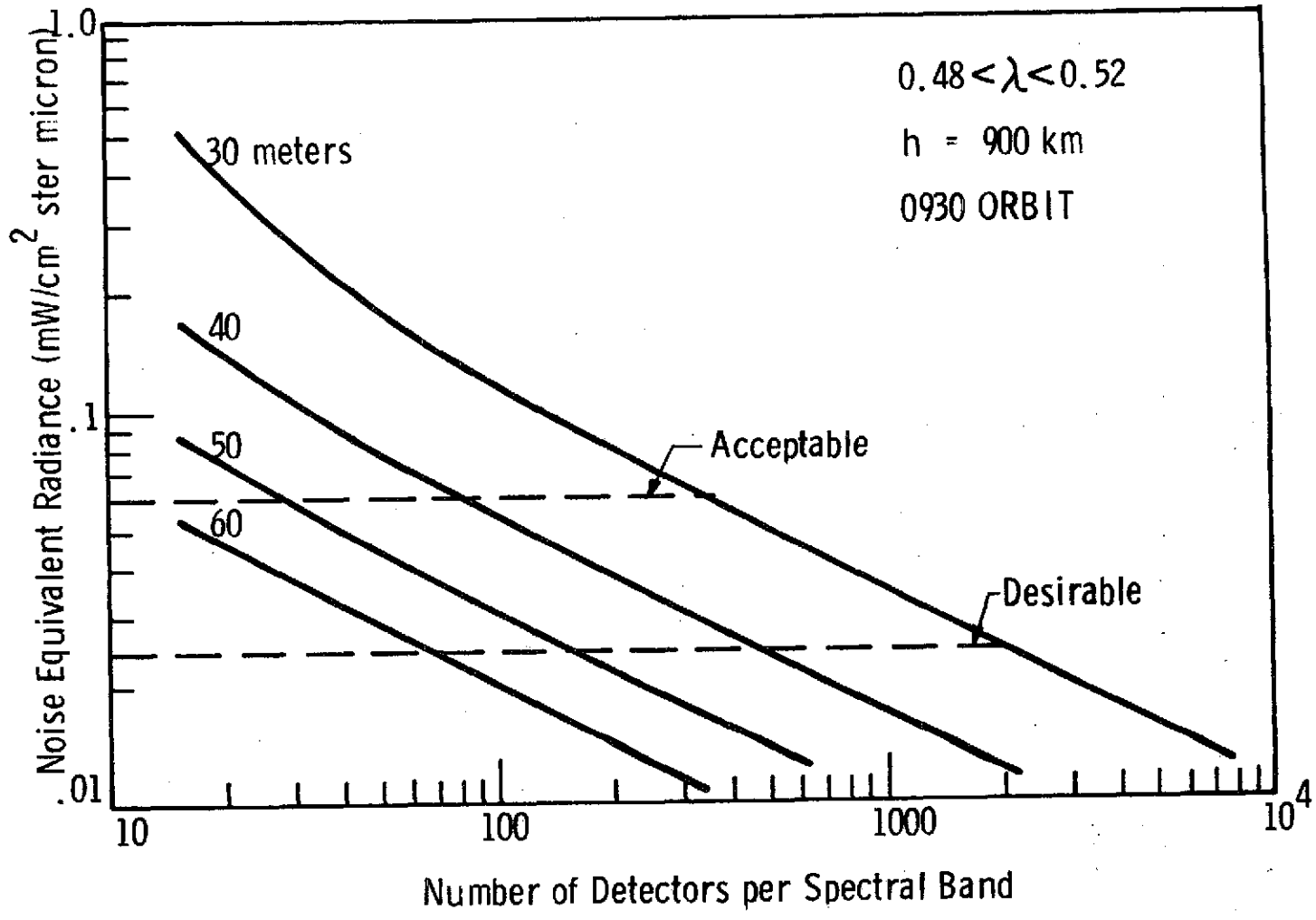

Figure 1 RESOLUTION AND NEL VS NUMBER OF DETECTORS

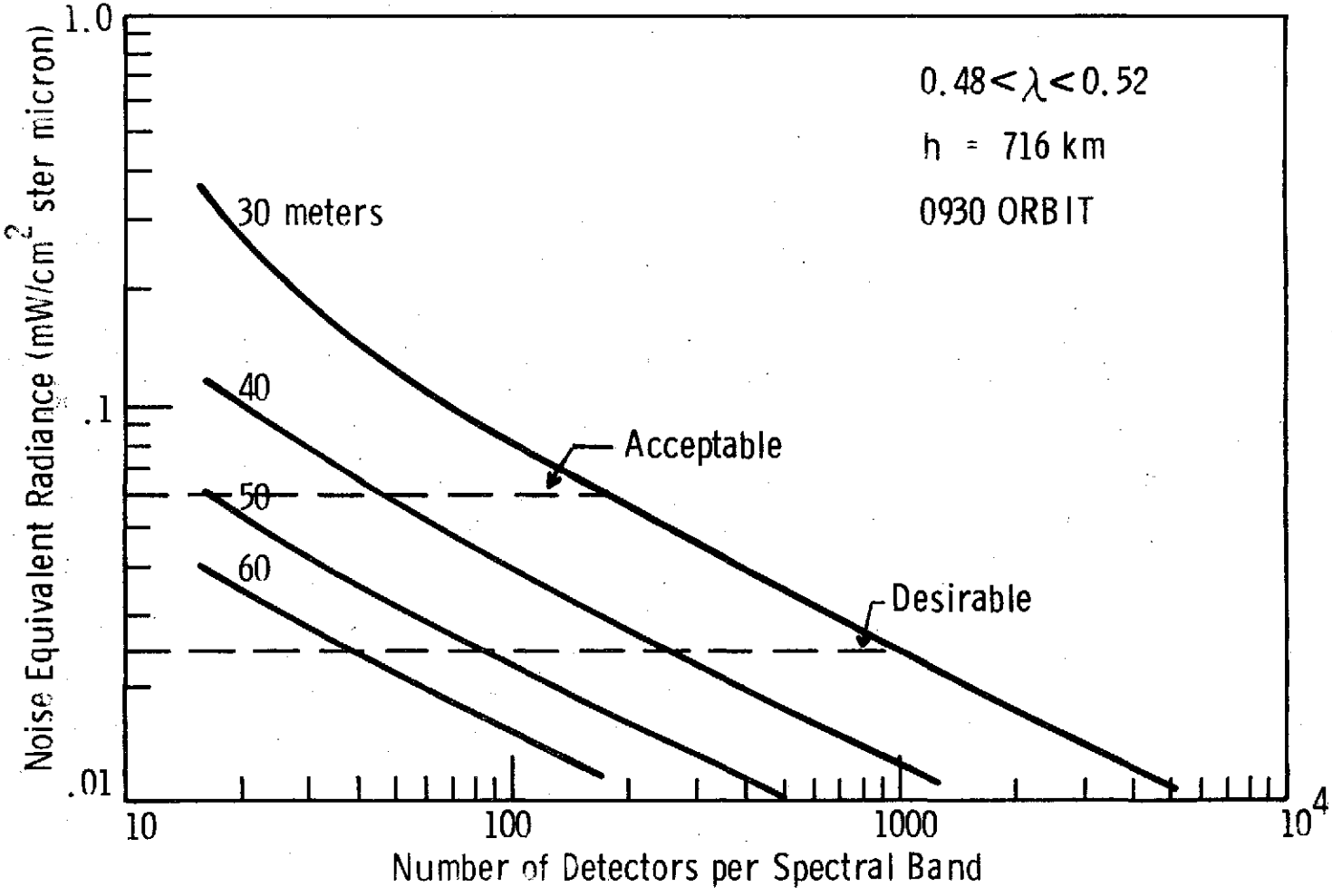

Figure 2 RESOLUTION AND NEL VS NUMBER OF DETECTORS

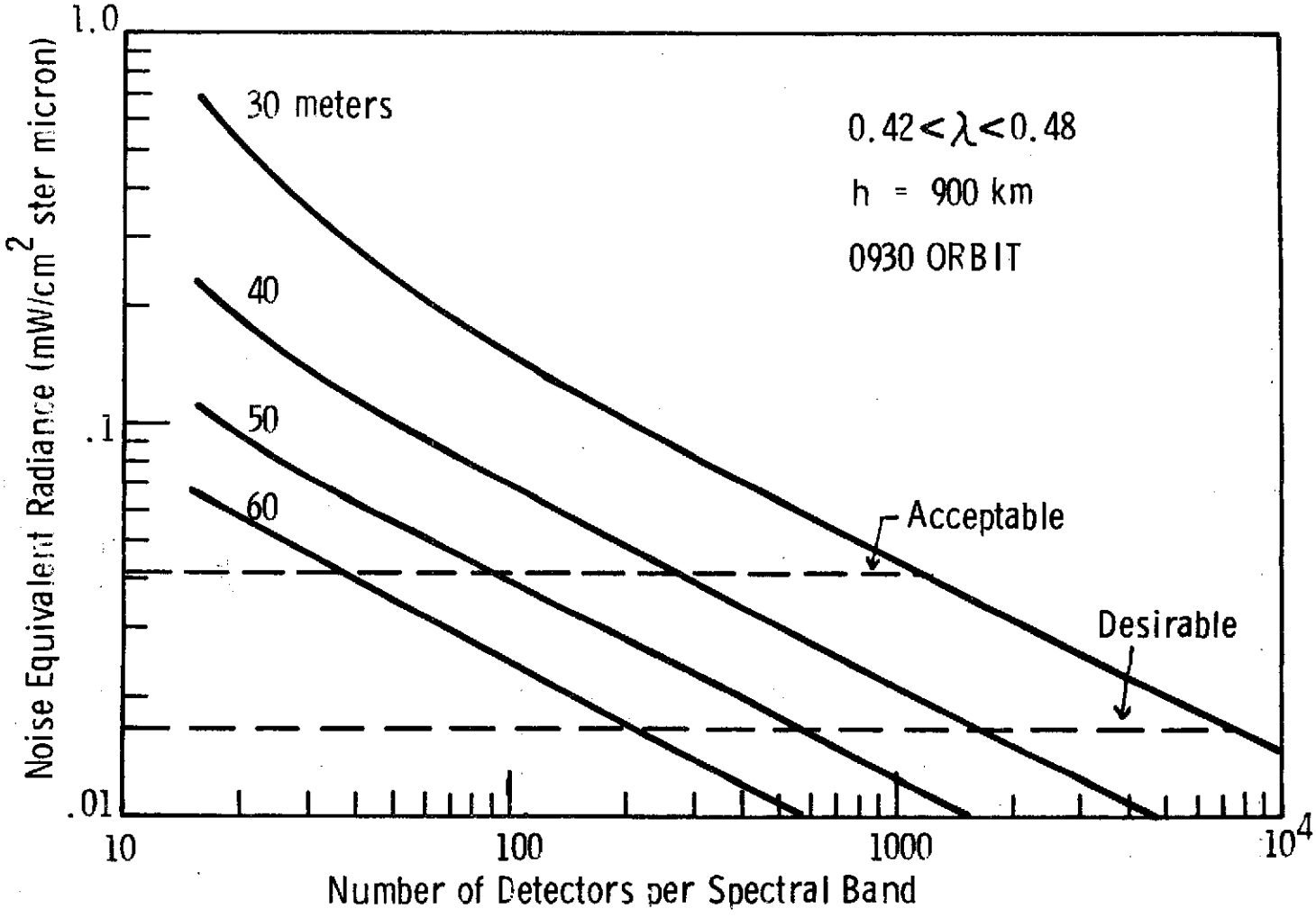

Figure 3 RESOLUTION AND NEL VS NUMBER OF DETECTORS

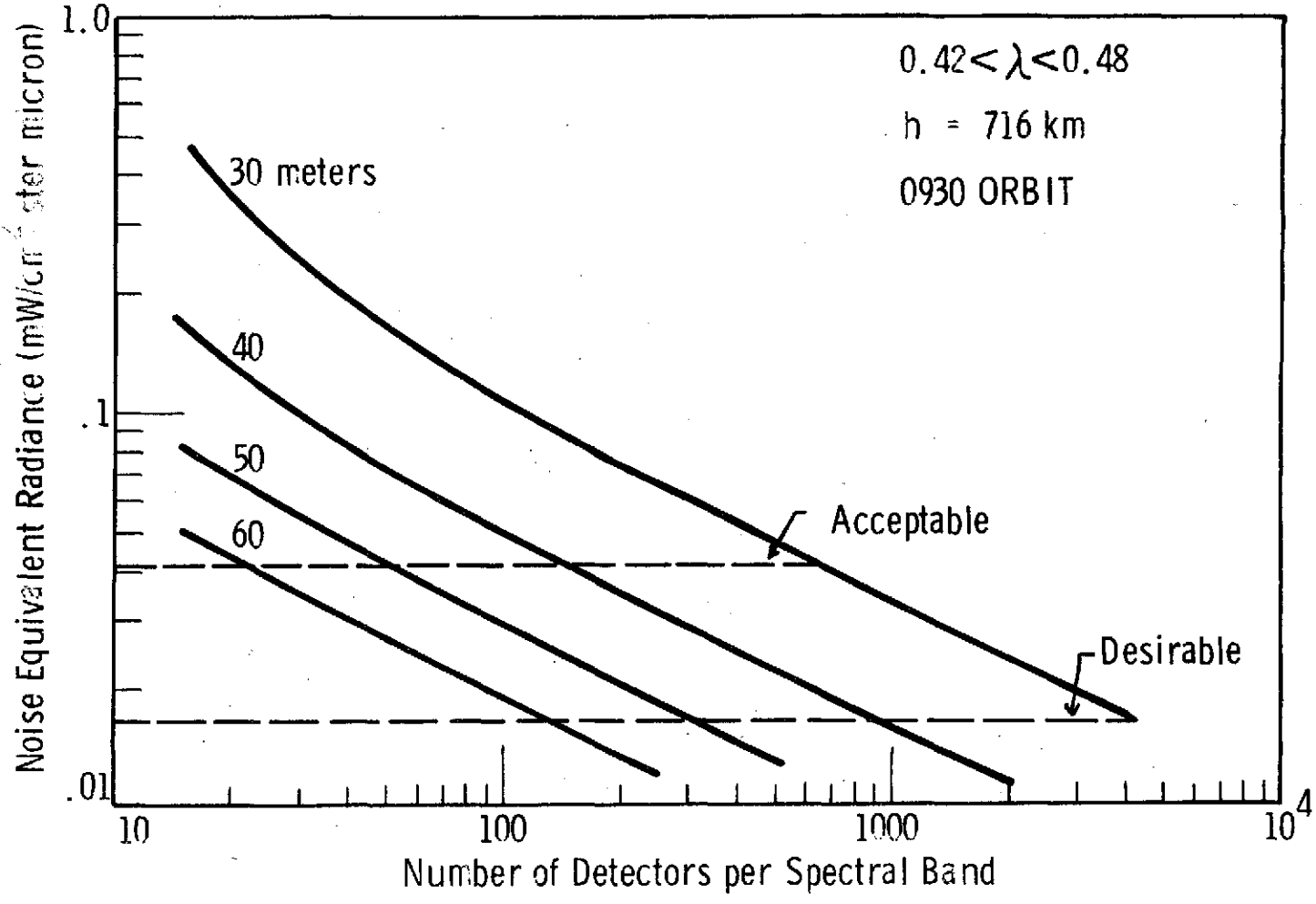

Figure 4 RESOLUTION AND NEL VS NUMBER OF DETECTORS

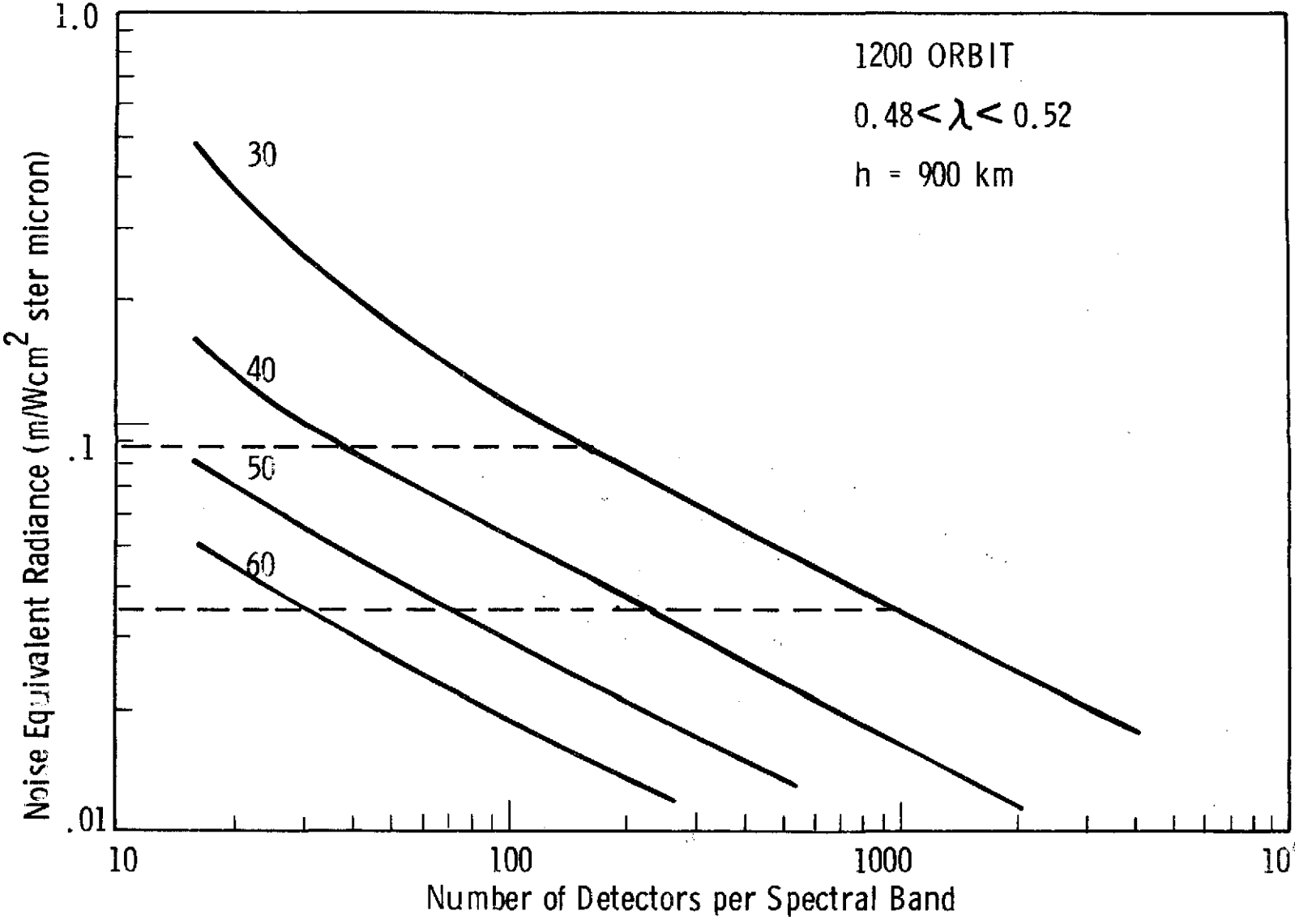

Figure 5 RESOLUTION AND NEL VS NUMBER OF DETECTORS

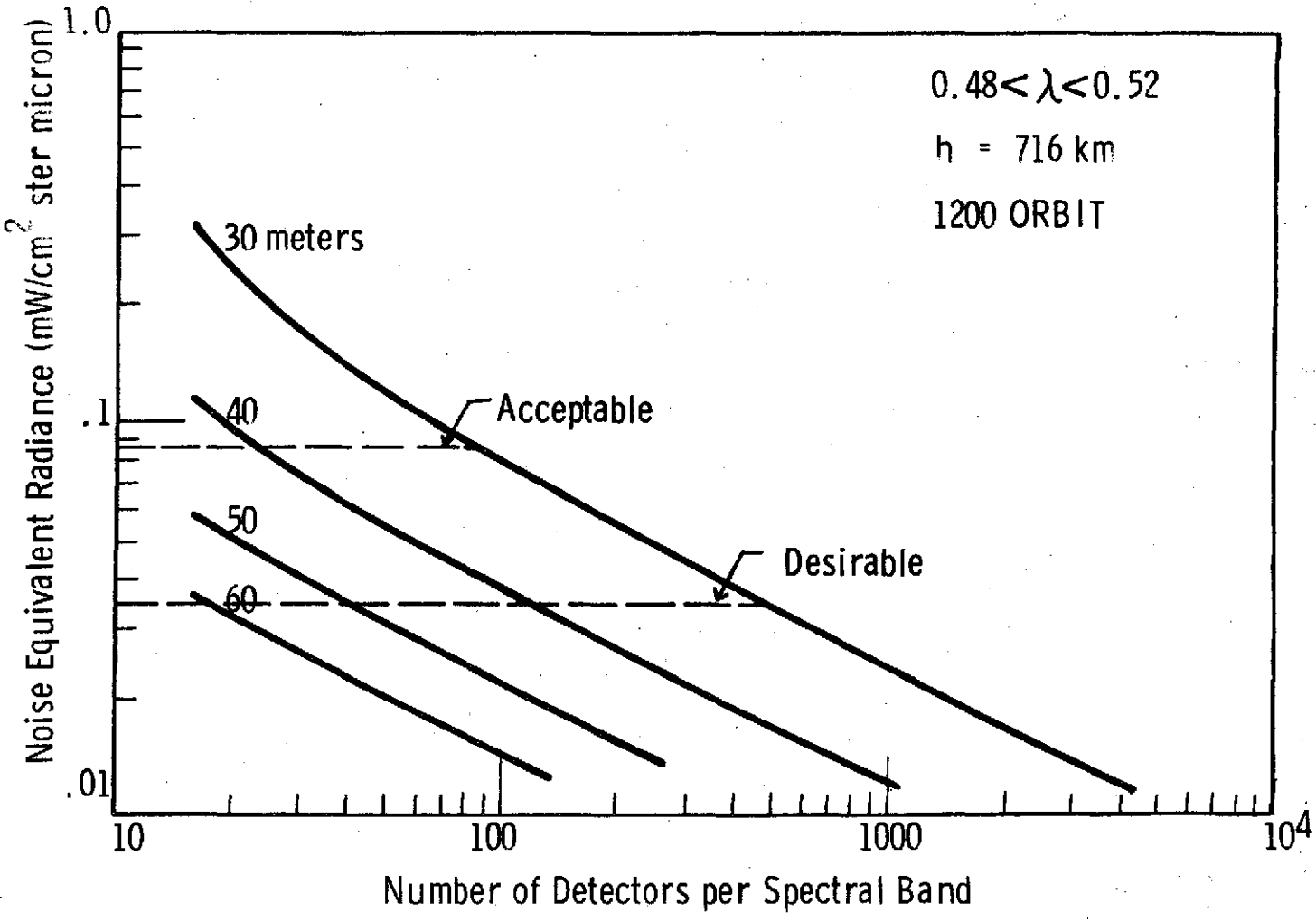

Figure 6 RESOLUTION AND NEL VS NUMBER OF DETECTORS

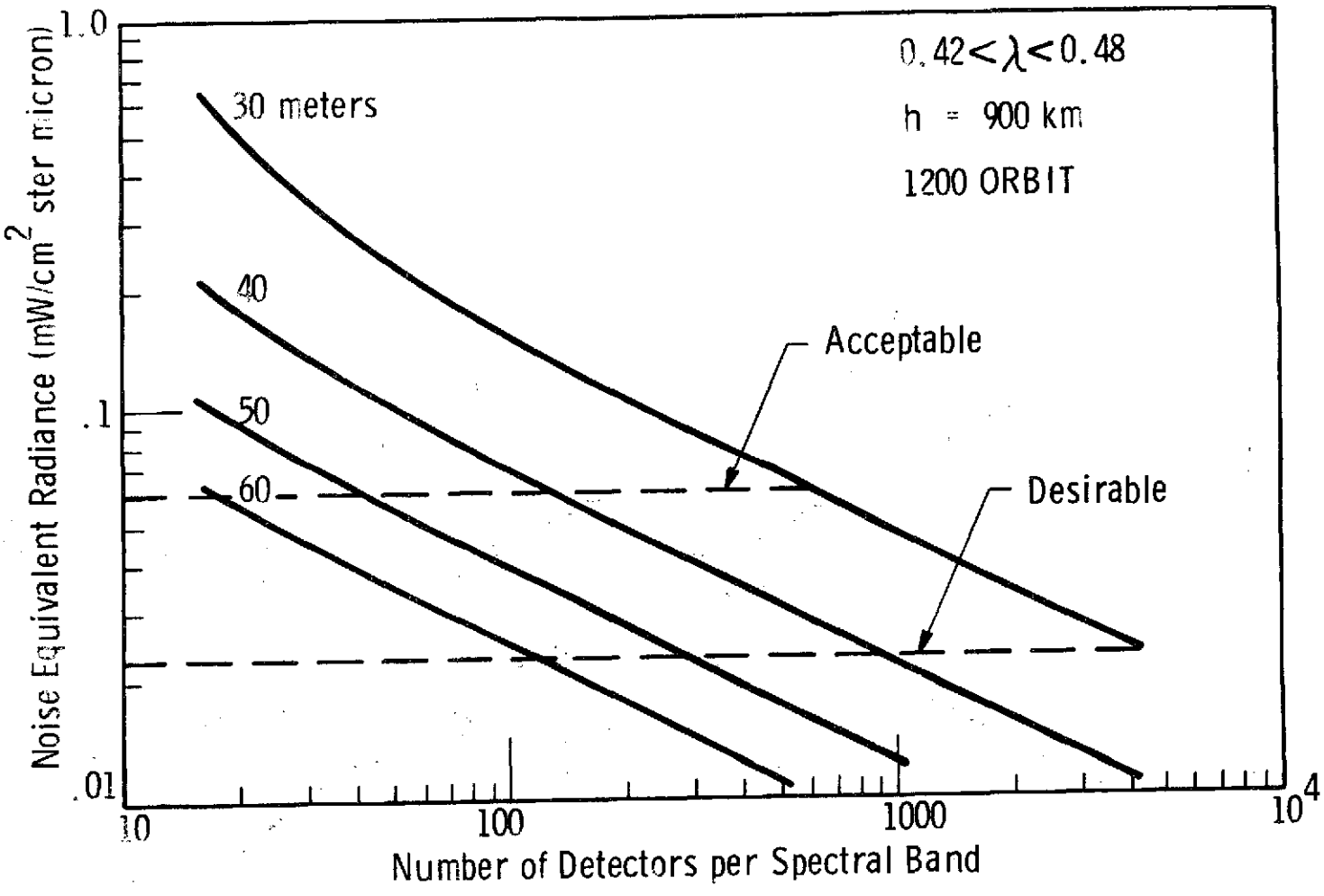

Figure 7 RESOLUTION AND NEL VS NUMBER OF DETECTORS

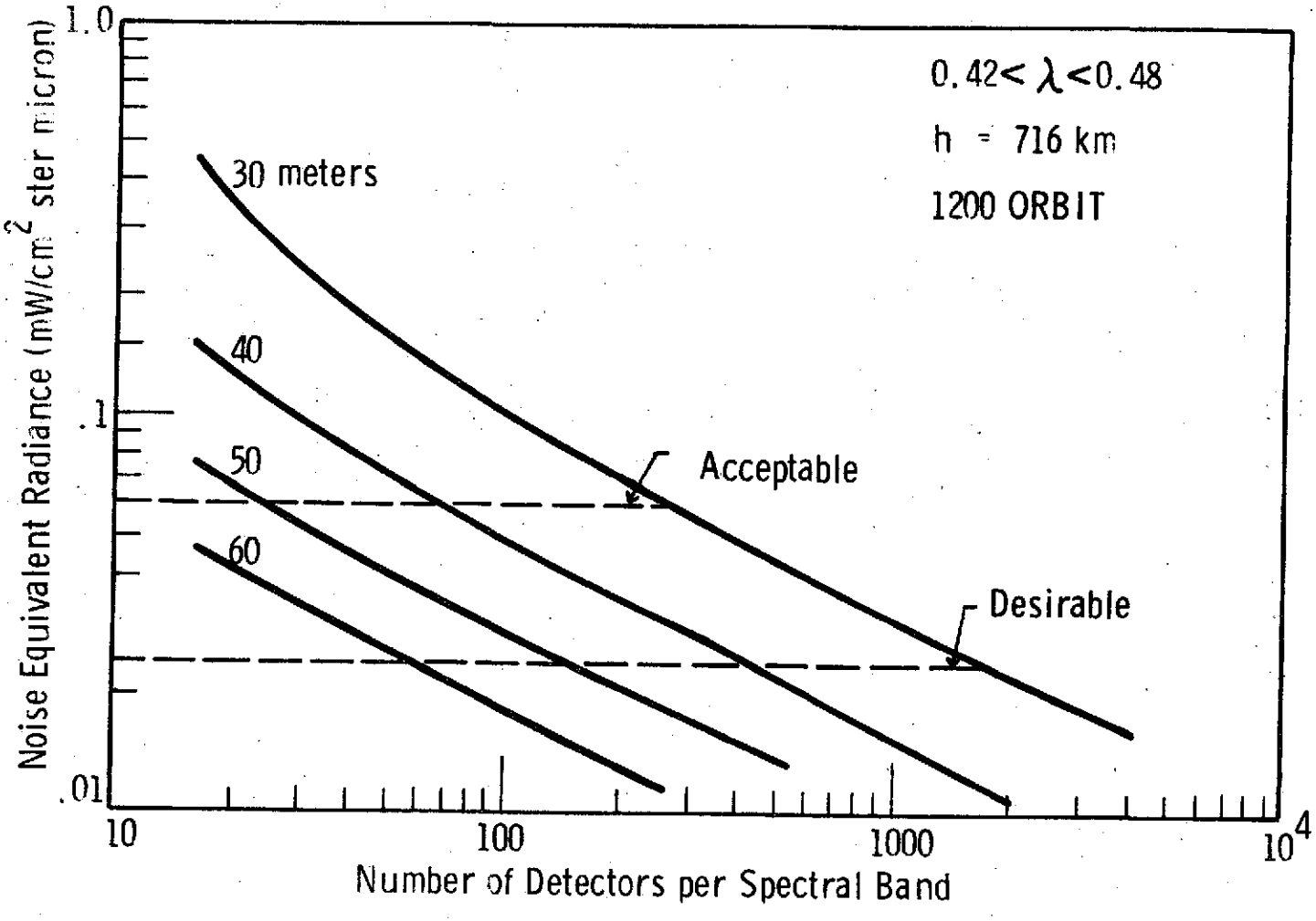

Figure 8 RESOLUTION AND NEL VS NUMBER OF DETECTORS

1) Going to a lower orbit (716 km vs 900 km) results in about a factor of two reduction in the number of detectors per spectral band required to achieve a particular performance level (NEL) for any given ground resolution.

2) Going to a 1200 noon orbit rather than an 0930 orbit results in somewhat more than a factor of 2 reduction in the number of detectors per spectral band required to achieve a particular performance level for any given ground resolution.

3) Inclusion of the 0.42 - 0.48 micron band increases by a factor of more than 3.5 the number of detectors per spectral band required to achieve a particular noise equivalent reflectivity ($NE\Delta\rho$) as compared to an instrument designed only to include the 0.48-0.52 micron band. The economic implications of the above observations are discussed in the next section.

The graphs presented in Figures 1 to 8 can be extrapolated to cover cases not explicitly presented in Figures 1 to 8. Consider first an increase in spectral bandwidth. With reference to Equation 2.1, increasing the spectral bandwidth, $\Delta\lambda$, linearly increases the signal current to a first order approximation. Referring to Equations 2.2 and 2.3, the noise current is proportional to (I_s/n) for n and/or I_s large enough that the $2eI_s$ term dominates. (In terms of the graphical presentations, the dominance of the $2eI_s$ term corresponds to those regions where the slope of the curve is -0.5). The signal-to-noise current is then proportional to (nI_s) or equivalently $(n\Delta\lambda)$. Therefore, scaling n by the inverse of the change in spectral bandpass will yield the new performance relationship. For example, if the spectral bandwidth is doubled, then the abscissa (horizontal axis) is multiplied by 0.5. With reference to Figure 1, this means that a doubling of spectral bandwidth would allow acceptable 40 meter performance with 40 detectors per spectral band rather than 80, all other factors being equal. In all likelihood, all other factors are not equal because the acceptable NEL could decrease with increasing spectral bandwidth depending on the details of the spectral reflectivity of the observed material. This relationship would have to be supplied by ERIM or the user community. It should be stressed that the scaling procedure described is only valid for those portions of the graph with a -0.5 slope. For the other portions of the graph it will be necessary to evaluate Equations 2.1 - 2.3 using the new conditions.

Referring again to Equations 2.1 - 2.3 an increase in the telescope collecting area of the subject radiometer can be handled in the same manner as an increase in spectral bandwidth. Extrapolation of

the tradeoff charts to other spectral bands would be difficult and would yield questionable results. It would be more fruitful to generate a new set of curves.

2.3 COST IMPACT

Obtaining an accurate cost estimate for a particular radiometer configuration is a difficult and time-consuming undertaking. Generally past experience is a better indicator of total procurement cost than an engineering estimate. Accordingly a search was initiated to find an existing econometric model applicable to the thematic mapper. This search uncovered an econometric model developed by NASA based on a sample of 6 scanning radiometers. Curve fitting by NASA to the price vs performance points yielded a relationship of the form

$$\text{Cost} = K \frac{(\text{Number of information channels})^{.57}}{(\text{IFOV})^{.13}} \qquad (2.4)$$

Work done under the EOS Point Design studies indicated an order of magnitude cost of 20 million dollars for a 7-band 16-detector/band scanning radiometer. Using this cost estimate as a baseline and Equation 2.4 for extrapolation, a cost vs complexity graph can be generated as shown in Figure 9. Curves are drawn for a 7-band and an 11-band radiometer. Both 30 meter and 60 meter resolution are shown.

The most obvious feature of Figure 9 is that radiometer cost increases rapidly as the number of detectors per spectral band increases. Although the graph extends to over 200 detectors per spectral band, it is doubtful that the relationship expressed by Equation 2.4 is valid beyond 64 detectors per spectral band because for large arrays of detectors a different technology would be used.

2.4 INSTRUMENT IMPACT

Several other implications of the ERIM worst case performance requirements should be considered. The first is the impact of the required NEL and number of spectral bands on the data rate of a thematic mapper. The EOS point design specification indicated a seven bit word. Figure 10 presents the bit rate vs the number of spectral channels for 30, 40, and 50 meter ground resolution. The multiplexer proposed for the thematic mapper has a bit rate limit of 120×10^6 bit per second as indicated by the dashed upper bound on bit rate. The

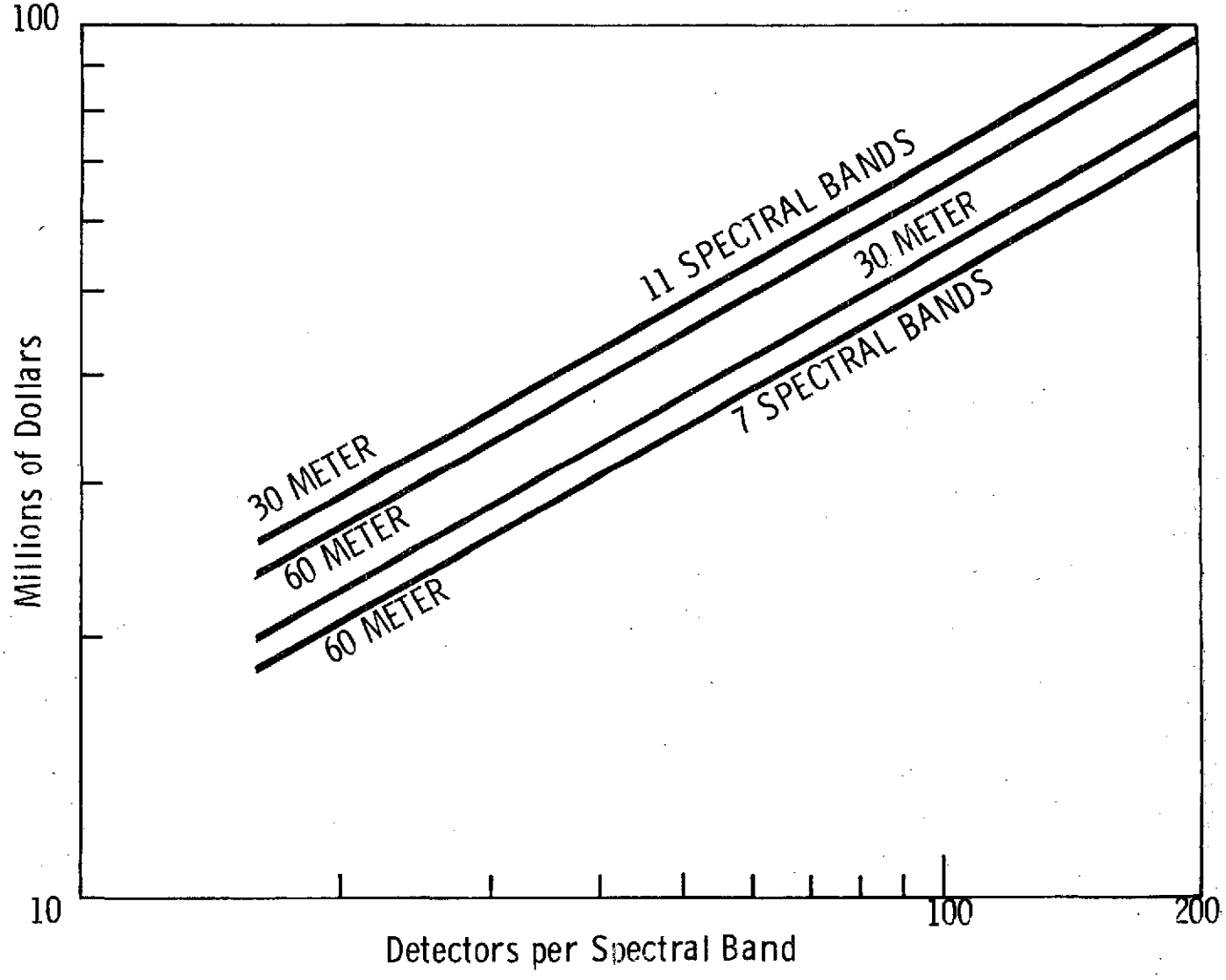

Figure 9 COST VS RESOLUTION AND NUMBER OF DETECTORS

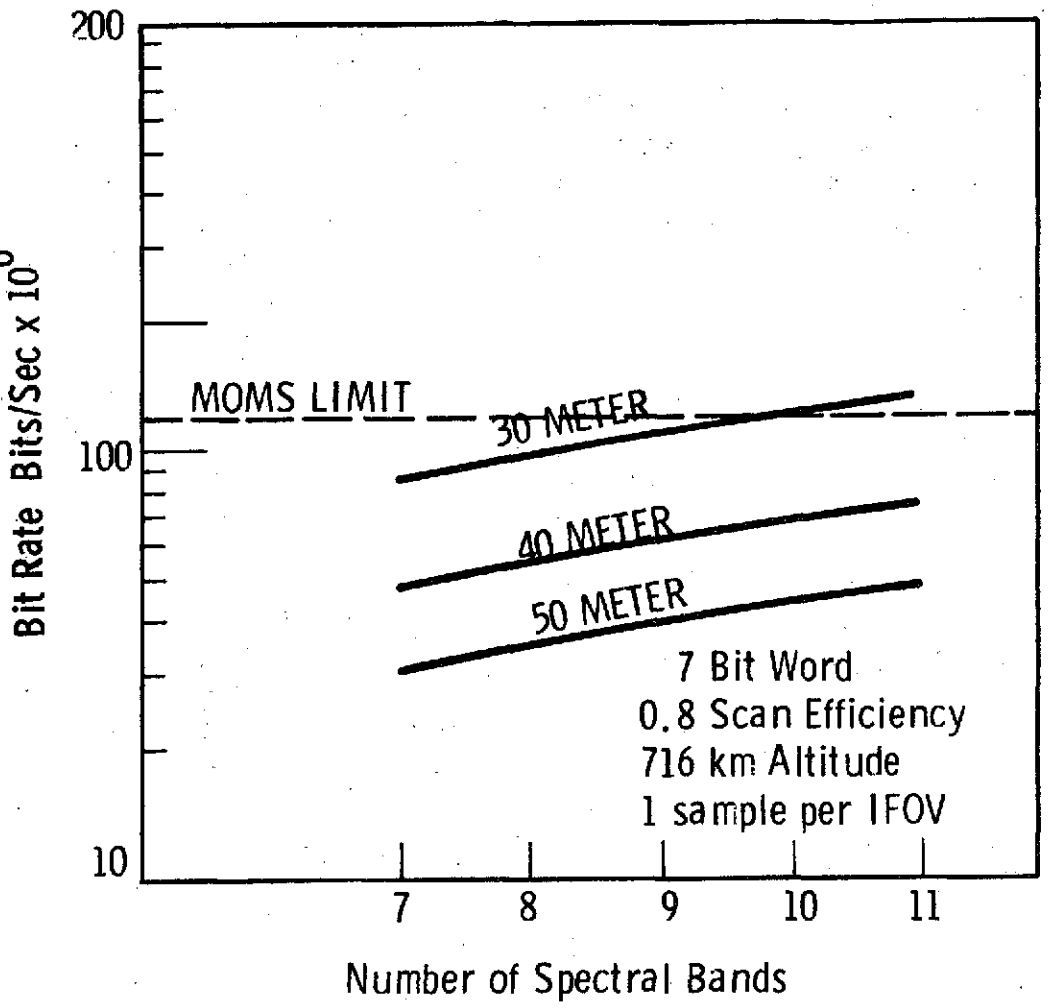

Figure 10 BIT RATE VS RESOLUTION AND NUMBER OF SPECTRAL BANDS

ratio of the desired NEL to the maximum radiance expected yields a dynamic range for the ERIM data of about 1000. This would require a 10 bit word for linear encoding. Figure 11 presents the bit rate vs number of spectral channels assuming a 10 bit word length and various ground resolutions. It can be seen that going to 40 meter resolution results in a manageable data rate even with 11 spectral bands.

Another consideration bearing on the trade-off graphs of Section 2.2 is the relationship between the number of lines scanned in parallel (number of detectors per spectral band) and the 'bow tie' effect for linear scanners. The Te Point Design Study indicates that for the 716 km altitude, 30 meter resolution, 185 km swath width, 16 detectors per spectral band results in 9.1% misregistration at the edge of the field while 32 detectors increases the misregistration at the edge of the field to 18%. Accordingly there may be a large penalty in terms of data reduction time for increasing the number of detectors per spectral band on a linear scanner. A conical scanner has a constant line-of-sight distance to the scene and, therefore, does not suffer a bow tie effect.

Another result of the ERIM study, not mentioned in Section 2.1, is the desirability of having the same IFOV in the thermal channel as in the other spectral channels. The obvious difficulty associated with providing this capability in a thematic mapper is that optical diffraction effects are a factor of 10 worse than for the 1 micron portion of the spectrum. In addition, decreasing the ratio of the thermal IFOV to visible IFOV from 4:1 to 1:1 decreases the available energy by a factor of 16. To determine the feasibility of obtaining adequate performance in the thermal band under these conditions, calculations were done for a radiometer with 40 meter ground resolution scanning 64 lines in parallel. Under these conditions, the 40-meter resolution thermal channel will provide a low spatial frequency noise equivalent temperature difference (NEΔT) of 0.6 °K at 340 °K assuming a D^*_λ of 3×10^{10} cm $Hz^{1/2}$ W^{-1}. The MTF of the thermal channel at the 1/2 IFOV frequency is about 0.34 for a 16 inch telescope entrance pupil assuming the detector is matched to the IFOV and the electronic rolloff is matched to the 1/2 IFOV frequency. The MTF could be increased but at a loss in performance.

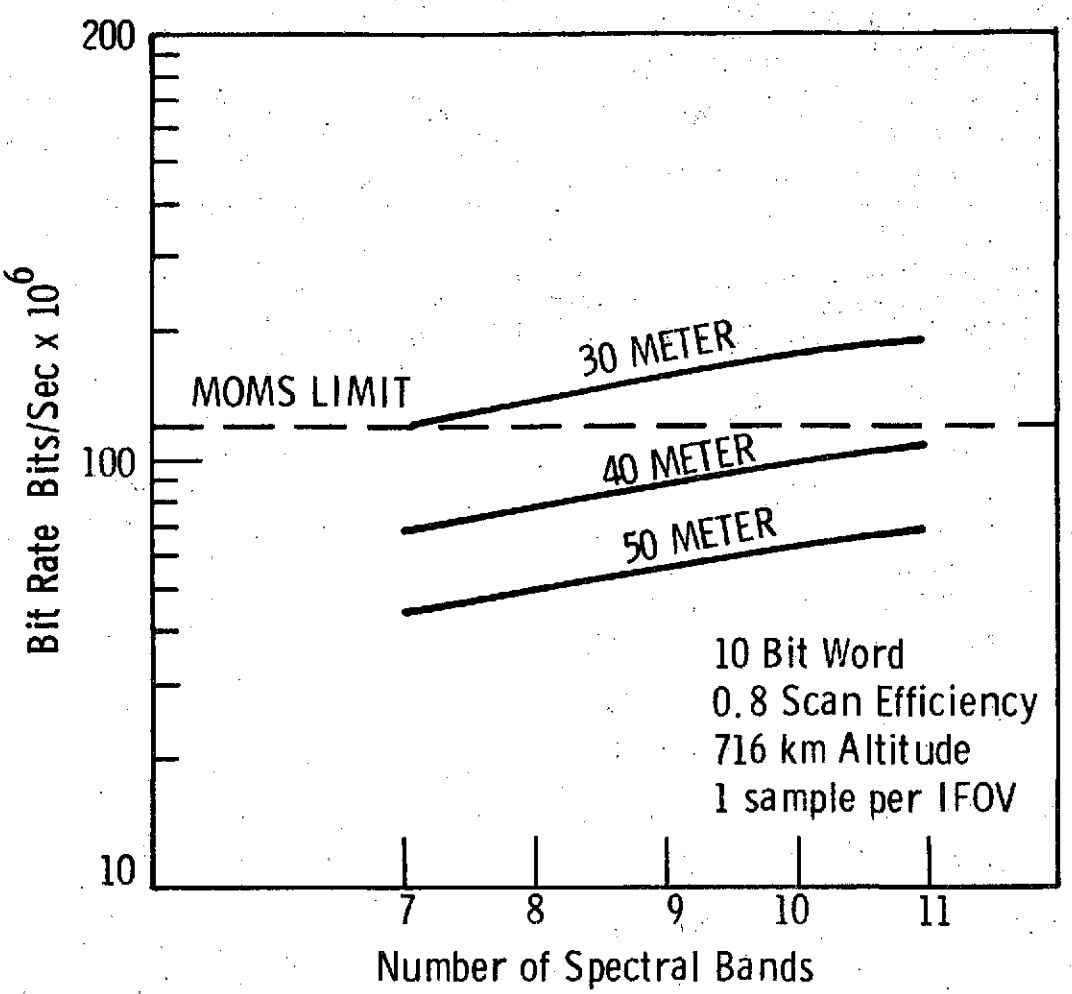

Figure 11 BIT RATE VS RESOLUTION AND NUMBER OF SPECTRAL BANDS

SECTION 3

CONCLUSIONS AND RECOMMENDATIONS

3.1 INSTRUMENT DESIGN

The three designs for the thematic mapper as presented in the three EOS Point Design Study Reports differ considerably from each other. Each instrument has some outstanding features and some weak points. The Hughes design allows the largest telescope aperture for the given package size constraint. This would imply the best potential radiometric performance as well as the highest MTF for a high resolution thermal channel. The Honeywell design minimizes the mechanical complexity and has the fewest number of moving elements. The conical scan concept results in a constant ground resolution throughout the scan. The Te design produces a linear unidirectional ground scan. As far as can be determined from the material presented in the design reports each of the scanners is capable of meeting the original EOS Point Design Study Specification with the possible exception of the Te design radiometric performance owing to the fact that the Te design has less than one-half the optical collecting area of the Hughes design.

Based on preliminary analysis, each of the three designs can be modified to accommodate changes in user requirements such as a greater number of spectral bands or an increase in sensitivity. For this reason, it is not possible at this level of analysis to recommend one design concept above the other two concepts.

3.2 RADIOMETRIC PERFORMANCE

The obvious conclusion that can be drawn from Figures 1 to 9 is that a thematic mapper designed to meet the ERIM worst case sensitivity requirements while providing 30-meter ground resolution would be considerable more expensive than now envisioned. A more subtle conclusion that can be drawn from Figures 1 to 9 is that the current EOS point design instruments are operating at a less than optimum point of the radiometric performance tradeoff plane. Either an increase in the ground resolution or an increase in the number of detectors per spectral band would move the system from a detector/preamplifier noise-limited performance condition to the condition where radiometric performance is limited only by the statistical variation of the input radiance.

One of the results of the EOS Data Integration Study Final Review (JSC, June 10 - 11, 1974) was that high (30 meter) ground resolution did not seem to be important in meeting a broad class of user requirements. With this thought in mind, it seems reasonable to recommend that the ground resolution of the thematic mapper be increased from 30 meters to 40 or 50 meters. This would result in the following:

a. A 3x (40 meter) to 6x (50 meter) increase in sensitivity (decrease in NEL) for the 16 detector per spectral band case.

b. Feasibility for setting the thermal channel (10.4 -12.6 μm) IFOV equal to the visible IFOV.

c. Data rates compatible with 10 bit word length and 11 spectral bands.

d. Lower instrument cost.

3.3 FURTHER STUDY

During the course of this study it became obvious that a general consensus on user requirements would not be reached quickly. Accordingly this HRC report has been configured to help in determining which user requirements impose a heavy burden on the instrument design. Using the tradeoff graphs contained in this report, the general parameters of a thematic mapper can be established. However, as discussed in the Hughes EOS Point Design Study (their Section 2.2.3) optimization of MTF vs radiometric performance should be conducted once the generalized parameters are established. This optimization is most effective when the performance modeling relates the instrument parameters (S/N, Ground Resolution) to the user requirements (classification accuracy). It is highly recommended that such an optimization of instrument parameters be conducted once a user consensus is established.

Appendix D shows that the concept of a pushbroom radiometer is a viable alternative to a scanning radiometer, especially where extreme radiometric sensitivity is required. It is recommended that the pushbroom concept for a radiometer be further studied to resolve such problem areas as wide field optical design, in-flight radiometric calibration, dc restoration, and the configuration of the image plane. The rate of progress on linear detector array technology, especially the application of CCD concepts to both the visible and near and far infrared regions of the spectrum

indicates that the state-of-the-art in the 1978 time frame will be such as to make a pushbroom radiometer a practical solution for the thematic mapper application.

APPENDIX A

FINAL REPORT

COMPARISON OF RADIATIVE COOLER DESIGNS PROPOSED FOR SCANNING SPECTRAL RADIOMETER

Prepared for

Honeywell, Inc., Radiation Center
Two Forbes Road
Lexington, Massachusetts 02173

Honeywell Project No. 22548-01

Prepared by

Arthur D. Little, Inc.
Cambridge, Massachusetts 02140

14 May 1974

C-74977-11

PURPOSE AND SCOPE

The objective of this study was to perform a preliminary evaluation of the feasibility and practicality of radiative cooler design approaches proposed for a Scanning Spectral Radiometer. The evaluation was made by examining three reports of point design studies submitted to the NASA Goddard Space Flight Center by Honeywell, Inc., Radiation Center, the Hughes Aircraft Corp., and Te Co. (Division of Gulton Industries). The reports were furnished to us by Honeywell. In accordance with the funding and time available for this study, the evaluation was primarily qualitative in nature and dealt with the feasibility and general practicality of the proposed design approaches and techniques for integration with the associated radiometer.

SUMMARY

A radiative cooler suitable for use aboard satellites must integrate design solutions to mechanical, thermal and optical alignment requirements. All of these factors must be dealt with effectively or the final cooler design will not meet performance expectations. The accompanying chart summarizes our comparison of the three radiative coolers proposed by Honeywell, Inc., Radiation Center, Hughes Aircraft Corp., and Te Co. (Division of Gulton Industries), respectively.

It should be emphasized that the comparison was made on the basis of a relatively short-term study, approximately two weeks, of the final point-design study reports submitted by these companies and reflects our evaluation of the work reported. Also, our effort was funded by Honeywell and there was no written or oral communciation between ADL and either Hughes or Te Co.

Both Honeywell and Te Co. based their radiative cooler integration plans on using a flight-proven Arthur D. Little, Inc. (ADL) radiative cooler, while Hughes based their design on an in-house radiative cooler. Certainly one important aspect of the cooler evaluation is flight precedent and we are aware of the fact that three ADL coolers have been flown successfully

RADIATIVE COOLER DESIGN COMPARISON

	HONEYWELL RADIATION CENTER PROPOSAL	HUGHES AIRCRAFT CORP. PROPOSAL	TE CO. (DIVISION OF GULTON IND.) PROPOSAL
APPLICATION REQUIREMENTS			
• Operating temperatures	200 K - 2nd stage 105 K - 1st stage	85-90 K - 1st stage	105 K - 1st stage
RADIATIVE COOLER DEFINITIONS			
• Cooler manufacturer	Arthur D. Little, Inc.	Hughes Aircraft Corp.	Arthur D. Little, Inc.
• Cooler design configuration	101° CFOV conical body of revolution	truncated conical body of revolution	101° CFOV conical body of revolution
RADIATIVE COOLER SUITABILITY			
• Ability to survive launch environment	documented capability to survive 35 g's RMS mechanical environment	unknown	documented capability to survive 35 g's RMS mechanical environment
• Previous flight experience	one of 3 current flight units has operated over 16,000 hrs. below 110 K	unknown	one of 3 current flight units has operated over 16,000 hrs. below 110 K
• Optical alignment capability	optical alignment of inner stage and outer stage at operating temperature documented	unknown, but suspected to be relatively poor	optical alignment of inner stage and outer stage at operating temperature documented
• Self-contamination resistance	only vacuum system compatible materials are used for construction	Lexan inner stage support element could be a source of contamination	only vacuum system compatible materials are used for construction
• Contamination protection capability	decontamination heaters used on inner and outer stages	decontamination heaters could be mounted on cooler stages	decontamination heaters used on inner and outer stages
• Suitability for bench testing	bench testing can be accommodated by using outer stage as part of vacuum enclosure	design presented must be modified to accommodate evacuation	bench testing can be accommodated by using outer stage as part of vacuum enclosure
• Developmental risk	low	unknown, but estimated to be relatively high	low

in orbits similar to the one proposed for the Scanning Spectral Radiometer, even though this information was not mentioned in the Honeywell or Te Co. reports. Since the Hughes cooler was of their own design and there was no flight data cited in their report, we concluded that it was not a flight-proven unit. On this basis, we were concerned about the validity of comparing the Hughes design concept with the ADL flight unit. However, in an effort to arrive at a relative comparison with regard to cooler performance and capability, we have compared these units on the basis of general design approach and overall suitability for operation in the sun-synchronous orbit.

TECHNICAL DISCUSSION

The evaluation criteria primarily considered in this study were as follows:

- suitability to survive the mechanical environment associated with launch
- capability to achieve desired operating temperatures and refrigeration capacities in orbit
- ability to maintain optical alignment with the associated radiometer

Radiative Cooler Proposed by Honeywell, Inc., Radiation Center

The Honeywell study approach utilized an ADL radiative cooler, but there was no detailed treatment of how it would be integrated with the radiometer or the degree of optical alignment required between the cooler mounted components and the radiometer. Therefore, it was difficult to assess the adequacy of the way in which the cooler was to be applied in their instrument; however, based on existing flight data we know that the cooler proposed for use here is capable of perfoming satisfactorily in this application.

Radiative Cooler Proposed by the Hughes Aircraft Co.

It appeared that Hughes based much of their cooler design on some similar principles established for the Multi-Spectral Scanner (MSS) which is a Nimbus sun-synchronous orbit. However, the MSS cooler, developed by

Hughes has a rectangular outer stage compared to the truncated-cone outer stage presented for the design in the point-design study report. There was also mention in the report of design principles taken from a cooler for the Visible IR Spin Scan Radiometer (VISSR). We understand that this was a larger cooler design and built by the Santa Barbara Research Center to operate in a geo-synchronous orbit rather than a sun-synchronous orbit. This cooler does have an outer stage of a truncated-cone configuration. To our knowledge, neither cooler has yet been proven in flight although they have undergone some mechanical and thermal verification on testing on the ground. The above information on the MSS and VISSR coolers was verified in discussions with personnel at the NASA Goddard Space Flight Center. Our observations relative to the design approach advocated are:

- The method of mounting the second stage radiator to the first stage using a thin wall (approximately 0.006 in. thick) polycarbonate (LEXAN) cone is very risky from a mechanical survivability point of view. This problem is aggravated by the fact that the second stage radiator is eccentrically positioned on this support structure such that moment loading will occur during dynamic environment.

- The radiation shields between the first and second stage radiators are only supported at the junction with the polycarbonate cone. These thin wall radiation shield structures will have resonant modes of vibration within the range of normal launch vehicle vibration spectra. At resonance these thin structures are likely to impact one another and possibly fracture or shatter.

- The technique for cooling and purging the cooler for bench testing is not well defined. If the proposed technique involves evacuating the interior of the first stage, the possibility of damaging the second stage polycarbonate support in the process seems to be great.

- It seems very unlikely that the detector lateral positioning capability of the cooler relative to the mounting interface (and the optical axis of the instrument) will be satisfactory. The structural path for the detector consists of a polycarbonate tube connection to the first radiator stage and truss support of the first stage from the cooler mounting ring. The aft relay lens is mounted in a conical support from the cooler mounting ring. It seems very likely that lateral misalignment of the relay lens and the detector will occur as a result of shifting of parts during dynamic environment or due to temperature difference of gradients within the structural paths. For example, the first radiator stage is positioned by a truss structure utilizing unequal tube lengths. At operating temperature the first stage of the radiator will tilt due to unequal contraction of the truss which will cause a lateral and axial shift in the detector position relative to the cooler mounting ring. If the first stage temperature fluctuates, the tilt of the first stage will fluctuate also. Any relative lateral displacement of the detector relative to the aft relay lens will cause angular optical axis shift which is highly magnified. Since these elements appear to be about 1 inch apart, a lateral shift of 0.001 in. will cause a 1 milliradian change in the cooler optical axis. Alternatively, if the optical axis is fixed by the instrument and the relay lens, a 0.001 in. lateral shift of the detector will cause the beam focus and the detector chip to be misaligned by this amount.

- It appears highly unlikely that the degree of alignment and alignment stability required between the detector and relay lens can be maintained between room temperature alignment of the components and operation at desired temperature levels. Lateral shifting of these components in the order of 0.002-0.005 in. seems quite likely in view of the very long and involved structural paths involved. This degree of possible misalignment seems incompatible with the physical dimension of the detector arrays and the layout contemplated.

- The construction technique of using berylium or titanium structural parts and electro-formed radiation shields appears to be excessively expensive, particularly in view of the mechanical survivability risks involved.
- The design concept of integrating multi-layer insulation with the support truss will be very difficult to accomplish with acceptable overall thermal effectiveness. Each shield must be positioned within the available volume without touching adjacent shields and without having significant gaps around the truss tubes which penetrate them.

Radiative Cooler Design Proposed by Te Co.

The Te Co. study approach utilized an ADL radiative cooler, but here again there was relatively little information dealing with how it would be integrated with the radiometer. In general, they appeared to be integrating the ADL cooler correctly with the radiometer and were taking special precautions to achieve optical alignment between all detector channels.

The ADL radiative cooler referred to in this study is a slightly modified version of our flight unit which has the following characteristics:

- Proven capability to survive severe mechanical environment input of 35 g's RMS (20-2000 HZ).
- Proven capability to maintain detector temperatures below 110°K for over 16,000 hrs. of continuous operation.
- Measured capability to maintain alignment of both stages relative to each other within 0.001 in. radially and 0.0005 in. axially from room temperature through launch vibration and cool down to operating temepratures.

GENERAL DISCUSSION

The following comments refer to the application of radiative coolers to satellite instrument applications.

Registration of the Detector and Instrument

All the Scanning Spectral Radiometer design approaches examined utilized multi-element detectors requiring optical registration to a very high degree (less than 0.1 times the detector chip dimension). It has been our experience that the maintenance of accurate positioning at operating temperatures of optical elements incorporated within radiative coolers is very difficult even when the interconnecting structural paths are short and rigid and allowable excursions of motion within the support systems are controlled. The degree of alignment required for the subject radiometer will necessitate special design provisions within the cooler.

Radiative Cooler Covers on Earthshields

The Hughes cooler makes use of a combined earth shield and protective door while the ADL cooler is generally used without an earth shield. However, ADL coolers are generally supplied with a protective door for protection during launch.

Effect of Satellite Orbit Changes on Radiative Cooler

The orbit mentioned in the report was near polar, sun-synchronous, circular, 99° inclination, 900 km altitude, and descending north to south at 9:30 A.M. local time nominal. A few comments will be made here to reflect potential impacts to coolers of changes in orbit parameters and refrigeration loads.

- Increases in orbit altitude will reduce cooler temperatures.
- Shifts of orbit plane from 9:30 towards noon will increase temperatures of both outer stage and inner stage.
- Increases in required refrigeration capacity can be met by increasing cooler overall size. In the case of the ADL cooler, this would mean a departure from the standard unit, but a routine scale up of all components.

APPENDIX B

DETECTOR - CCD TECHNOLOGY

Let us consider an Earth Resources Infrared system designed to scan the three spectral regions 0.5 - 1.1, 1.5 - 2.5, and 10.0 - 12.0 μm. Linear 64-element photovoltaic silicon and indium-antimonide detectors have been proposed to observe the first and second spectral bands, respectively, while a linear 64-element photoconductive mercury-cadmium-telluride array would be used for the third. The conventional approach which requires a preamplifier connected to each detector becomes undesirable for a system of this complexity since, in addition to the weight, volume and power requirements of the preamplifier, the numerous cold feedthroughs represent a significant heat leak source and the large number of individual leads add to the bulk and weight of the system. We shall see that the application of a charge coupled device, similar in structure to the present HRC device, circumvents many of the above problems.

B.1 CCD MULTIPLEX OPERATION

A charge coupled device (CCD) stores, transfers, and serially reads out charge packets introduced into the shift register entrance or through parallel inputs spaced along the register. Figure B-1 illustrates that the functional layout of the HRC CCD makes possible a parallel to series multiplex operation because information is read into the device through the nine parallel input diodes and is then serially read out. A time delay between readout and readin exists which is the product of the transfer time per element and the number of elements. The basic construction of Figure B-1, if extended from nine to 64 elements, would permit a system modification in which one CCD per spectral band would parallel-to-series multiplex the detector signals of that band. This modification would reduce the number of preamps per band to one and the number of feedthrough leads to less than ten with accompanying power, volume and weight reduction. A discussion of that device is included in this appendix to aid in understanding how it and similar CCD's function.

B.2 CCD ANALYSIS

For the purposes of this study, consider a system in which a separate CCD is utilized per spectral band and which serves as a parallel-to-series multiplexer. The detector signals will be coupled to a surface channel two-phase 64-element CCD through parallel

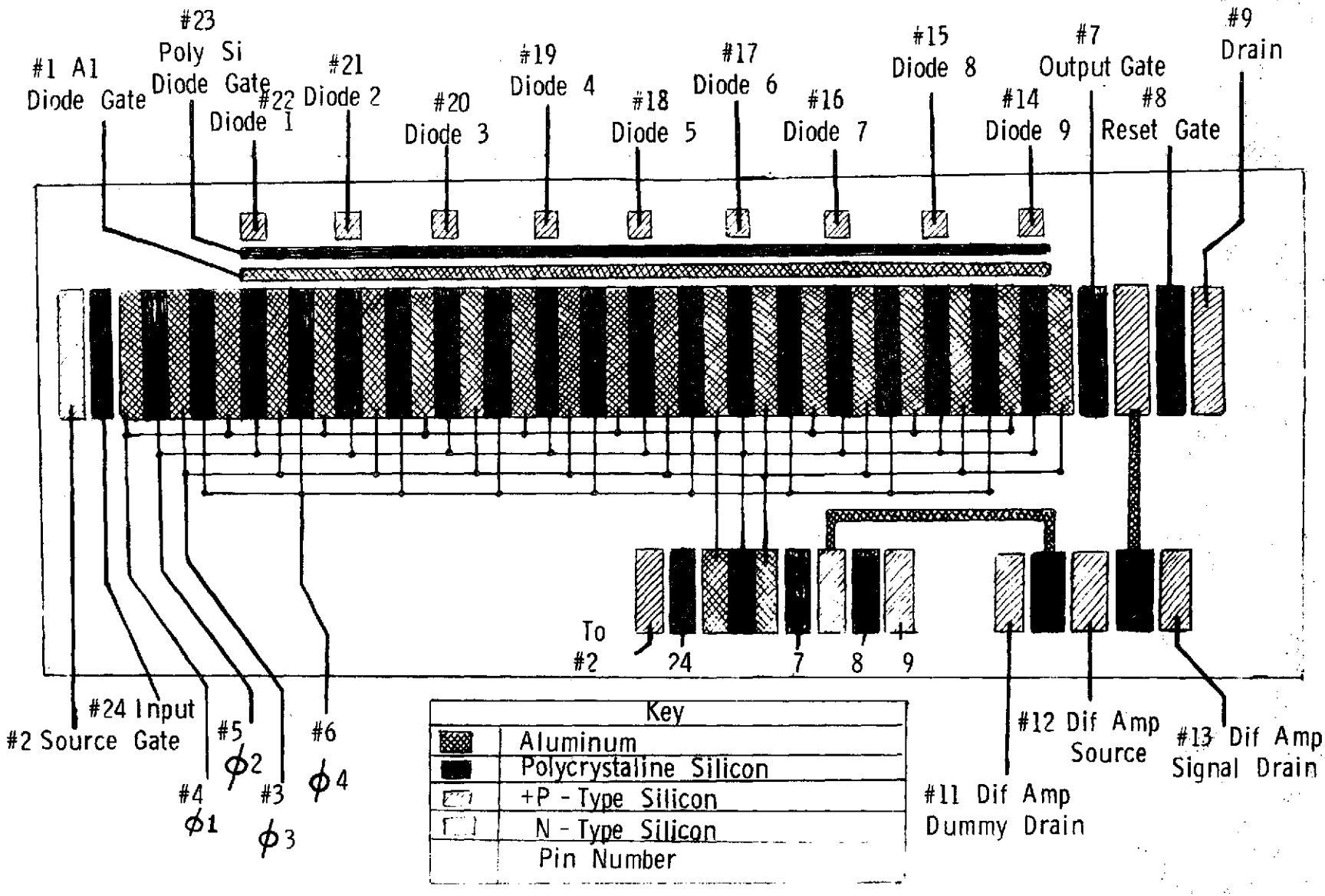

Figure B-1 9-BIT CCD DELAY LINE DIAGRAMATIC CONSTRUCTION

input diode gates, located similar to the polysilicon diode gate in Figure B-1 except that each one is individually accessible. The input technique used involves setting the charge level under a second input gate adjacent to the register by withdrawing the charge from that gate area until its silicon surface potential equals that of the input gate. The stored charge is emptied into the register as the adjacent $\emptyset 1$ gate creates a deep potential well and is transferred from the register by the $\phi 1$ and $\phi 2$ phased potentials at a clock rate compatible with the system's scan rate until it has been withdrawn through the on-chip MOS transistor to the preamplifier. After all of the charge from all the diodes has been serially transferred out of the device, another parallel to series multiplex operation may begin. This process requires that the device function at a clock frequency

$$f_c = \frac{69}{(60\ \mu s)\ t_{scan})}$$

where 1/60 μs is the rate at which each detector is scanned and t_{scan} is the time required to scan the array. Figure B-2 illustrates the input pulse timing sequence.

The CCD would be mounted on the focal plane immediately adjacent to the detector array to minimize feedthrough heat leads and for additional compactness a MOS buffer amplifier between the detector and CCD could be integrated within the CCD's substrate to provide any additional required signal gain.

The starting point to determine the system's ability to function is the depletion approximation from which we relate the charge introduced, Q_s, to the input signal, V_s:

$$Q_s = C_o\ A_g\ V_s \tag{B.1}$$

and a MOS structure surface potential, ϕ_s, for an applied potential V_G

$$\phi_s = V_G - V_{FB} + \frac{\sigma}{c_o} + \frac{\epsilon_{sq}\ N_D\ t_{ox}}{\epsilon_{ox}\ c_o} \left[\sqrt{1 - \frac{2c_o\ \epsilon_{ox}}{\epsilon_{sq}\ N_D\ t_{ox}}\ V_G - V_{FB} + \frac{\sigma}{c_o}}^{-1}\right] \tag{B.2}$$

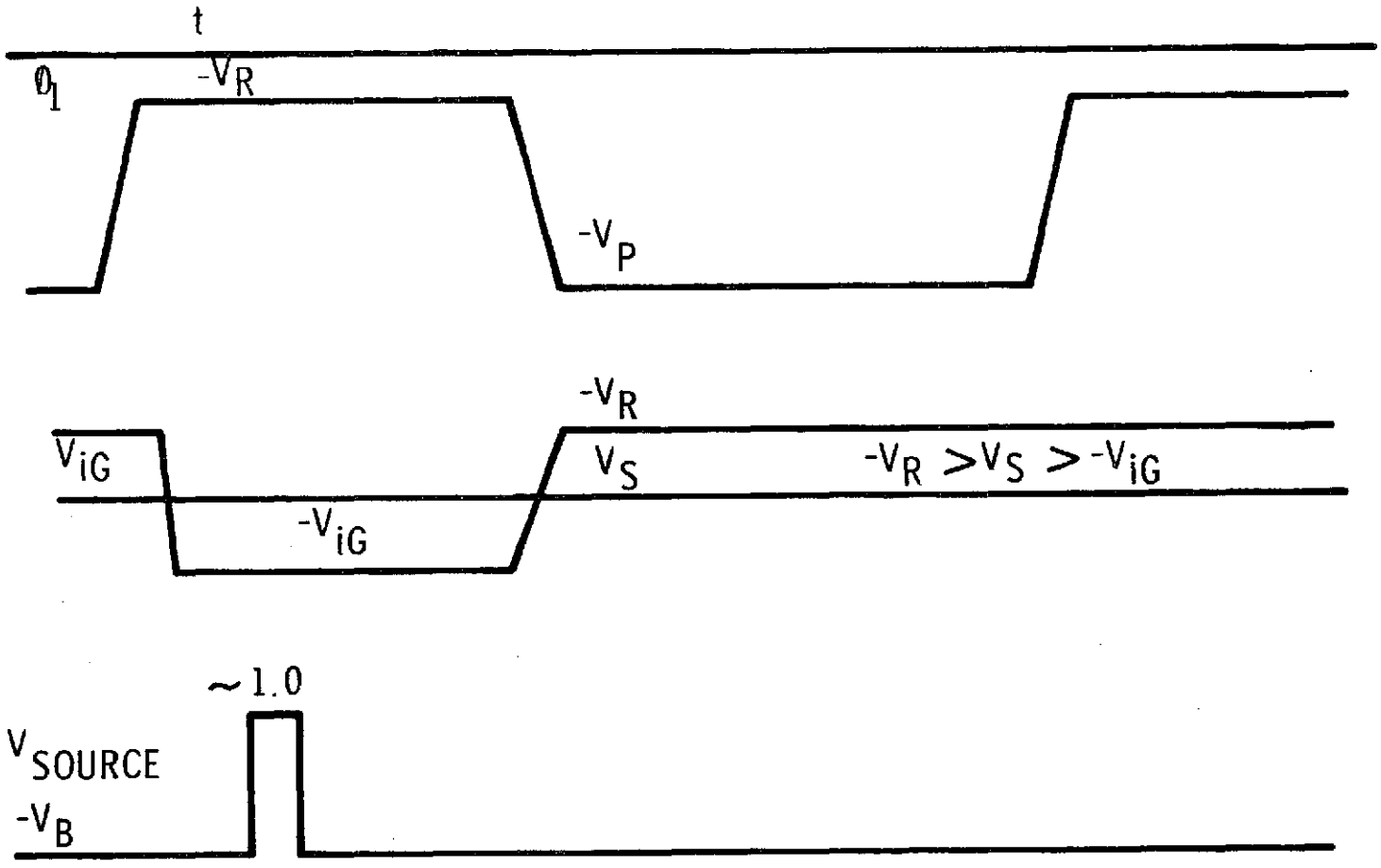

Figure B-2 INPUT TIMING DIAGRAM

when V_{FB} = flat band voltage

C_o = oxide capacitance/cm^2 = $\frac{\epsilon_{ox}}{t_{ox}}$

A_g = gate area

σ = mobile surface change density

N_D = silicon doping level

t_{ox} = oxide thickness

$\epsilon_{s,\ ox}$ = dielectric control of silicon and oxide

V_T = threshold voltage

The surface potentials for a 1100 and 3000 Å oxide structures are plotted in Figures B-3 and B-4, respectively. The family of curves represent the percent of maximum possible mobile charge, where

$$\sigma_{max} = c_o\ (V_G - V_T)$$

B.2.1 Maximum Signal

Unidirectional charge flow in a two phase device [2] is achieved by maintaining a surface potential barrier to charge flow under the thicker oxide gate structure. The condition which determines the maximum charge capacity of the two phase device is that the surface potential of the thin oxide structure, the charge storage location, may never exceed the potential of the thick oxide. Figure B-4 indicates that a 20-volt gate voltage applied to the thick oxide structure will result in ϕ_s = -11.65 V which, because of the aforementioned conditions, limits the charge level to σ_{max} = 5.4 x 10^{-7} coulombs/cm^2 for the HRC device Q_{max} = 5.4 x 10^{-12} Coulombs. From reference 1 we see that $|V_{s\ max}|$ = 1.78 x 10^{-4} V/ input gate area. Typically, we would expect $|V_{s\ max}| \simeq$ 15 volts. Thus, the maximum input signal the device may accept is greatly in excess of what we would expect from the detectors.

B.2.2 Minimum Signal

The minimum input signal which can be processed through the CCD is determined by its attenuation per transfer of the charge packes and the charges introduced into the packet due to the CCD noise sources. Since for each transfer some charge is not transferred

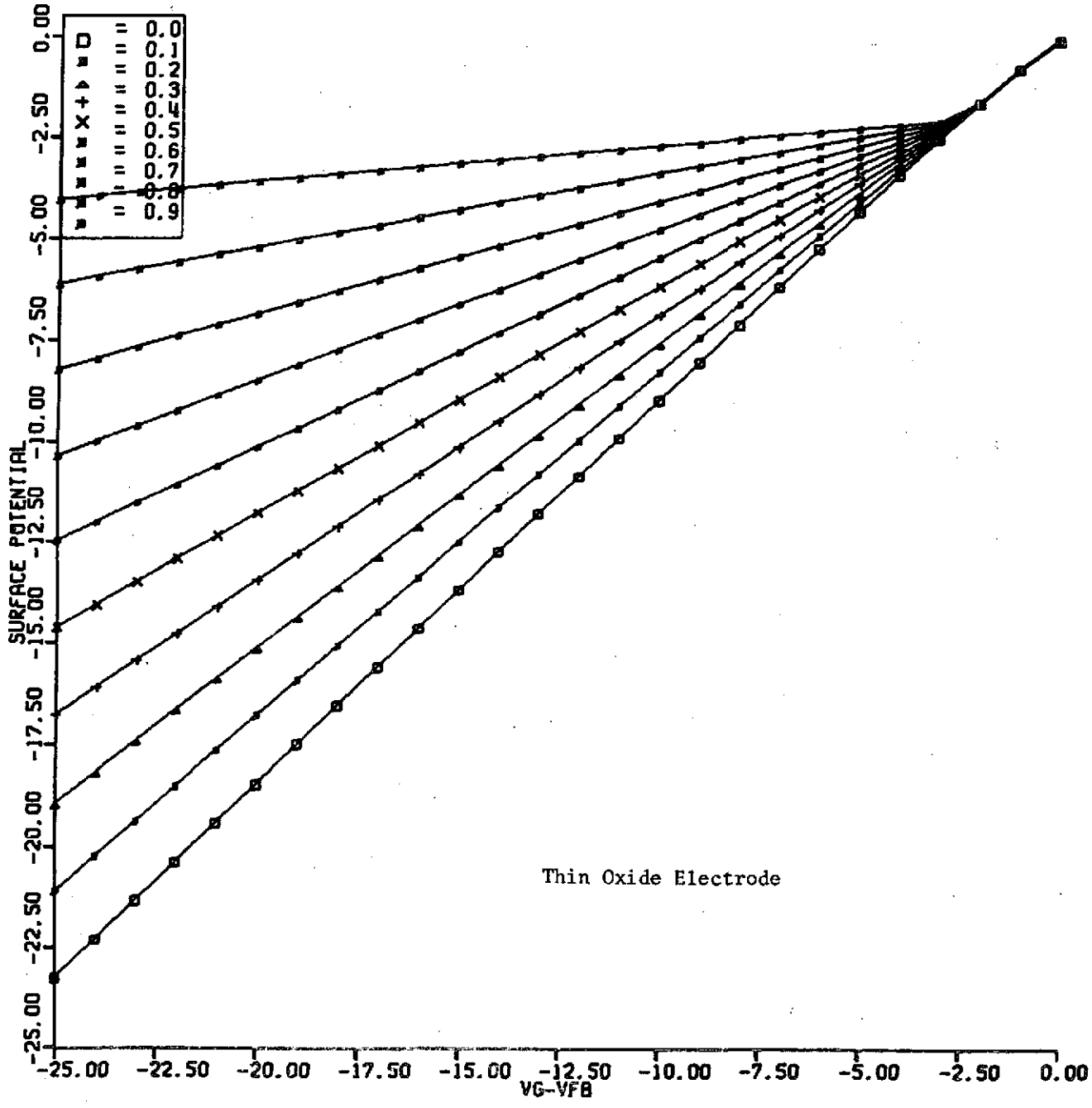

Figure B-3 SURFACE POTENTIAL OR A FUNCTION OF APPLIED POTENTIAL

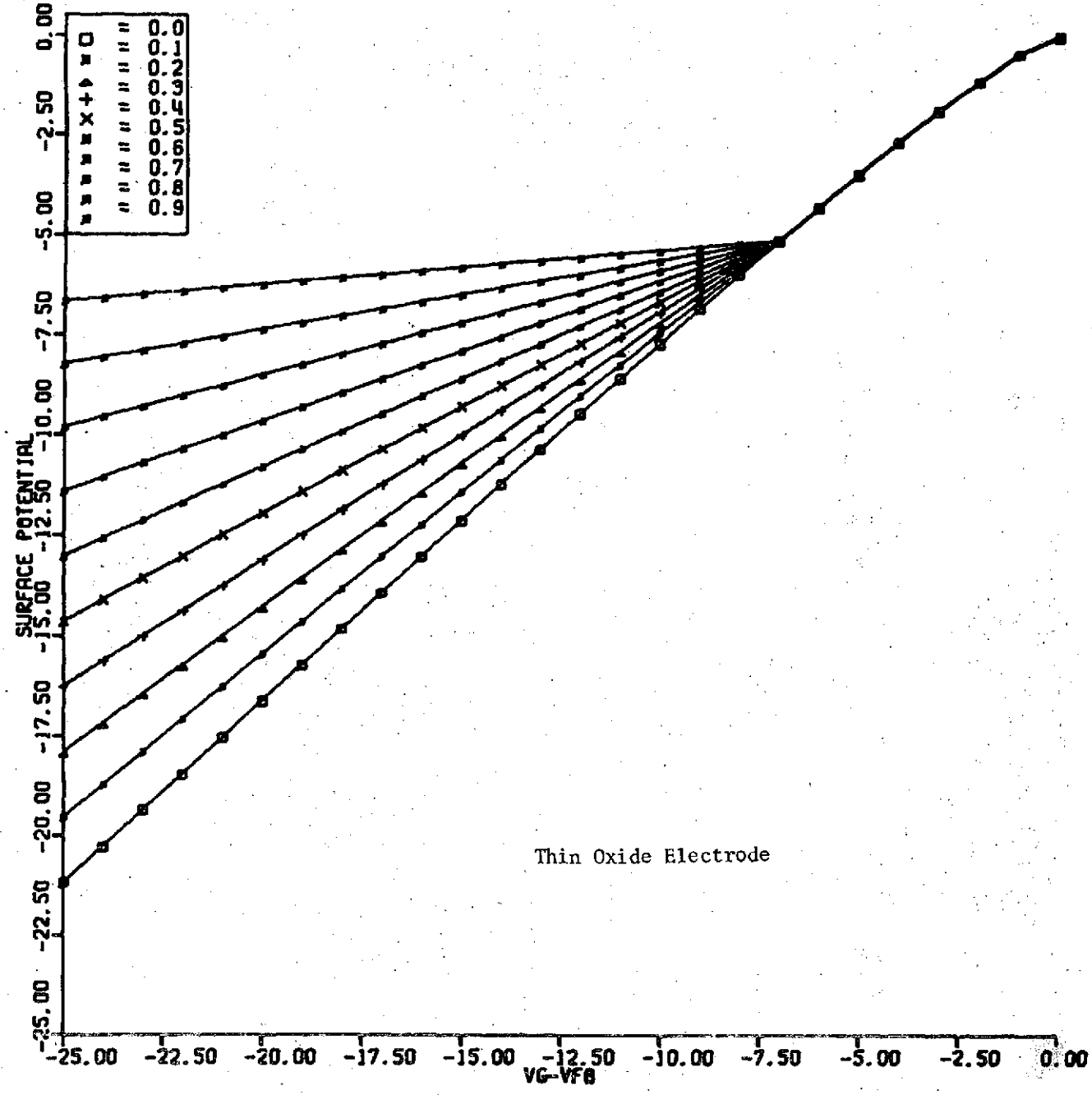

Figure B-4 SURFACE POTENTIAL AS A FUNCTION OF APPLIED POTENTIAL

to the next well we define the ratio of charge not transferred to total charge as ϵ, so that the final value of the packet is:

$$Q = Q_o \ (1-\epsilon)^{2N_B} \tag{B.3}$$

where Q_o = initial charge level

N_B = number of elements (the 2 in the equation is included to account for the two transfers per bit)

B.2.3 Transfer Efficiency

Since transfer efficiency is a parameter dependent upon the time during which charge transfer may take place, due to device design considerations, it is usually defined for a given clock frequency. However, current state-of-the-art devices exhibit transfer efficiencies which are essentially constant for clock rates up to 6 MHz; thus, for this purpose of this study we take ϵ to be a constant. The ratio of Q/Q_o is plotted in Figure B.5 for various transfer inefficiencies and element sizes and we see that for a 64-element device we require $\epsilon < 1 \times 10^{-4}$ if we are to maintain less than a one percent difference in signal values between the first and last element. Transfer efficiencies of 0.9999 are attainable at the expected clock rates although special device and processing techniques may be required [3].

B.2.4 Noise Sources

The other limitation to the minimum signal which can be processed is CCD introduced noise. The basic CCD noise sources, expressed in terms of noise charge numbers, are [4]

$$\text{Input noise} = n_1^2 = kT\ C/q^2 \tag{B.4}$$

$$\text{Transfer noise} = n_2^2 = 2\epsilon\ N_B\ N_S \tag{B.5}$$

$$\text{Interface state noise} = n_3^2 = 2.8\ kT\ N_B\ A_G\ N_{SS} \tag{B.6}$$

$$\text{Reset noise} = n_4^2 = kT\ C^1/q^2 \tag{B.7}$$

$$\text{Output noise} = n_5^2 = C_o^2\ 4\ kT\ \Delta f/q^2\ g_m \tag{B.8}$$

where C = capacitance of input gate

N_S = number of charges initially in packet

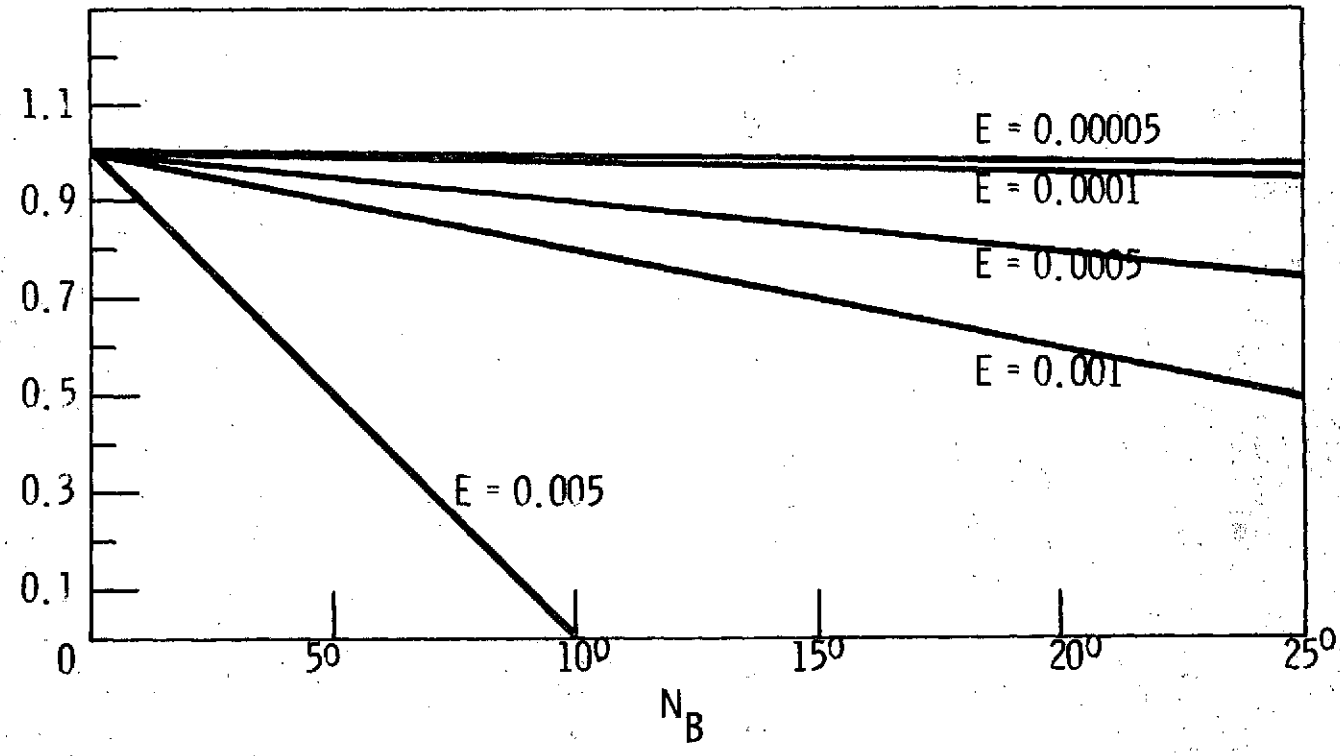

Figure B-5 TOTAL CHARGE TRANSFER AS A FUNCTION OF NUMBER OF ELEMENTS

N_{SS} = density of silicon - silicon dioxide interface state

C^1 = capacitance of reset gate and floating diffusion

C_g = capacitance of MOS transistor gate

g_m = MOS transistor transconductance

Δf = signal bandwidth

The signal-to-noise ratio at the CCD output as a function of the input diode position is:

$$\frac{S}{N} = \frac{(1 - 2 N_B \epsilon) Q_i}{\left(n_1^2 + n_2^2 + n_3^2 + n_4^2 + n_5^2\right)^{1/2}} \qquad (B.9)$$

We will calculate the S/N assuming a 50% of maximum charge level since the transfer noise is dependent upon the charge level. Using the data of Table B.1 we find the various noise sources contribute as follows:

$$n_1^2 = 47.5 \times 10^3$$

$$n_2^2 = 216 \times 10^3$$

$$n_3^2 = 447 \times 10^3$$

$$n_4^2 = 47.5 \times 10^3$$

$$n_5^2 = 0.02 \times 10^3$$

In Figure B-6 we show the total number of noise charges, N_T, in the output signal as a function of elements and Figure B.7 shows the signal-to-noise ratio, ρ, as dependent on element number. This information can then be used to estimate the effects of signal degradation as a function of input diode position. Note that the curves slope decreases as N_B increases since for large values of N_B the S/N $\alpha N_B^{1/2}$. The minimum input signal which the device can process above its noise level is found from (B.10)

$$V_{S\,min} = \frac{\frac{2\epsilon N_B C}{q} + \sqrt{\left(\frac{2\epsilon N_B C}{q}\right)^2 + 4C^2(1-2N_B\epsilon)^2\left[\frac{kT}{q^2}(C+C^1+C_{\frac{q}{gm}}^2 4\Delta f) + 2.8kTN_{SS}N_B A_S\right]}}{2\epsilon^2/q^2(1-2N_B\epsilon)^2}$$

TABLE B.1

Symbol	Definition	Volume	Units
C	Input gate capacitance	0.19	pf
C^1	Reset plus floating diffusion capacitance	0.3	pf
C_g	MOS transistor gate capacitance	0.24	pf
gm	MOS transistor conductance	1.25×10^{-3}	mhos
Δf	Bandwidth	2	MHz
N_{SS}	$Si-SiO_2$	1×10^{10}	$(cm^2\text{-}eV)^{-1}$
N_B	Substrate doping density	4×10^{14}	cm^{-3}

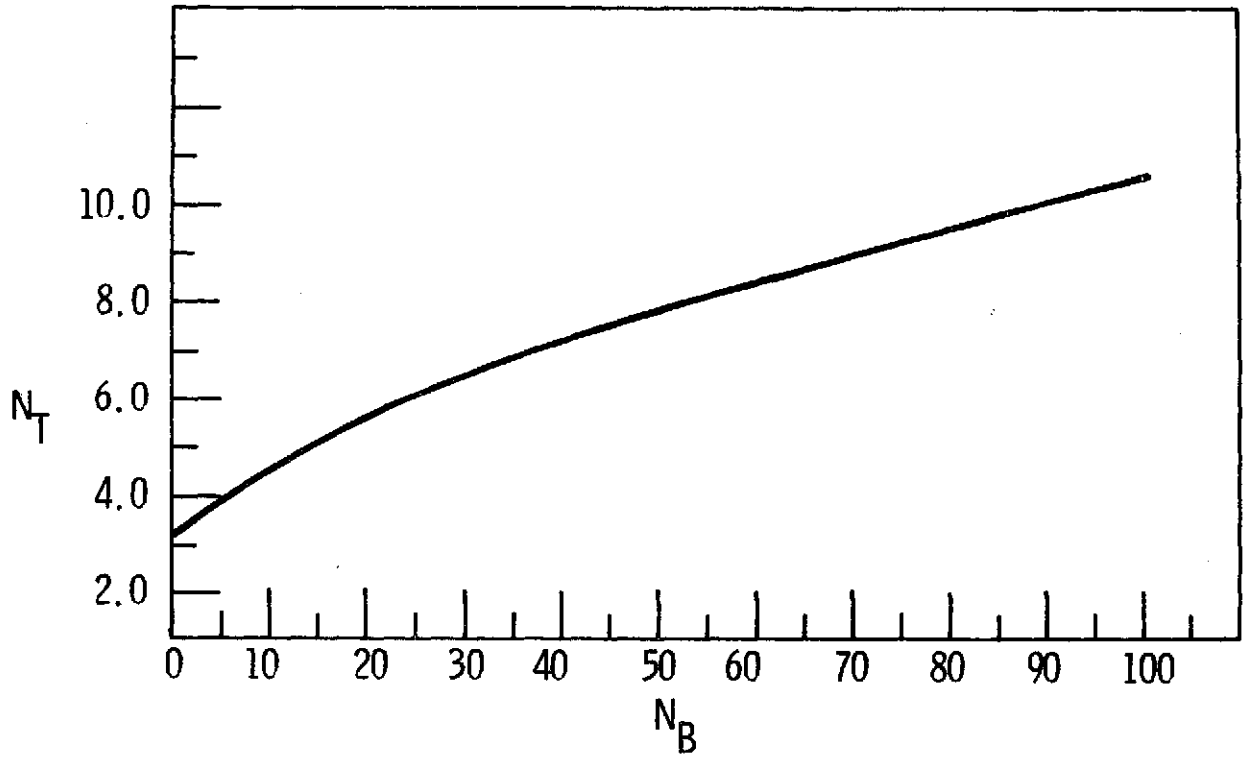

Figure B-6 NOISE CHARGES IN OUTPUT SIGNAL AS A FUNCTION OF NUMBER OF ELEMENTS

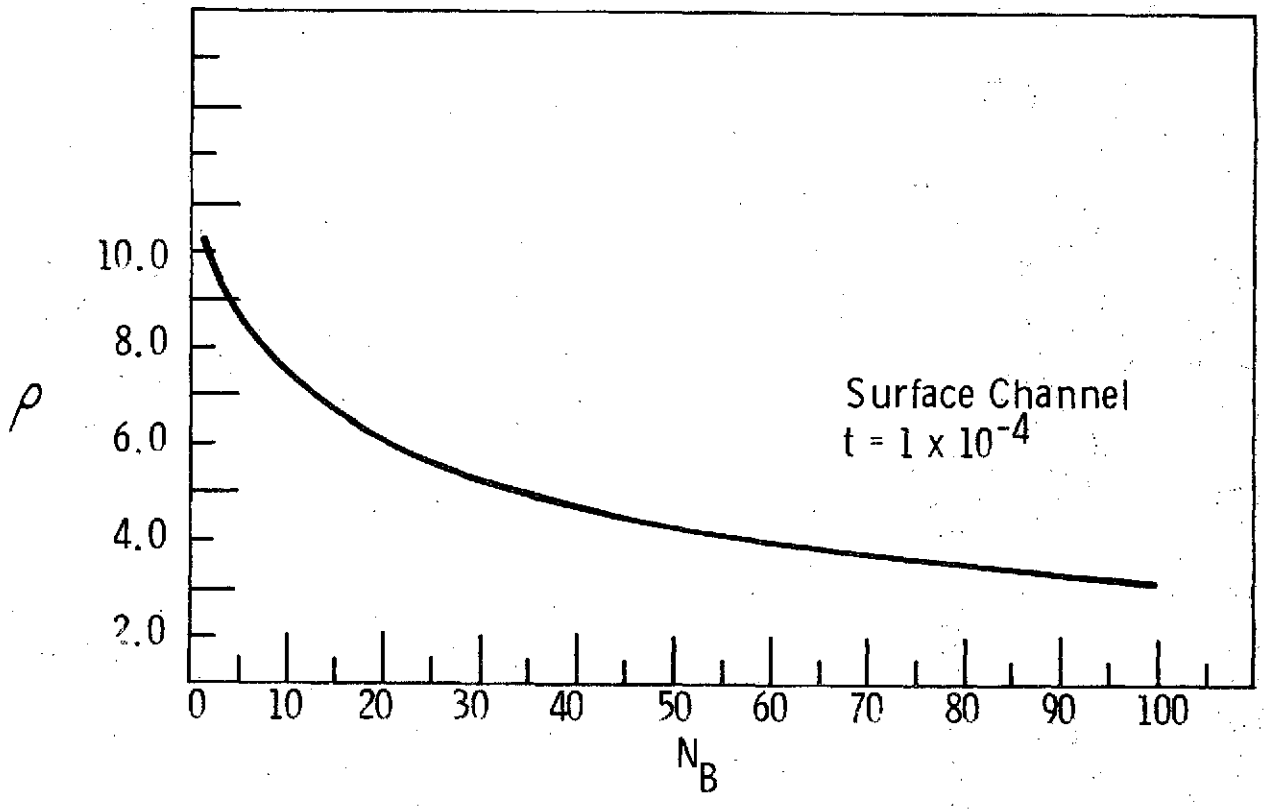

Figure B-7 SIGNAL-TO-NOISE RATIO AS A FUNCTION OF NUMBER OF ELEMENTS

which for the parameters listed in Table B.I is 350 μV. Thus, for the detectors being considered a buffer amplifier integrated on the chip will be required.

B.2.5 Power Considerations

The CCD power consumption per electrode is

$$P = A_G \sigma_{max} V_G fc \qquad (B.11)$$

which for the device structure in Table B.1 operating at 1 MHz is 20 μW per element. Thus a 64-element device would consume approximately 2.5 mW; considerably less than the power dissipated in a typical long wavelength photoconductive detector. Whether it is advantageous to mount a CCD on the cold plane to minimize feedthrough heat leaks can be found by considering the number of feedthroughs which can be saved as a function of the array size. Figure B-8 illustrates this comparison where we assumed a 100 μW heat leak per feedthrough so that for an array greater than 12 detectors it becomes advantageous to mount the device on the cold plane.

B.2.6 Packaging

The device space requirements are determined primarily by the interconnections scheme chosen because each element occupies less than 2.5×10^{-6} cm^2 and a 64-element shift register would be 0.1×0.0005 cm^2. Conventional bonding pads plus support circuitry would increase the device size to no more than 0.25×0.075 cm^2. Thus a well designed interconnection scheme would permit the device to be mounted on the cold plane immediately adjacent to or attached with the detector array. A flip-chip bonding system is illustrated in Figure B-9 where low temperature solder contacts are deposited on the CCD contact. The CCD is inverted, placed on the detector array and a circuit board which provides the CCD clock pulses, power and signal output leads. Then the entire system is heated so that solder reflows and forms the interconnections. Low temperature solders compatible with (Hg,Cd)Te have been developed and their feasibility demonstrated in HRC's laboratories.

B.2.7 Temperature Effects

There are advantages to low temperature CCD operation as can be seen from a consideration of the temperature dependence of the CCD noise sources. Although the noise introduced by transfer inefficiency appears as a temperature independent factor it is also

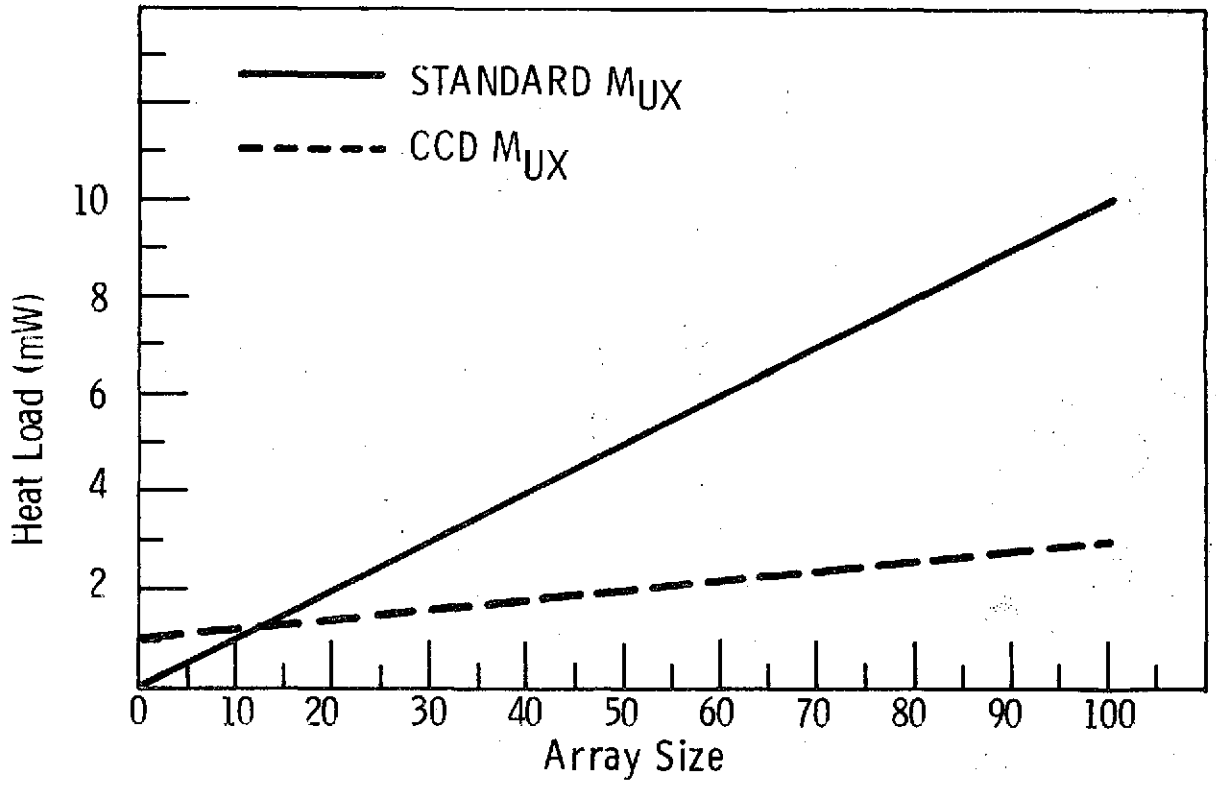

Figure B-8 HEAT LOAD AS A FUNCTION OF ARRAY SIZE

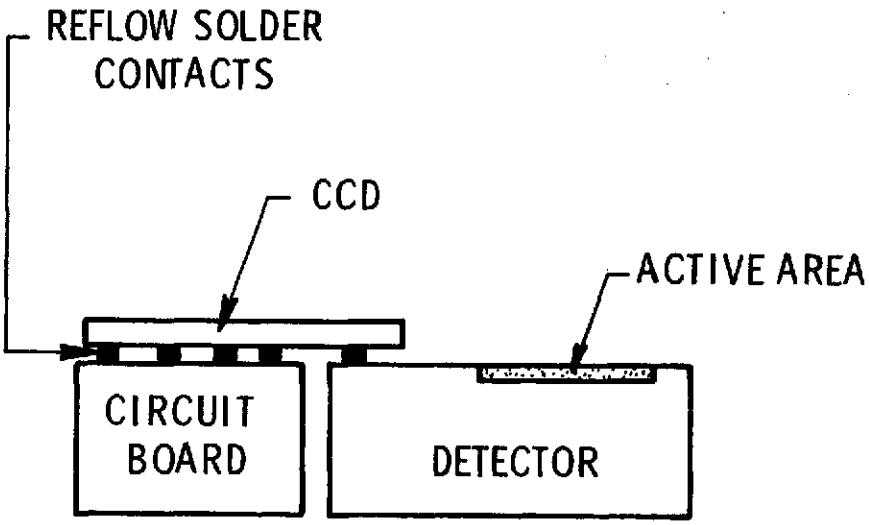

Figure B-9 FLIP CHIP CCD-DETECTOR SYSTEM

temperature dependent because transfer inefficiency decreases at lower temperatures. Increased charge mobility and longer silicon - silicon dioxide trap occupation times are the chief factors involved in ϵ's temperature dependence. For example, on typical devices we have measured a 25% decrease in transfer inefficiency when the device was operated at 77 °K. An additional advantage of low temperature operation is improved dc stability since oxide charge redistribution effects are suppressed.

B.2.8 Buried Channel

In considering CCD parallel to series multiplexing of a 64-element detector array we choose device parameters which are typical of today's surface channel devices. Two parameters are of particular importance, transfer inefficiency and the interface state density since they are the source of both signal attenuation and signal-to-noise dependence on the input element location. This suggests that a buried channel [5] CCD would be a more appropriate device because in a buried channel the charge is transferred within the silicon bulk so that signal charge interactions with the surface do not take place. Fringing field effects and the lack of the surface state interactions also increases the transfer efficiency. Thus in a buried channel CCD one noise source is completely eliminated and a second is significantly reduced. A buried channel device noise analysis similar to the preceeding in which we assume a 5×10^{-5} transfer inefficiency is summarized in Figure B-10 and indicates a significant reduction in S/N dependence on input element location. Clearly, except for a particular case which requires the larger dynamic range of the surface channel, a buried channel device is superior.

If we wish to extend this system to a linear array of 6000 elements or more, we would determine the most convenient detector module size based upon yield and cost considerations. A CCD, compatible with the detector array's size and a number of elements would then be designed. The detector array D* uniformity will, in all probability, be the dominating factor since even for CCD's in excess of 100 elements, the CCD properties will be the more uniform of the two devices.

B.2.9 Summary

This analysis indicates that buried channel CCD technology, combined with a well designed detector array - CCD interconnection system, should be used to access long detector arrays. A low noise input technique exists, a cell diagram of which is illustrated

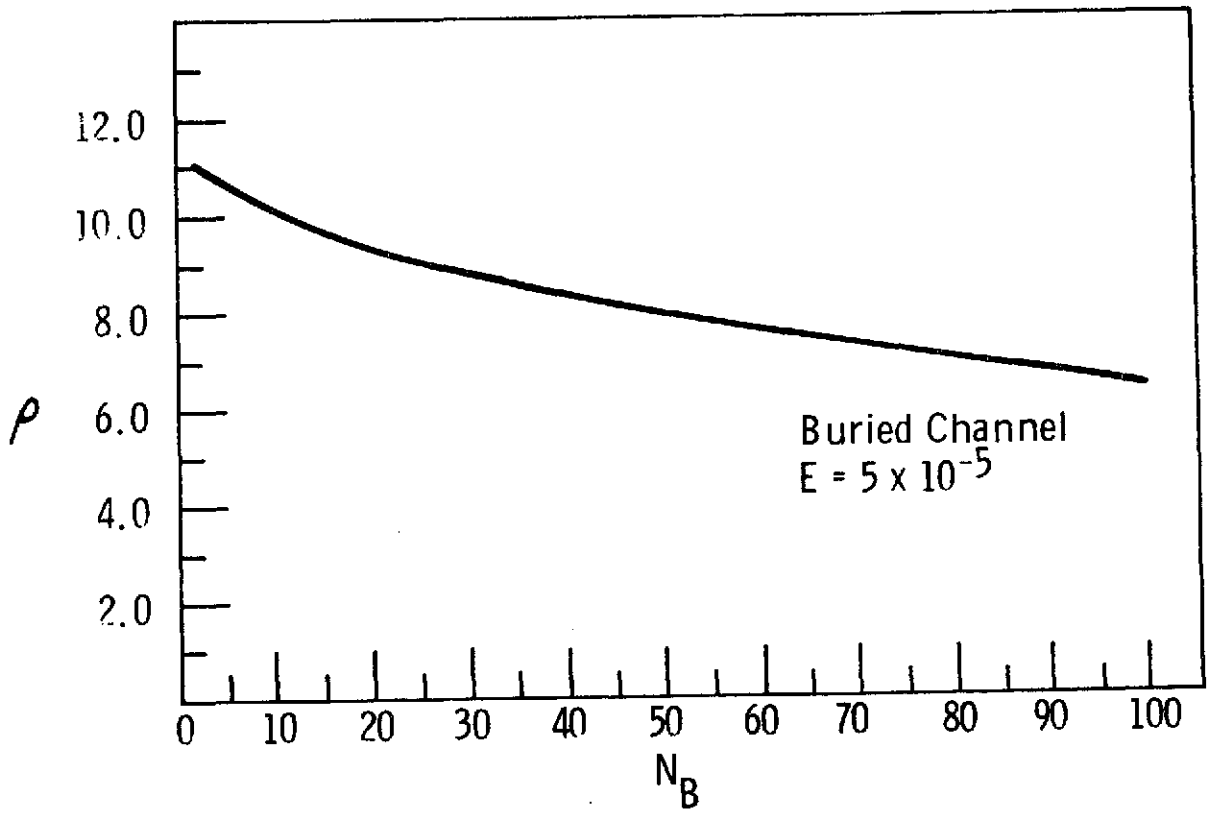

Figure B-10 SIGNAL-TO-NOISE RATIO AS A FUNCTION OF NUMBER OF ELEMENTS

in Figure B-11, which sets the charge in the CCD's register in a manner independent of threshold shifts; thus the technique is stable to long term drift. Since a buffer amplification stage is required between a detector and its CCD input, design and experimental work is required to properly integrate the amplifier on the CCD substrate. The signal to noise degradation due to CCD processing would be well within acceptable limits for devices with high transfer efficiencies. For reasons of compactness power dissipation and device performance, it is desirable to mount the CCD within the cold plane and preferrably on the detector array using a system similar to that exhibited in Figure B-9. Finally, the CCD would contain the same number of elements as the detector array which would be divided into modules.

B.3 NINE CHANNEL CCD

The HRC-CCD, designed with and fabricated at Honeywell's Solid State Electronics Center, is the key component of our Electronically Scanned Array Program. With the receipt of a small initial shipment from SSEC, we set out to determine device no. 1's general operational characteristics so that, from these results, we could define a more comprehensive device characterization program. This section summarizes operational characteristics of the CCD.

B.3.1 Device Design

The chip design includes the following devices, individually addressable and integrated within one chip:

1. 9 bit - 4 (2) ϕ floating diffusion output
2. 9 bit - 4 (2) ϕ floating gate output
3. 9 bit - 3 ϕ floating diffusion output
4. 128 bit - 4 (2) ϕ shift register
5. 32 bit - 4 (2) ϕ shift register
6. 32 bit - 3 ϕ shift register
7. MOST test device

Since standard dual in-line packages have limited number of leads, it is impractical to bond more than one 9-bit device. We chose to have the 9-bit 4(2)ϕ floating diffusion device bonded at SSEC.

B.3.2 Structure of the 9-Bit CCD Delay Line

The 9-bit CCD analog delay line is represented diagramatically in Figure B-1. This CCD structure can be partitioned in six functional areas: 1) fat zero input; 2) the shift register; 3) the

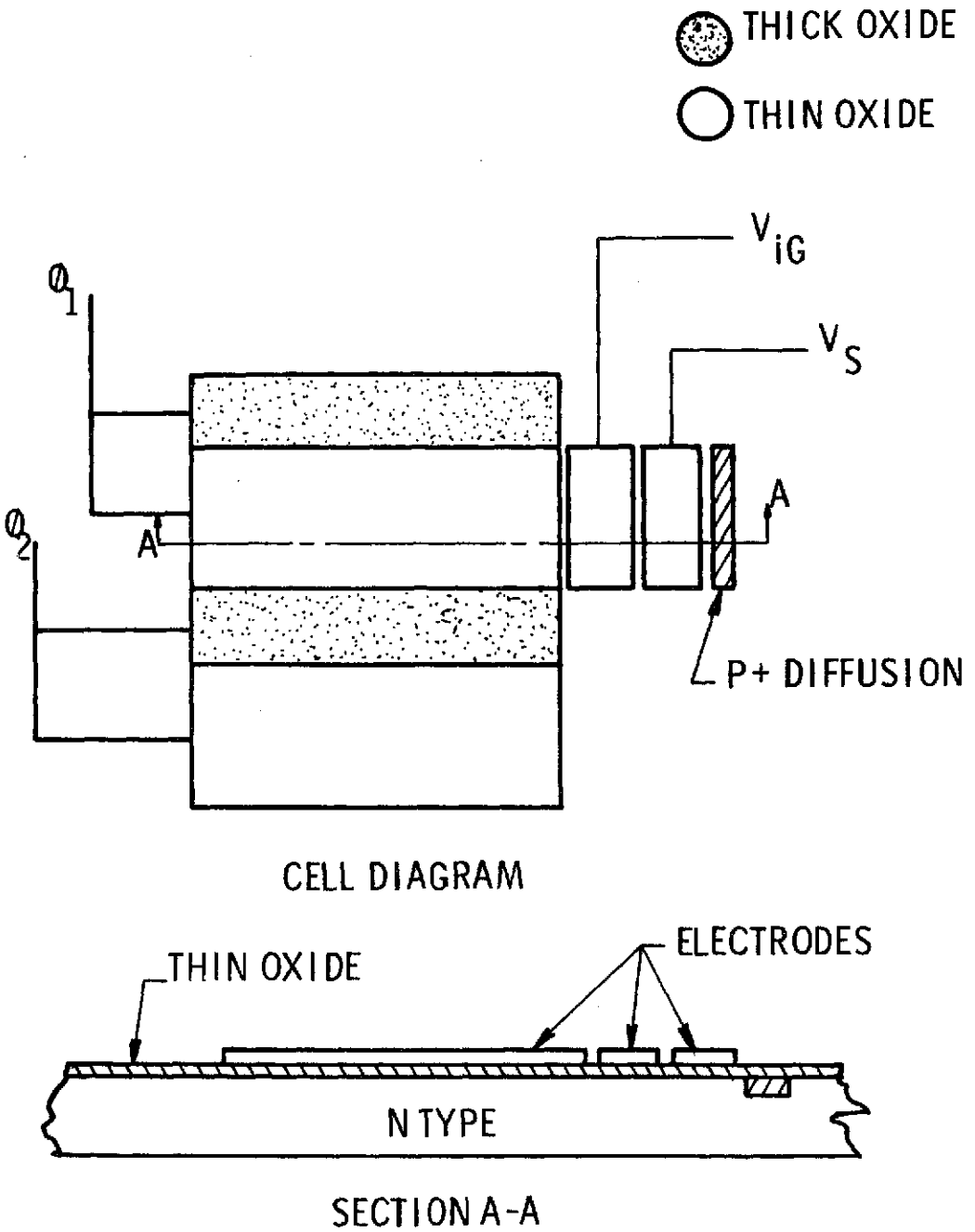

Figure B-11 LOW NOISE INPUT TECHNIQUE

input diodes and diode gates; 4) the output region; 5) the MOSFET; and 6) the dummy register. The substrate is common to all the areas.

The fat zero input structure consists of a +P source diffusion and a polysilicon input preceding the shift register. This device construction is shown in Figure B-12. Holes, the charge carriers in this device, are supplied by the source diffusion. The flow of holes from the source into the register is determined by the potential difference between the source and surface potential beneath the first ϕ_1 electrode, and the conductance of the channel between the source and the register. The input gate's voltage controls the channel conductance in the same manner as the gate of a MOSFET.

The shift register, as depicted in Figure B-13 consists of a linear array of MIS capacitors. This array is composed of two distinct types of capacitors, those with polysilicon as the upper capacitor plate and those with aluminum; the n-type silicon substrate serves as the common semiconductor surface for all the capacitors. The polysilicon plates are deposited on top of a 1100A layer of SiO_2. Then, an additional 1900A layer of SiO_2 is grown, on which the aluminum plates are deposited, overlapping part of the lower polysilicon plates. Every other polysilicon plate and every other aluminum plate is interconnected, giving four individually addressable groups of capacitors. By connecting the ϕ_1 aluminum capacitors to the ϕ_2 polysilicon capacitors, one produces a 2-step capacitor cell which we shall call $\overline{\phi}_1$. Likewise ϕ_3 and ϕ_4 capacitors are connected together to form $\overline{\phi}_2$ cells. When a negative voltage is applied to ϕ_1 or ϕ_2, a stepped surface potential well is produced so that by appropriately clocking ϕ_1 and ϕ_2, charge can be unidirectionally transferred down the shift register.

Figure B-14 depicts the structure of the input diodes and the diode gates. The input diodes provide nine different points along the register where charge can be entered and are in line with ϕ_2 plates of the shift register, so that the signal charge is injected into the register under the ϕ_2 plates. Channel diffusions, (not shown in the diagram), aid in confining the charge to travel in a narrow channel from the diode to the potential well beneath ϕ_2. There are two individually addressable overlapping diode gates, one polysilicon and one aluminum, which control the channel conductance between the input diodes and the shift register.

Figure B-15 shows the output region. The output region consists of a polysilicon output gate, a floating +P diffusion, a polysilicon

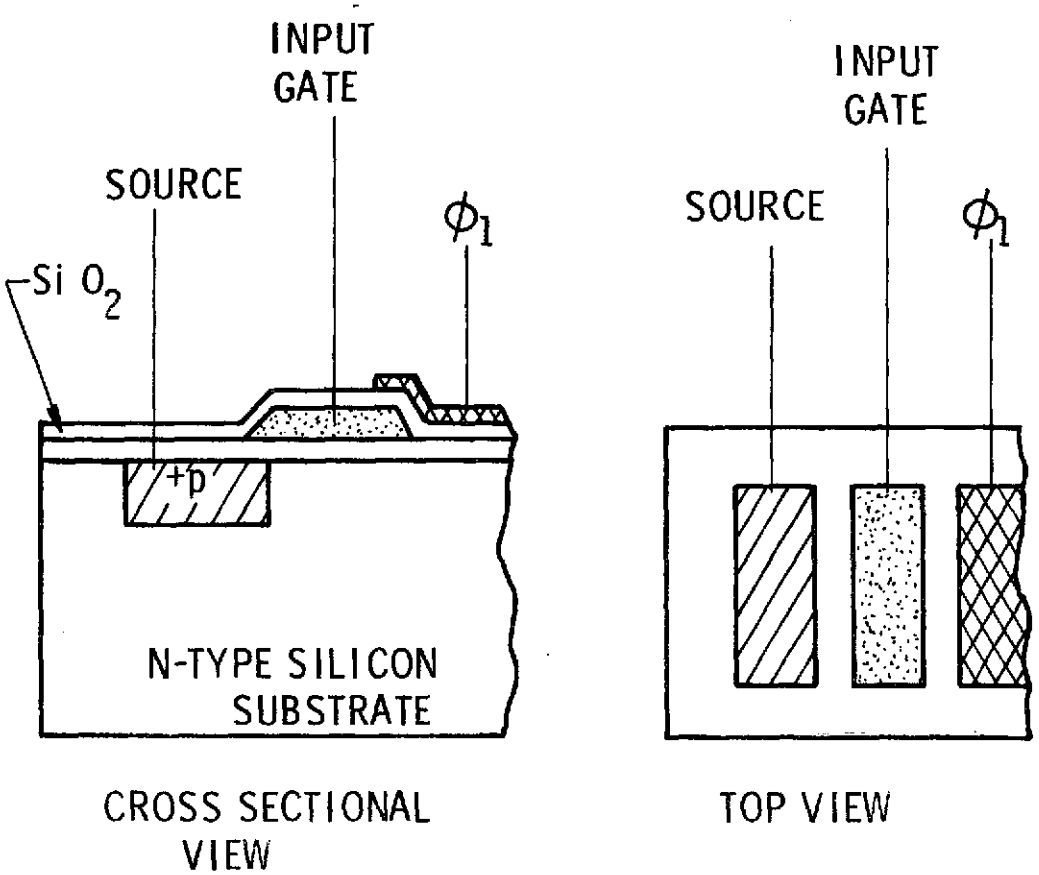

Figure B-12 FAT ZERO INPUT

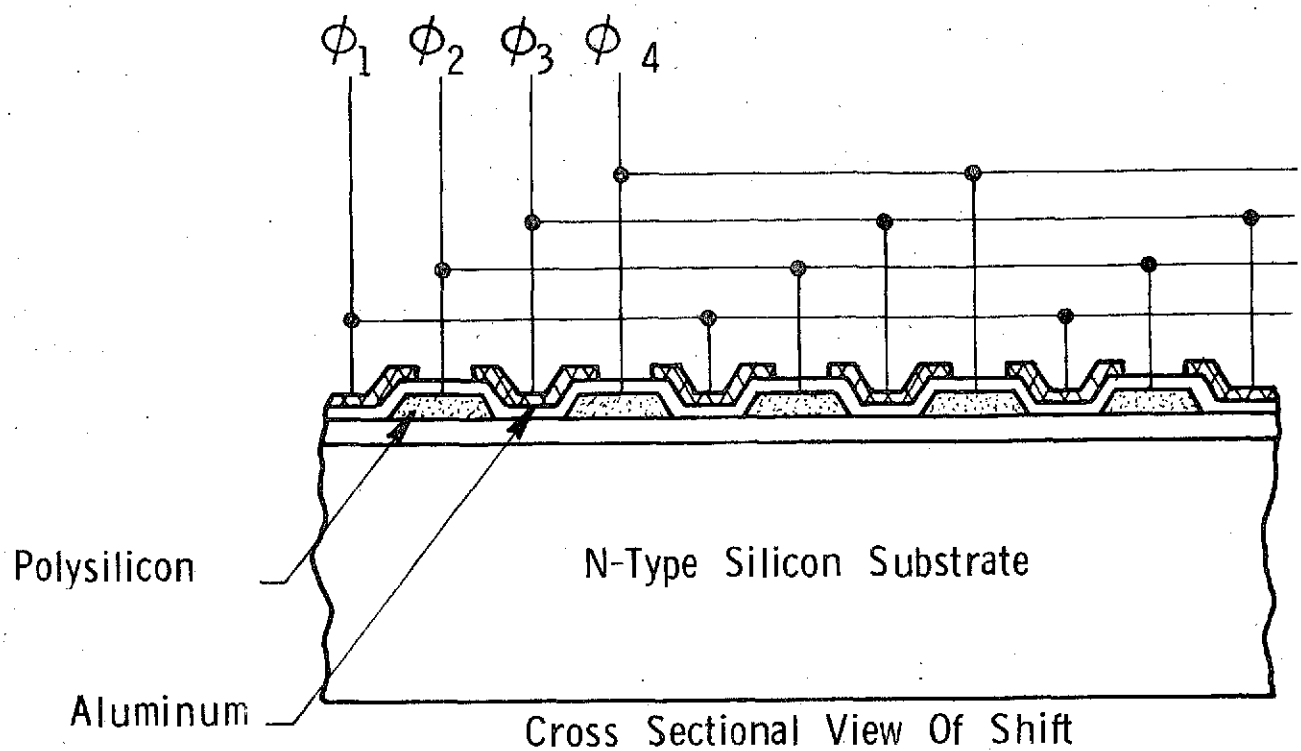

Cross Sectional View Of Shift Register MIS Capacitors

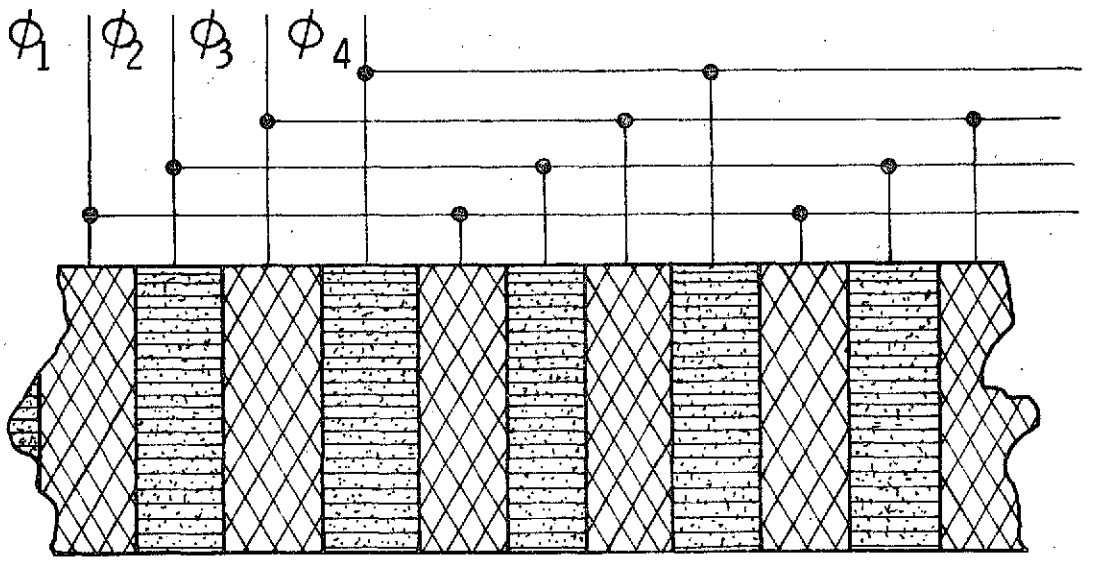

Top View Of The Shift Register's MIS Capacitors

Figure B-13

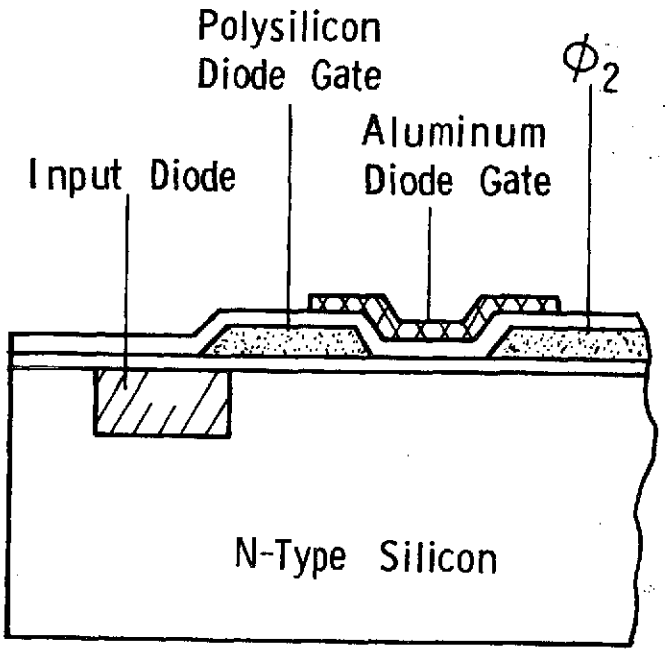

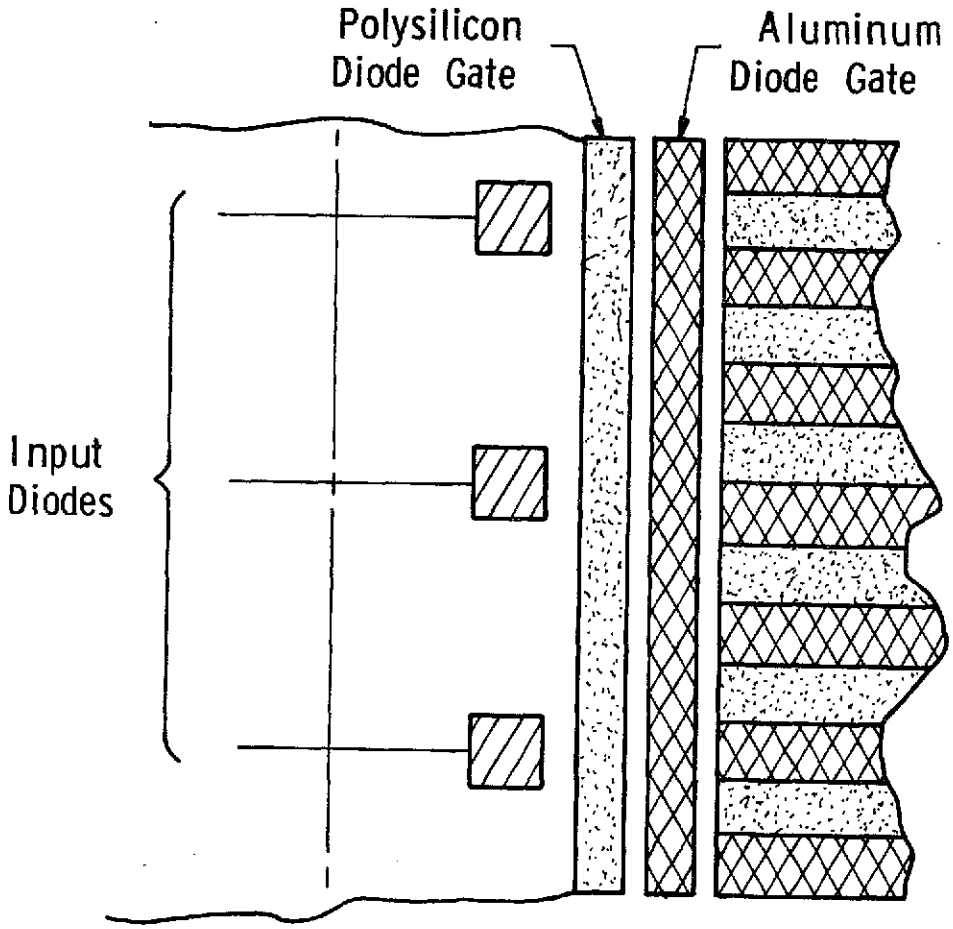

Figure B-14 INPUT DIODES AND DIODE GATES

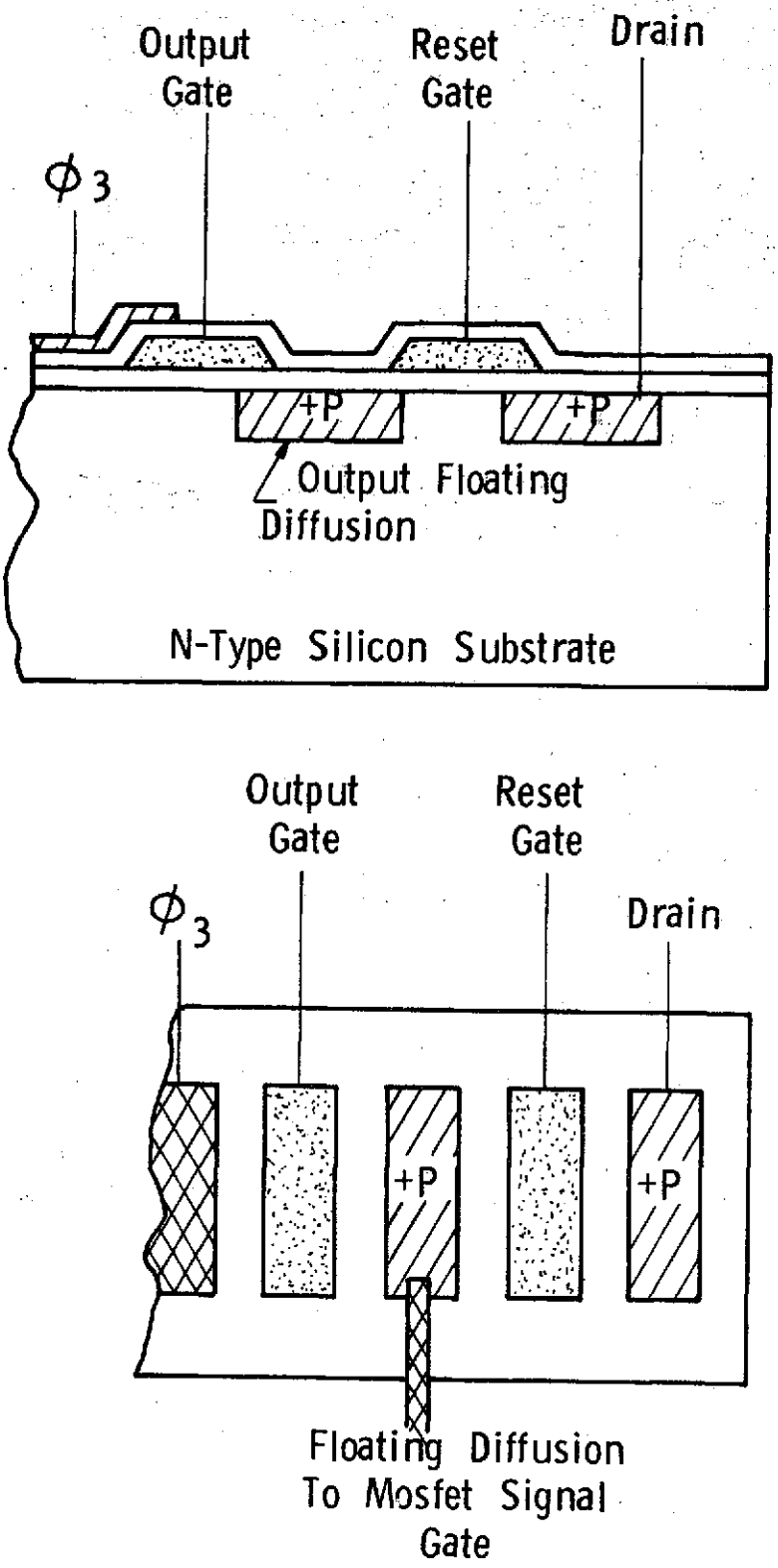

Figure B-15 CROSS SECTIONAL AND TOP VIEW OF OUTPUT REGION

reset gate and a +P drain diffusion. The floating diffusion is connected to the MOSFET signal gate. After signal charge is clocked down to the end of the register, it travels through a channel controlled by the output gate and into the +P floating diffusion. From the floating diffusion, the signal holes flow through a channel controlled by the reset gate into the back-biased drain. The voltage, with respect to the substrate, developed in the floating diffusion as a result of the passage of the signal holes through it, is used to modulate the gate potential of the MOSFET. The output signal is detected as either the current flow out of the drain to ground or as a current flow through the MOSFET.

The MOSFET is a two drain, common source FET as shown in Figure B-16. One side of this device is used to amplify the signal voltage developed in the floating diffusion output, while the other side is used to amplify the signal voltage developed in the dummy register. This way, the amplification of each signal is matched to the other, so that the output from the MOSFET can be used in a differential clock noise concellation manner.

The dummy register is pictured in Figure B-17. This dummy register is used to generate an output signal which duplicates the clock induced signal noise of the main shift register. The dummy register is a duplicate of the fat zero input, the last three shift register capacitor plates and the output region of the functional CCD. All of the dummy structures, except for the floating diffusion in the output, are internally interconnected to their respective structures in the functional CCD. Since is is presumed that the last three capacitor plates are the source of most all of the clocking noise, the dummy register should produce the same output voltage minus the injected signal produced by the main register. By taking the difference between the dummy output and the signal output, it should be possible to cancel the coherent clock noise.

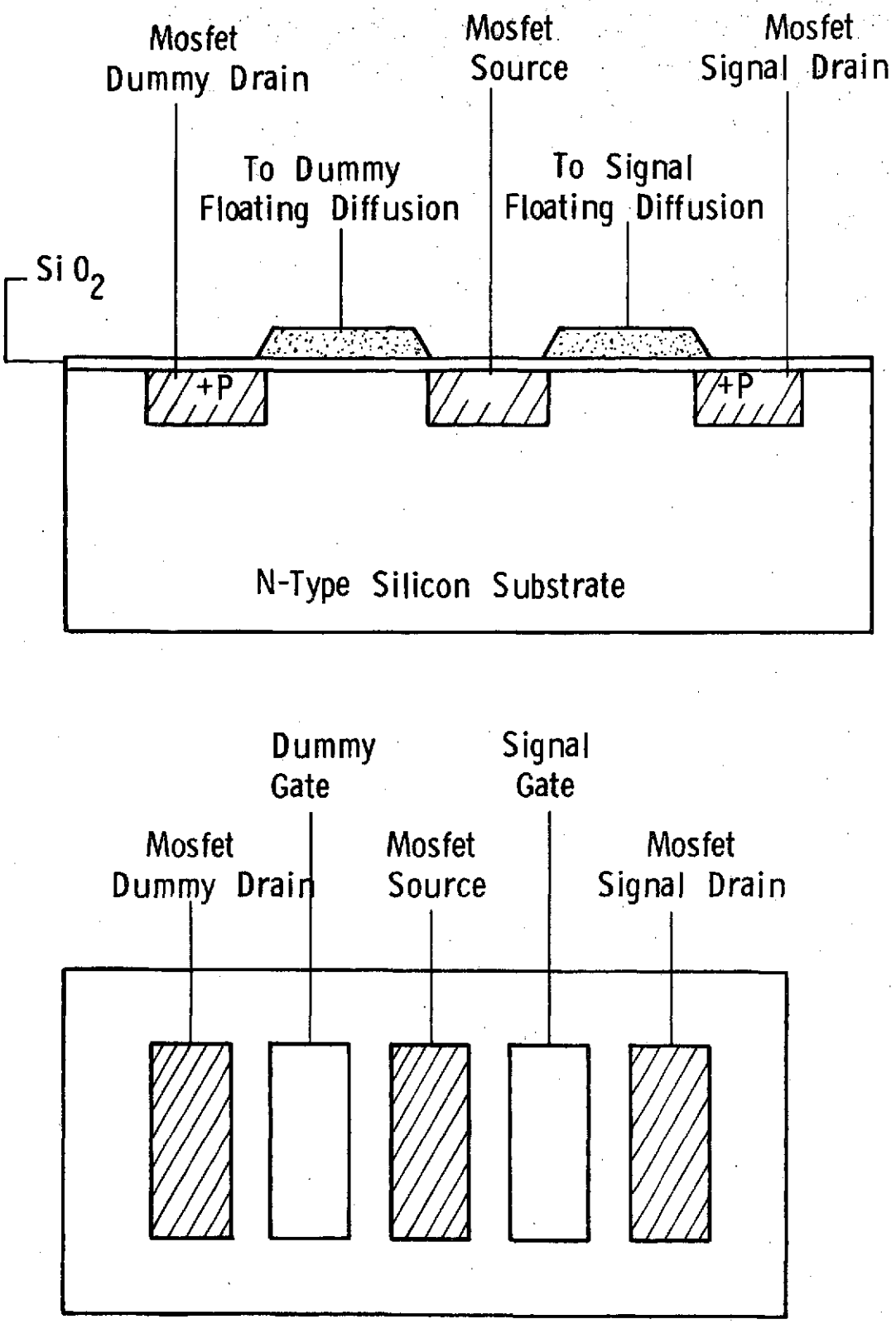

Figure B-16 CROSS SECTIONAL AND TOP VIEW OF THE MOSFET

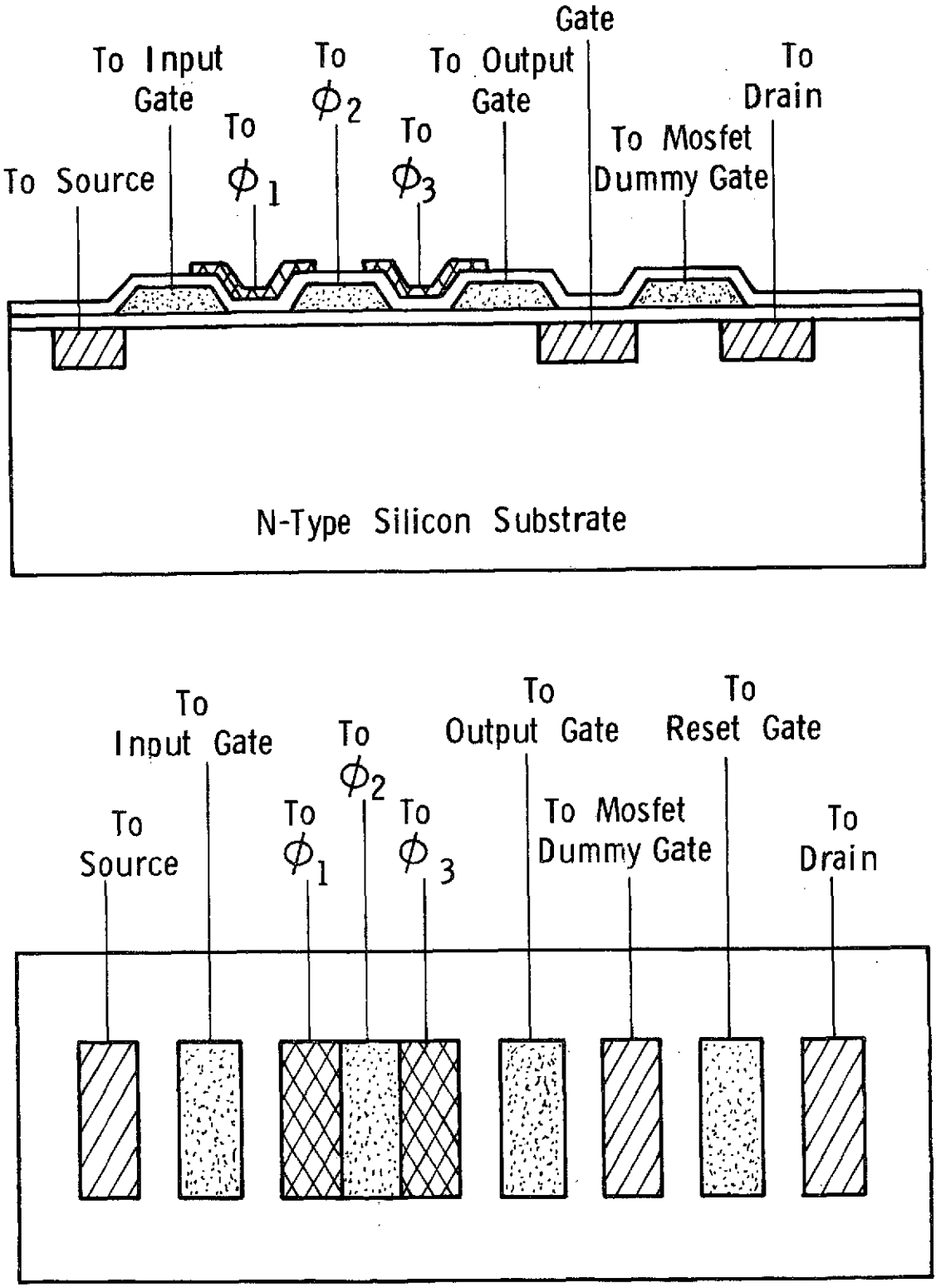

Figure B-17 CROSS SECTIONAL AND TOP VIEW OF DUMMY REGISTER

REFERENCES

1. M. Tompsett, Proc. CCD Applications Conf., San Diego, Calif., Sept. 18 - 20, 1972, pp 147 - 150.

2. W. Kosonecky and J. Carnes, RCA Review, Vol. 34, No. 1, p 164, March 1973.

3. S. Emmons and D. Buss, 1973 Device Research Conf., June 1973.

4. W. Kosonschy and J. Carnes, RCA Review, Vol. 33, p 327, June 1972.

5. C. Kim, Proc. CCD Applications Conf., San Diego, Calif., Sept. 18 - 20, 1972, pp 7 - 12.

APPENDIX C

EOS POINT DESIGN ANALYSIS

The objective of this study was to develop criteria for balancing the cost and complexity of a data acquisition instrument against the requirements of the user community. To do this effectively, it is necessary to have a reference instrument that serves as a datum point for the generation of tradeoff charts. The three EOS point designs were sufficiently different in their solution of the thematic mapper problem that it was not possible to select a single design as a representative instrument. Accordingly, a two-phase approach to generating a reference instrument was taken. The first phase was to analyze each of the three designs to determine the performance capability and high risk areas within each design. The second phase was to generate a set of instrument parameters based on a subjective average of the parameters of the three instruments.

As work progressed on the first phase, it became obvious that in many cases the point design reports did not contain sufficient engineering data to allow complete analysis of a particular item of interest. The scope of the contract precluded extensive inquiries to the originators of the point designs, therefore, one of the two following methods was used to handle an impasse. The most common solution was to indicate that, based on the prior experience of an engineer active in the appropriate discipline, the particular design element or design concept in question could be a problem and should be further analyzed. The rationale behind this procedure was to flag possible deficiencies in the various designs to prevent their incorporation into a reference design without the appropriate supporting analysis. These "flags" are presented in Section C.1. It must be assumed that the reader is familiar with each of the three point designs since to incorporate the referenced material contained in the point designs would generate excess bulk in this report. The second solution to an analytical impasse was to assume the missing information based on standard engineering practice and current state-of-the-art materials, etc. This solution was exercised when the design feature was central to the design concept. The results of these point analyses are also contained in Section C.1. Section C.2 discusses the development of the instrument parameters for the reference instrument.

C.1 EOS POINT DESIGNS

C.1.1 Critique of Hughes Aircraft Co. SSR Point Design

C.1.1.1 General Comments

- Dominated by large scan mirror and sunshield which would make spacecraft mounting (not shown) difficult if not impossible to assemble.
- Orientation of scanner to spacecraft interface may cause radical design concept change.
- Radiative cooler door malfunction could cause catastrophic failure. (Is door absolutely required?)
- High Risk Areas: ..... Scan mirror fabrication - (by P-E).

  ..... Scan mirror long-time continuous operation to true time-linear scan.

  ..... Launch environment survival of scan mirror assembly and sunshield.

  ..... Confidence levels in using MSS techniques for the EOS SSR are questionable.

C.1.1.2 Structural Frame

A. Large thin-section magnesium castings would be difficult to cast and machine to the close tolerances required, especially in non-symmetrical configurations.

B. The use of magnesium castings in the presence of residual stresses and repeated impacts from the external scan mirror in combination with possible temperature gradients would cause dimensional instability and misalignment of optics would result.

C. Launch acoustic environment, especially in design of the large sunshield was not considered.

D. A math or simulation model is referred to but very little information is described, and no system vibration math model was described.

C.1.1.3 Telescope Frame

A. Aluminum and Invar are alternately mentioned. It is not clear which is used and where and how various sections are joined and/or stress-relieved to micro-creep stability levels.

B. Baffle treatments are not defined.

C. Central baffle seems to be supported by primary mirror in a cantilevered manner. This looks like a problem affecting figure of mirror if true.

C.1.1.4 Scan Mirror Assembly

A. Fabrication of the large flat scan mirror by Perkin-Elmer is an unknown factor. A stable 0.15λ rms wave front accuracy is required for a 30 microradian instrument which presents a challenge to any mirror fabricator.

B. Insertion of plugs for "kicking" and "snubbing" the oscillating mirror could strain dissimilar material (beryllium mirror). Attachments of plug and torquer armature and nylon bumpers are not shown and could be a problem.

C. Long-term effects of the silicone rubber damper and cold-flow nylon bumper surfaces are unknown problems that could occur in space and cause velocity changes beyond the scan monitor capability. There is no indication that this is not a problem.

D. Deflections of the MSS mirror vary in the text from 10×10^{-6} inches to 27×10^{-6} inches, and it is not clear whether bonding or bolting of the mirror to some frame is or is not more effective (pps 3-3, 4-6 and D-5).

E. Static flatness (0 g release) of mirror is 15×10^{-6} inches, not 6×10^{-6} as HAC calculates and natural frequency would drop below 3300 Hz. Total deformation including thermal and dynamic forces would be considerably in excess of required $2\text{-}5 \times 10^{-6}$ inches. An analysis was made at HRC using a fine mesh model mirror with sandwich finite elements, and a coarser model with thin plate finite elements having approximately equivalent stiffnesses. Thermal and dynamic deflections were not included because gradients and mirror forces were unknown. As indicated above, the fine

model peak 1G deflection was 15.3 micro-inches and the coarse model was 9.4 micro-inches with first natural frequency at 789 Hz — the surface modes and deflection maps are shown in Table C.1 and Figures C.1 and C.2. The adequacy of the HAC design is thus open to serious question because optical performance is directly dependent on the optical quality and reliability of the large scanning flat mirror.

Table C.1

ANALYSES OF HAC SSR POINT DESIGN SCAN MIRROR

	Fine Model Sandwich Element	Coarser Model Equiv. Plate	Hughes SSR 020 Results
Peak 1G Displacement, micro-inch	15.3	9.4	6
Middle 1G Displacement, micro-inch	9.9	3.4	1
1st Nat. Frequency, Hz*		789.0	3300.
2nd Nat. Frequency, Hz**	894.0	1293.0	9700.
(* mode symmetric about X2, asymmetric about X1)			
(** mode symmetric about X1, X2: "dish mode")			

C.1.1.5 Mirror Assemblies (generally limited detail is presented)

A. The primary and secondary mirrors are supported with tangential bars, but there is insufficient detail shown describing the accomplishment of such mounting. No other mirror mounting is shown or described, so an evaluation cannot be made.

B. The packaging concept of the optics for the scan position monitor is not clear but there seems to be a problem in folding these optics. A more detailed layout would clarify this.

C. The aft optics area should include an optical schematic including the IMC mechanism and fold mirror for better delineation. Insufficient detail is shown of all the optic and mechanism relations and how they all mount to the

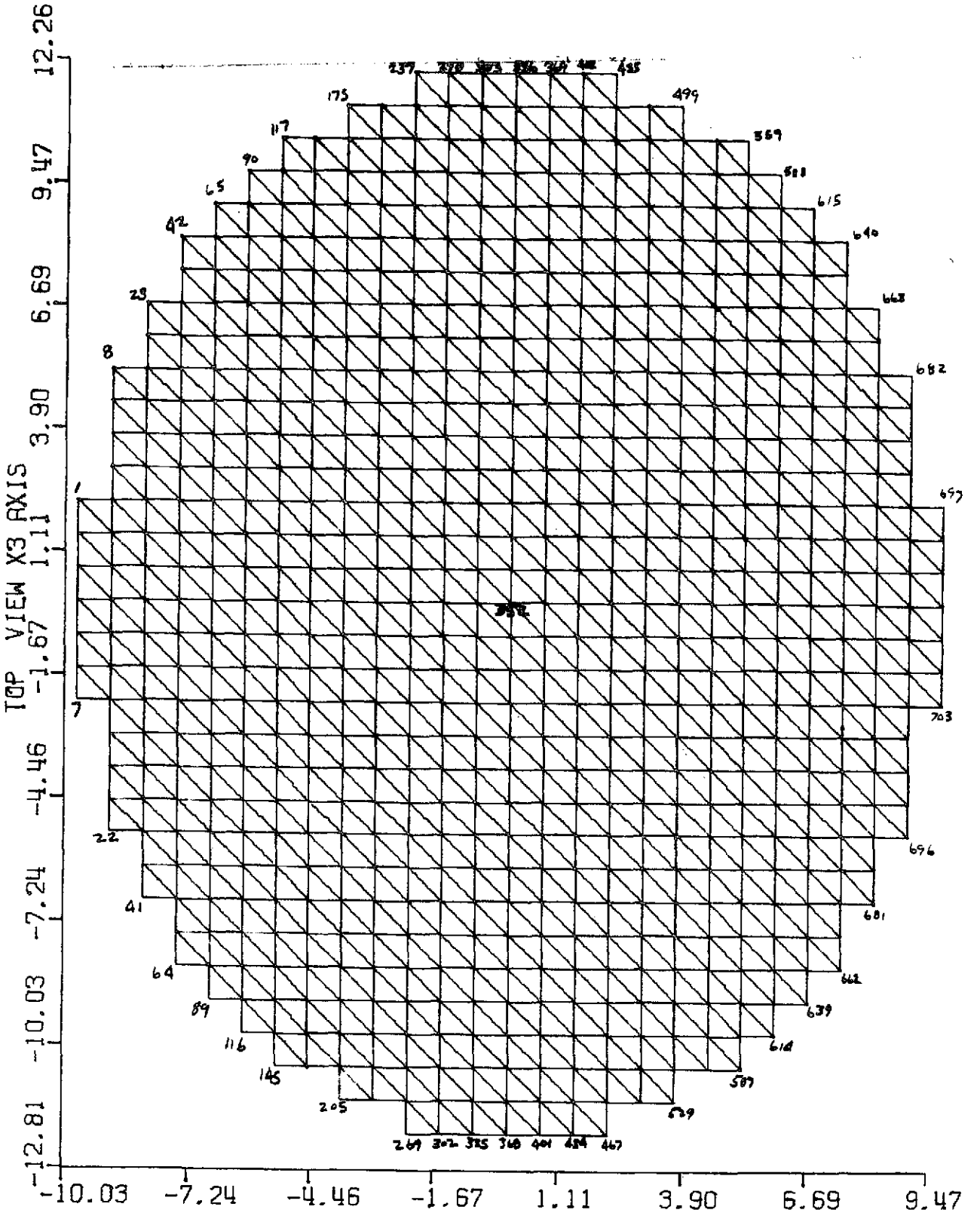

Figure C.1a FINE MESH MIRROR MODEL SURFACE NODES

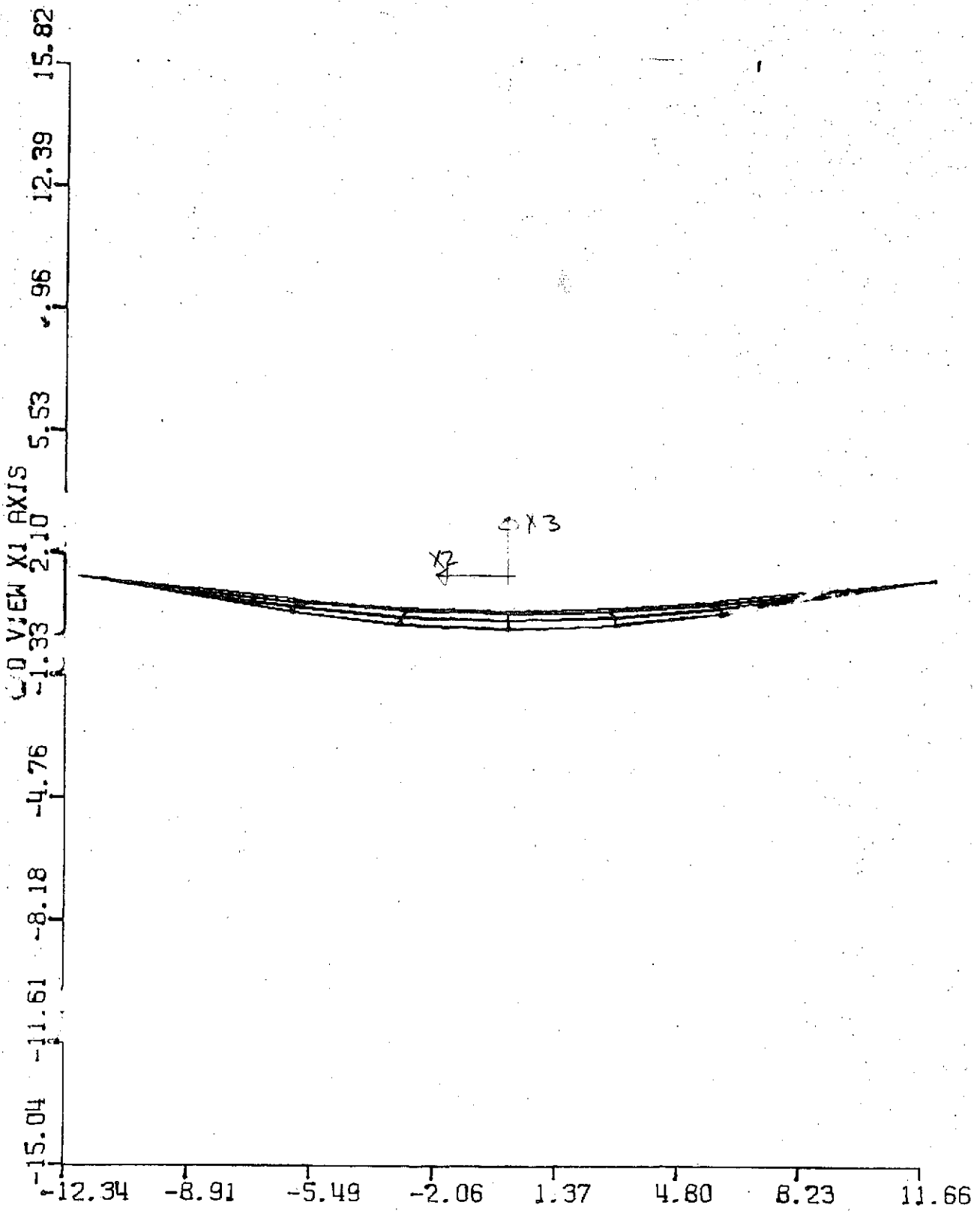

Figure C.1b FINE MESH MIRROR MODEL 1G(X3) DEFLECTION MAP

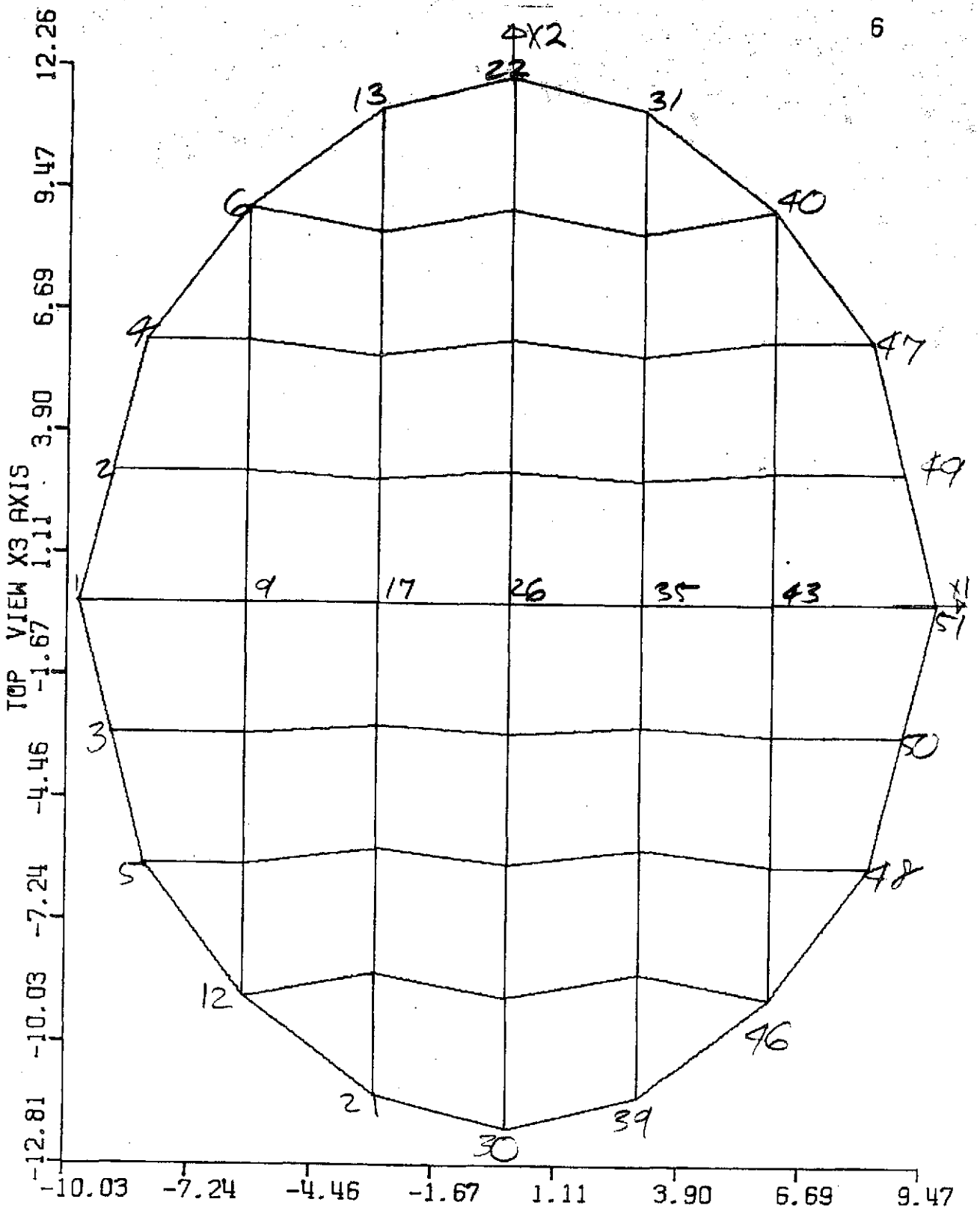

Figure C.2a COARSER MESH MIRROR MODEL SURFACE NODES

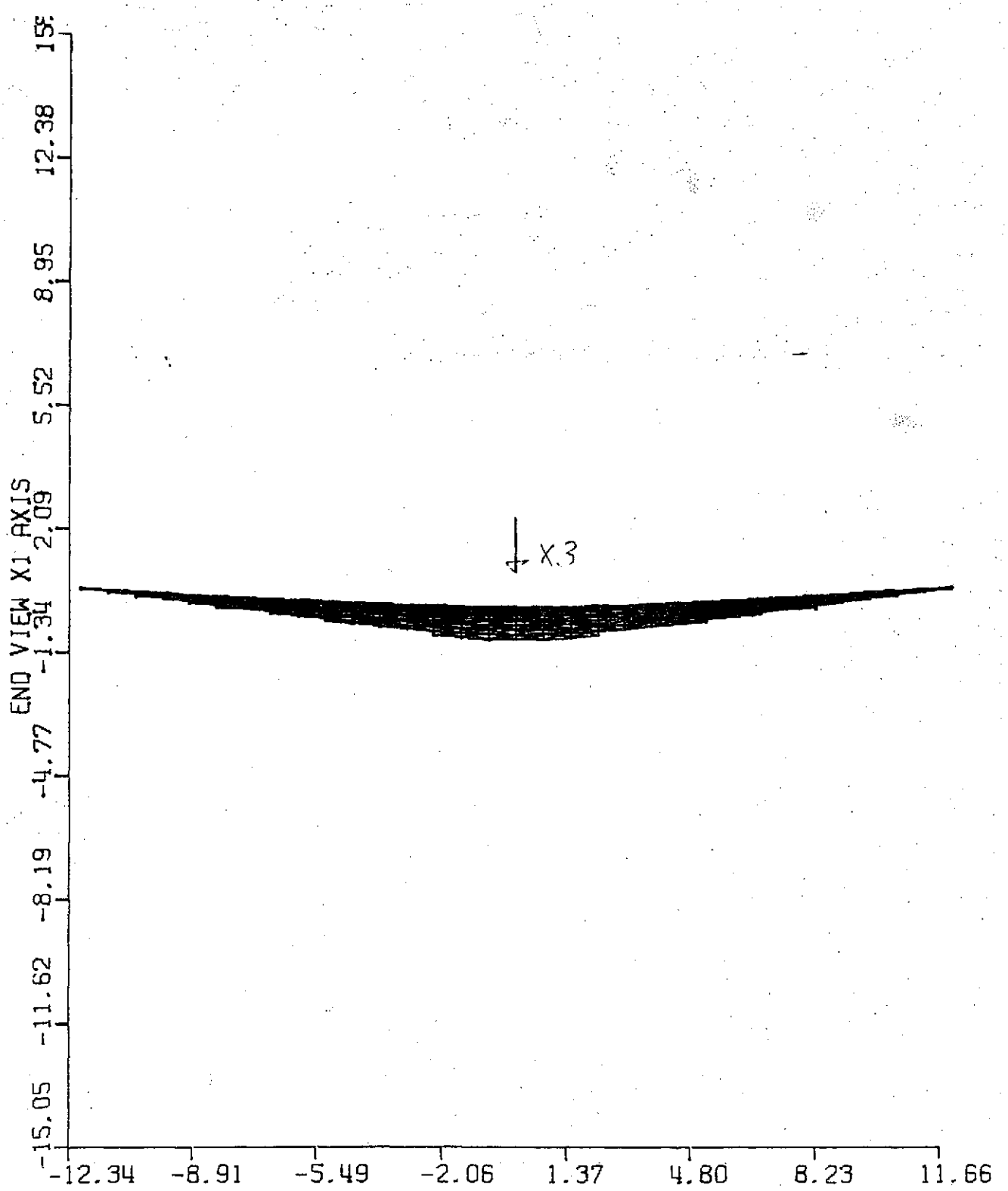

FIGURE C.2b FINE MESH MODEL 1G(X3) DEFLECTION MAP

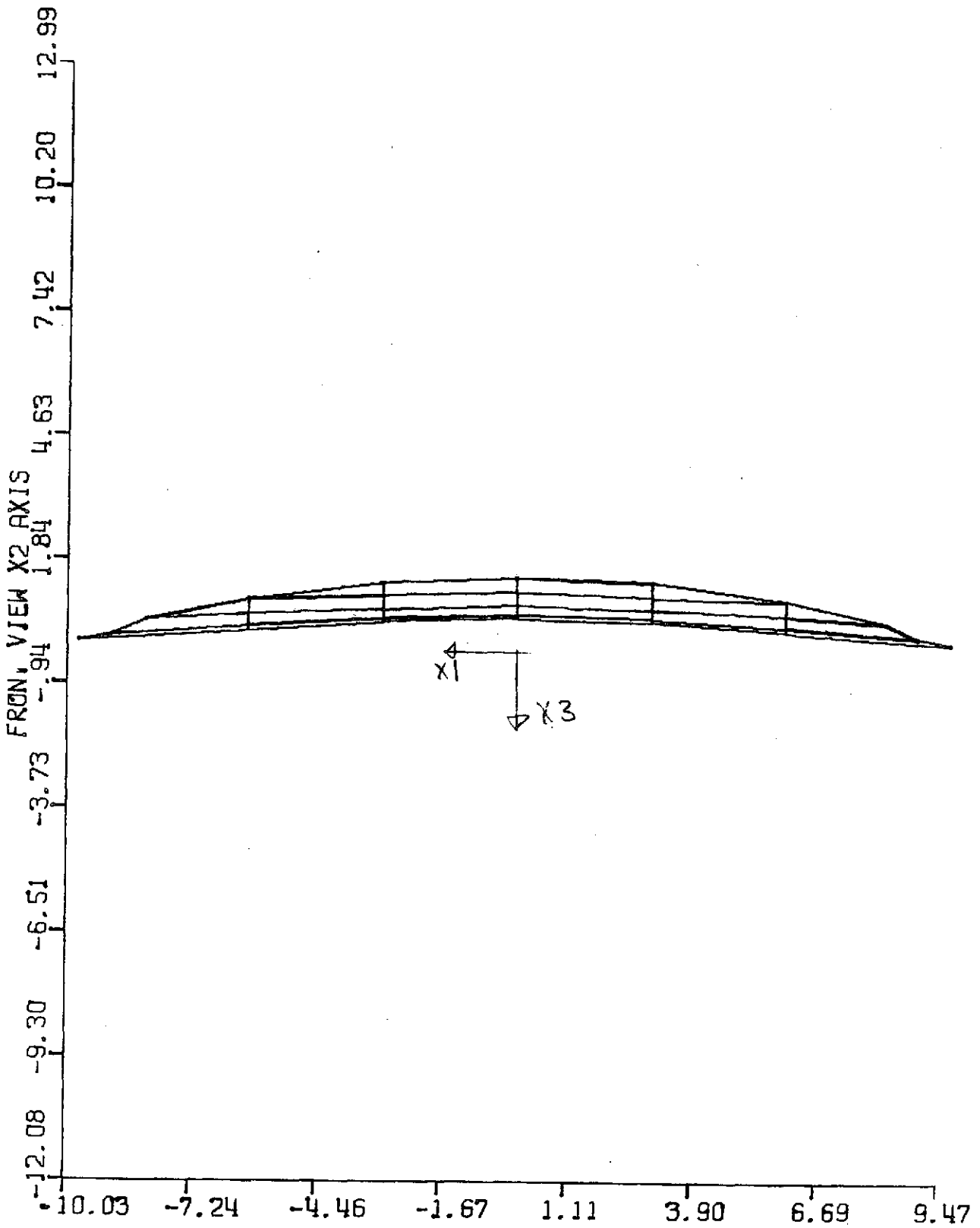

Figure C.2c COARSER MESH MODEL 1G(X3) DEFLECTION MAP

telescope. The confidence level is low for this entire design area because of the incomplete description.

C.1.1.6 Areas Not Sufficiently Described Or Questionable

A. The structural frame was thermally analyzed using aluminum although magnesium was the selection.

B. The finishes, treatments, or use of MLI and locations were not defined on the outside of the magnesium castings. If used, was its compatibility with the base material considered to maintain optical alignment?

C. Mounting of the IMC to the aft optics section is not shown and only obliquely referenced.

D. Interface of the SSR to the spacecraft and the thermal isolation to it was not discussed or design shown, nor was consideration given to adjacent obstructions affecting it.

E. The Aft Optics area from folding mirror to radiative cooler is not sufficiently detailed for comment. The proper integration of optics with passive radiative coolers is a difficult problem especially when there are several spectral bands requiring cooled detector arrays.

F. Lubrication has generally been designed out by using flexpivots instead of bearings wherever possible; but other lubrication points such as stepper motors, gears, sliding surfaces, etc have not been described or evaluated for long life usage.

C.1.2 Critique of TE Co. SSR Point Design

C.1.2.1 General Comments

- Relatively large and complex - heaviest design.
- Requires extremely close tolerances in fabrication and assembly.
- Requires an unusual number of shields and baffles.
- Mounting to spacecraft could be structurally unfavorable because of only two mounts. These are in-line and both at one end. It is not described how one of the mounts "floats" in one axis.

- High Risk Areas: ..... Scan wheel and roof mirrors
  ..... Scan wheel assembly
  ..... Launch environment survival
  ..... Overall complexity of parts and motions

C.1.2.2 Structural Frame

The TE Co structural frame consists of four aluminum castings that support the SSR instrument. The frame was modeled as a beam network with load inputs from components acting as rigid bodies. The resulting first fundamental vibration frequency was 158 Hz. It is questionable if large masses such as the scan wheel and the mirror can be sufficiently simplified to act as rigid beams loading a massive frame also modeled as a rigid beam. A program that analyzes the network as plates acting on plates would be more appropriate although more complicated. The probable result would be that the first fundamental vibration frequency would be lower than 158 Hz and thus could require modification of the frame design and the optical-mechanical configuration.

The description of the four castings and the pointing mirror support column did not indicate the method of their attachment, either by bolting, pinning, welding, brazing, or other method. Each method would have its own detail problems and it is doubtful if the math model included any of them. In addition, mirror mount flexibilities have not been included, and it is not clear if the primary mirror elements have included the effects of the flex-leaf supports.

C.1.2.3 Criteria For Design

It should be noted that the criteria for design was "survival of the launch environment requirements" and since the structure frame showed 60 g peaks at its 158 Hz resonance, this was taken as the most severe case. Maximum stresses were shown to be 25,000 psi. A part of the criteria for design should be to design for a micro-yield stress value with a well-defined safety factor so that creep and misalignment over a long-time period may be avoided for an orbiting instrument. The other criteria should be the maintaining of the alignment upon release of the 1 g environment. Although the 1 g release is shown using the math model, there was no discussion of designing to a micro-yield strength creep level.

C.1.2.4 Insulation Box (Outer Shell)

The description failed to include any acoustic analysis especially of the thin aluminum enclosure with its network of baffles and shields. This omission therefore raises the question of the validity of taking the structural frame as the most severe case of 60 g's from its sinusoidal vibration test. There was no input into the math model from this outer shell structure and there was no detail construction or calculations shown of the outer shell. If 60 g's were used to design the shell structure at 158 Hz, it may not be adequate to withstand broadband acoustic pressure of greater than 146 dB overall from 25 - 20,000 Hz. This is because the resonances of the enclosure may not be excited by acoustic pressures. A box structure, such as shown, having 0.030-inch aluminum skin with 0.017-inch aluminum baffles will have problems surviving >146 dB pressure. It is expected that stiffeners or panel design be changed to a semi-monocoque structure in order to survive >146 dB acoustic pressures.

C.1.2.5 Mirror Assemblies

C.1.2.5.1 Pointing Mirror

The pointing mirror will become disfigured because of the following:

A. The use of a hard trunnion mounting. No strain relief path exists.

B. The mounting is between preloaded bearings. Again, no strain relief path exists.

C. The pointing mirror could disfigure from a 0.0007 inch change in width between bearings under ±10°C excursions from the original assembly temperature.

D. The control rod articulating the mirror will produce strain because of its axial rigidity, especially if there is friction at the pivoted ball joint. The mirror surface is not separated from the stress region. The control rod is not required for fixed offset configuration, however.

E. Local strains may take place because of non-perfect mating of surfaces to the preloaded bearings. These bearings are not required for fixed offset configuration, however.

C.1.2.5.2 Primary Mirror

A. Assembly to "cup-like reservoirs" not clearly shown and mirror is not secured in Y and Z axes.

B. Questionable approach in attempting to achieve "soft compliance" up to 0.0001 inch (or 0.001 inch), and then a hard stop after 0.005-inch vibration displacement.

C. Safety factor of less than 10 at 750 psi is not sufficient as Cer-vit microyield strength is 1500 psi.

C.1.2.5.3 Scan Wheel Assembly

A. Fabrication and assembly of the roof mirror modules to 1 arc s accuracy in orthogonality would be difficult.

B. Fabrication of the wheel disc surface to a 1/4 quality optical flat (1/10 λ x 4) or 8-inch flatness would be difficult over the 32-inch diameter mounting surface.

C. Assembly of the scan drive requires 18 parallel surfaces between wheel and bearings, most of them contributing to possible cocking and variable compliances of the bearing raceways resulting in a wheel wobble considerably in excess of required 2 arc s. An individual raceway itself may have 15 arc s runout referenced to its face.

D. The critical areas of bearing preload, brinelling stresses of balls and raceways during launch and buckling of the bearing spacers will require more analysis than presented.

E. Bearing pair frictional torque of 6 inch-ounces may not be a realistic value when contributions from manufacturing tolerances are considered.

F. Discussion is missing on the method of achieving tilt control of the wheel axis about the Z axis - disregarding wheel wobble. Possible shims or spacers are not shown. Mounting of the wheel assembly to the frame casting is stated to be of some concern but the solution to minimize bearing strain effect is barely mentioned and the loading of critical parts to a microyield level has not been indicated.

G. The motor stator mounting appears to be inadequate to maintain a close air gap and concentricity with the rotor. The bearing housing and related sections are too thin and material is undefined.

H. The methods of maintaining positional accuracy after launch environment are not defined except through some close control of mating diameters. Pinning and epoxying seems to be avoided. This area requires more consideration.

I. Under vibration, a snubbing device limits excursion of the pointing mirror baffle near the roof mirrors. This is not shown, but its use should be avoided to minimize shock inputs to the mirrors.

C.1.2.5.4 Relay And Corrector Mirrors And Others

A. The relay and corrector mirrors would have the same problems as the primary mirror.

B. The assembly of the corrector mirror to provide two mounting pads along the launch acceleration axis (similar to the primary mount) is not shown. A strain cell of different design would be required.

C. Other mirror assemblies are not described and problems may exist in packaging, especially the image cone corrector and its mechanism.

C.1.2.6 Areas Not Described Sufficiently For Comment

A. Mechanisms: ..... Image cone compensator

..... Focus control mechanism

..... Pointing mirror stepping mechanism

B. Mounting of Items: ..... All mirrors from corrector mirror to detectors are not shown in their mounting configuration.

..... Pointing mirror column to the frame casting is not shown and not adequately described except as a torque box.

..... Radiative cooler to scanner support or mirror column is not clearly shown, nor inputed to math model.

C. Balancing of Wheel: ..... How this is to be implemented or controlled is not mentioned.

C.1.3 Critique of Honeywell SSR Point Design

C.1.3.1 General Comments

The HRC Point Design SSR is a mechanically simple well-proportioned structure and optical configuration. Of the three designs studied, it is the most easily adapted to a spacecraft mounting. Its optical bench, or torque-ring, is used to mount the most critical assembly, the scan wheel, along the center of gravity as well as to support the entire instrument. The torque-ring also provides mounting to the spacecraft as its stiffest section, acting along its center of gravity, and at three mounting points thus minimizing spacecraft deflection effects on the instrument.

C.1.3.2 Highest Risk Areas

— Scan wheel and scan mirrors: fabrication and mounting

— Semi-monocoque shell and torque-box dimensional stability

— Mirror support designs – especially the aspheric relay mirror

The configuration shows a heat pipe attached near the scan torque motor, however, there is no information on its method of attachments, nor necessary supports to survive the vibration environment on its path to the radiative base plate. It is also not indicated whether these necessary supports have been included in the overall conductance figure used.

C.1.3.3 Structural Design Requirements

The structural requirements to meet the acoustic, thermal, vibration and zero G release environments have been carefully considered and sufficient information is included to transmit a good degree of confidence in the design. However, as pointed out, some additional work is needed in the following areas:

1) Reinforcement of the cone section opening for incoming light. The details of the design used for the computer analysis was not shown, and the degree of necessary cut-out was not given.

2) The support of the primary mirror to its structural honeycomb plate. The analysis of the bezel design is not conclusive or at minimum is not clear, and the method of mounting the mirror in its bezel is omitted. Also the attachment of the hoop cylinder to the rings of the bezel is not indicated, nor is the attachment to the honeycomb plate. These areas need further design and analysis.

3) The mounting of most of the mirrors in general, requires further detail design and analysis including the optical elements of the spectrometer especially for the vibration environment.

4) The structural math model should include the influences of the baffle around the pointing and primary mirror. Details of the baffle construction and mounting to the semi-monocoque shell is also incompletely shown and described.

5) The mounting arrangement of the torque-ring and the three or four point mounting to the spacecraft was not analyzed for this report but the mounting was analyzed in an earlier weight-cost study that was subsequently changed. In any event, this area was not resolved and further work is needed to show the relationship between mounting to the spacecraft and internal component mounting to the torque-box ring.

C.1.3.4 Fabricability

The fabrication of the cone and cylindrical sections as well as the scan wheel assembly support cone will be difficult if not impossible to make as presently shown, and it can be expected that some changes in the metal thickness and section shapes will be necessary. However, even with recognizable changes fabrication may be difficult so as to avoid optical misalignments caused by gradual internal stress-relieving of rolled and machined thin sections, as well as those effects caused by temperature changes on the structure. Areas not sufficiently described or questionable are as follows:

1) Baffles

- material and finish or edge treatment is not indicated;
- location of baffles near shell opening is incorrectly shown;
- support of baffles to rings may not withstand vibration-acoustic environment. This has not been included in analysis and the proximity of baffles to primary mirror is undesirable;
- the assembly of the baffle or combination of baffles to the shell and/or pointing mirror is not clear and is not an optimum solution.

2) Aspheric Mirror

- the mounting of the aspheric mirror and its proximity to the torque-box (as well as its involvement with the necessary opening in the scan wheel housing) requires further packaging study. This is a weakly developed area.

3) Scan Wheel Assembly

This assembly is configured to balance the wheel, mirror, shaft and components so that theoretically there is no tilt of the shaft and mirrors in a 1 g or 0 g condition. There is some question, however, of support conditions, that is, bearing stiffness or isoelasticity. A study is recommended in the report to determine the sensitivity of the support conditions and its relation to actual tilt of the hardware. This appears to be an area of uncertainty that requires more investigation.

4) Bearings

A second area of design requiring further delineation would be the method of allowing the smaller set of bearings to float under thermal expansion along the shaft. It appears some floating freedom of the bearings is intended by using RTV between the bearings and housing bore, but this is not described and does not appear feasible. Some type of separate bearing diaphragm is required to allow axial softness but radial stiffness.

A lubrication reservoir was described for the bearings, but its detail is not shown in the assembly drawing, however, considerable analysis was included in a special section which could have led to appropriate design.

5) Scan Wheel

Fabrication of the beryllium wheel with its shrink-fitted titanium shaft, assembled with an inboard beryllium spin mirror and outboard spin mirror, appears to be within the state-of-the-art but would require the services of a specialty beryllium optical house. Since details of the mirror mounting surface to the wheel are not shown, these presumably were left to be worked out with the beryllium fabricator.

C.1.3.5 Anticipated Problems

1) Selection of two lapped surfaces to be used for reference and for mounting on the same side of the wheel.

2) Configuration of the beryllium spin mirror to allow mounting without damaging or influencing the mirror surfaces.

3) Maintaining position of the mirrors after vibration.

4) Dimensional integrity of the beryllium wheel under changed manufacturing, test and assembled loading conditions.

C.1.4 Radiative Cooler Design

The performance of the indium antimonide and mercury-cadmium-telluride detectors is very sensitive to the detector operating temperature. To determine the feasibility and practicality of reaching the desired operating temperatures using a radiative cooler, a subcontract was let to Arthur D. Little, Inc., Cambridge, Massachusetts to study the proposed radiative coolers and provide the desired information. Their report is included here as Appendix A. Although ADL and others have successfully designed, tested and flown several cooler designs the optical and mechanical integration of a passive two stage cooler is inherently a difficult task. This is because the inner stage must be well-shielded and thermally isolated in order to achieve its specified low temperature. In order to mount a 16-element array of detectors on this inner stage, it is necessary to bring signal radiation from the telescope (or a spectrometer) through the smallest possible hole in the MLI shielding

and then to focus it on the array. The inner stage is necessarily loosely coupled to the outer stage in order to give the required thermal isolation. This raises the possibility of a defocus and misalignment because of launch acceleration, shock or vibration. Techniques to minimize or correct such effects exist but the high resolution of the SSR type instruments makes this a difficult task.

C.2 THEMATIC MAPPER PARAMETERS

C.2.1 Instrument Definition

Three competitive approaches have been sponsored by NASA/GSFC, an image plane conical scanner by Honeywell (HRC), an ERTS-type object plane linear scanner by Hughes (HAC), and an image plane linear scanner by Te/Gulton (Te). Each of these instrument concepts has inherent beneficial features and inherent design risks. The three vendors have submitted Point Design Studies for the Thematic Mapper/SSR to the EOS Program Office, NASA/GSFC. We shall attempt here to provide an assessment of the risk factors associated with each point design.

C.2.2 Features

Table C.2 shows a comparison of the three approaches from a spacecraft integration point of view, i.e., size, weight, power. For this analysis, design study options were selected that most nearly met the 30 meter ground resolution (Bands 1-6) for a 100 nmi swath and a 494 nmi altitude. The requirement for offset pointing has been deleted in accordance with subsequent studies and the weights shown in Table C.2 have not been updated to consider this. It should be noted that the instruments are all large relative to the most recent 36 inch x 36 inch x 72 inch space constraints, however, repackaging to meet this new envelope is considered a minor risk. The HAC instrument is the lightest and the HRC instrument consumes the most electrical power.

C.2.3 Performance

Using the same 30 meter IFOV option and same instrument size, Table C.3 summarizes the performance. It should be noted that the three instruments provide comparable radiometric performance (SNR's, $NE\Delta T$'s) with the exception of bands 5 and 6. (Hg,Cd)Te detectors in the HRC band 5 clearly provide an advantage. The band 6 (2.08-2.35 μm) performance of all three designs is clearly below specification. However, the utility of band 6 is in question. The numbers in Table C.3 are those reported in the individual point design

Table C.2

SSR POINT DESIGN COMPARISON CHART

Company	Scan Type	Scan Efficiency	LxWxH (in.)	Weight (lb.)	Power (Watt)	*Major Axis Flight Direction
HRC	Conical (6 Arm)	80%	84x36 Dia	600	200	∥ or ⊥ to Flight Vector
HAC	Linear (Bi-directional)	80%	72x36x42	500	100	⊥ only
Te	Linear (Uni-directional)	80%	84x36x38	598	100	⊥ only

* Add 50 watts to each for heaters

Table C.3

SSR POINT DESIGN PERFORMANCE SUMMARY

Band (micrometers)	Nmin (W/cm^2-sr)	EIFOV and Detectors HRC	HAC	Te	Signal-To-Noise Ratio Specified	HRC	HAC	Te
1) 0.5-0.6	$22x10^{-5}$	33 μrad 16,Si	30 μrad 14,PMT	33 μrad 15,Si	10	11.5	17.4	14.5
2) 0.6-0.7	$19x10^{-5}$	33 μrad 16,Si	30 μrad 14,PMT	33 μrad 15,Si	7	12.5	13.5	14.5
3) 0.7-0.8	$16x10^{-5}$	33 μrad 16,Si	30 μrad 14,PMT	33 μrad 15,Si	5	13.8	9.6	13.2
4) 0.8-1.1	$30x10^{-5}$	33 μrad 16,Si	30 μrad 14,Si	33 μrad 15,Si	5	15.6	6.1	11.9
5) 1.55-1.75	$8x10^{-5}$	33 μrad 16,HCT	30 μrad 14,InSb	33 μrad 15,InSb	5	23.0	5.2	7.0
6) 2.08-2.35	$3x10^{-5}$	33 μrad 16,HCT	30 μrad 14,InSb	33 μrad 15,InSb	5	2.0	2.7	3.7
7) 10.4-12.6	300K BB	132 μrad 4,HCT	105 μrad 4,HCT	165 μrad 3,HCT	NEΔT 0.5K	NEΔT 0.3K	NEΔT 0.55K	NEΔT 0.3K

Notes:

1. 100 nmi swath, 494 nmi altitude, 30 meter resolution (bands 1-6).
2. 80% scan efficiency.
3. A_c = 950, 1321, 525 cm^2 (HRC, HAC, Te, respectively).

studies and some of these are subject to question. The Te design has a significantly smaller entrance pupil area than the others. An independent analysis provided signal-to-noise ratios for the Te design of approximately one-half those shown. Improvement in collecting and transmitting efficiencies of the magnitudes indicated are not substantiated in the report. The question then arises as to the viability of the size constraint with the possible increased aperture required for the Te design.

C.2.4 Principal Risks

The principal risk areas of the HRC concept are the scan wheel support structure stability and modification to the 72-inch length. The scan wheel support as shown is a rigid, double cone connected to the mounting ring. The questionable point of the design pertains to the degradation of telescope and scanner alignment as the mounting ring is stressed by mounting. Conformance to the 72-inch length dimension will require a complete revision of the spectrometer layout which has not been accomplished at the time of writing this report.

The HAC design requires an optically flat surface for the large scan mirror. Because the angular resolution requirements are approximately three times better than the ERTS-MSS (30 vs 86 μrad) and the scan mirror size approximately twice the diameter (48 vs 22 cm), the requirements for dynamic and thermal stability are more stringent. Independent analysis shows a lower natural frequency than that reported in the HAC point design report, and therefore, the dynamic stiffness is in question. The scan mirror in this design is exposed to the earth's thermal loading and thus a strong possibility exists for thermal gradients to develop. Supporting analysis was not provided in the report. Time did not permit an independent thermal analysis. A second area in question is the image motion compensator. The report does not cover in detail an error analysis of the image motion compensator, its reliability or its long-term stability. The final areas in question are the weight and power consumption which, although possible, may represent greater risk in attainment.

The Te concept, although sound, appears to be designed around optical efficiencies greater than demonstrated in the Point Design Study report. The risk, therefore, is in the physical size required to accomplish the stated task. The 2.5:1 entrance pupil area ratio (HAC to Te) does not seem reasonable. Design margin is not apparent in the performance calculations. As in the HAC design, the secondary correction mechanism (the cone compensator) was not

analyzed relative to an error budget, its reliability or the long-term stability. The electrical power requirements do not seem to allow any design growth or realizability margin.

The final risk area common to all three of the point designs is the radiative cooler which is described in Appendix A. While radiative coolers have flown on numerous satellites, the integration of the large cooler with the relatively large number of detectors still presents a challenge. It can be concluded from the comparison review that all three approaches have potential design problems which should be studied prior to selection of a final concept.

APPENDIX D

PUSHBROOM SCANNER VERSION OF THEMATIC MAPPER

D.1 INTRODUCTION

A pushbroom scanner version of a thematic mapper is described here because of the considerable interest shown in such an instrument. A brief survey of present large array technology was made to assess presently obtainable arrays and to determine if such a pushbroom version of a thematic mapper could be developed in time for the EOS program circa 1978 or for similar missions in subsequent years. The survey results and the conceptual design study show that a Pushbroom Thematic Mapper is feasible for 1978 or later delivery providing that certain development requirements are met. Six areas have been identified as needing further development. These are:

1) Photovoltaic (Hg,Cd)Te arrays of 6000 or more elements with good agreement (<20%) in detectivity (D^*_λ) and reasonably good agreement in responsivity across the array.

2) Integrated circuit preamplifier arrays with silicon JFET inputs for interfacing PV pushbroom arrays with CCD multiplexers.

3) CCD multiplexers for each pushbroom array.

4) A resonant type mechanical chopper for focal plane radiation chopping to provide dc restoration in each video channel.

5) In-flight long-term radiometric calibration techniques.

6) Providing a wide field high resolution optical design which covers a broad spectral region.

Each of these problem areas will be discussed in subsequent paragraphs. Tradeoff information is presented to establish the feasibility of the conceptual design and to allow for further comparisons and tradeoff decisions to be made in future mission planning.

D.1.1 Motivation and Guidelines of the Study

In configuring a pushbroom instrument, one important motivation is to improve on instrument reliability in unattended space missions

by the elimination of most rotating or sliding mechanical parts which are essential in the more conventional opto-mechanical multispectral scanners. This mechanical simplification is at the expense of electronic complexity and it should be emphasized that with present day detector and preamplifier technology some type of mechanical radiation chopper is still needed to allow the use of ac amplification with subsequent dc restoration of the video signal in each channel. Mechanical motions for long-term radiometric calibration are also likely requirements in most designs. There is a high probability that these chopping and calibration motions can be made in a very reliable manner using only flexure motions and small displacements. A second motivation for pushbroom versions of multispectral scanners is the simplification of the optics. In opto-mechanical multispectral scanners, the optics are quite complex, and some designs require servo motion of optical correction elements in order to achieve the required performance. Paragraph D.2.2.1 shows that this simplification of the optics is not readily achieved, but some reduction in the number of optical elements is perhaps possible. Perhaps the chief motivation of flying a pushbroom scanner is the fact that pushbroom systems have greatly improved signal-to-noise ratios as shown in paragraph D.2.2.2. An important guideline in comparing various multispectral scanner designs is worth noting here. Most users have expressed a need for a thermal spectral band in the 10.4 to 12.4 micrometer region. The inclusion of this band is thus important from the user's standpoint, but it also has a profound influence on the optical design of any multispectral scanner. The photons not only have a longer wavelength but also, therefore, have less energy per photon. This greatly restricts the choice of optical materials and detectors. Cooling is required for optimum performance in the thermal band. The in-band energy from earth self-emission is lower than that in the reflected sunlight bands unless the reflected sunlight bands are made very narrow.

The mid-band wavelength, λ_c = 11.4 microns, of the thermal band will determine the largest diffraction blur and thus will determine the aperture requirements of the instrument whenever the instantaneous field of view (IFOV) of the thermal band is made equal to that of the other spectral bands. Since a large number of users have expressed a preference for equal IFOV subtense in all bands, the requirements of the thermal channel can very well dominate in configuring any multispectral scanner, whether pushbroom or opto-mechanical.

D.2 SYSTEMS ANALYSIS

This section briefly discusses those aspects of systems analysis which are useful in comparing various versions of thematic mapper for an EOS type satellite.

D.2.1 Baseline Pushbroom System for ERIM Study

The baseline pushbroom system for the ERIM study is based on a modification of the Thematic Mapper Point Design Studies for the Scanning Spectroradiometer using an EOS type satellite. The major new change is the use of the latest ERIM worsr case spectral bands and radiance values. The bands have been narrowed and there are eleven bands instead of the previous seven. Table D.1 lists the baseline system parameters and Table D.2 presents the worst case ERIM spectral bands and radiance values. Also the new baseline system requires that all eleven bands have the same value of ground resolution (30 meters) while in the point design studies the thermal band was allowed to be several times (3 to 4 times) larger to ease the signal-to-noise and diffraction problems associated with the long-wave infrared band.

D.2.2 Derived Quantities and Some Implications

D.2.2.1 FOV and Optics

From Table D.1 the full optical field width is $\Phi = 14.74$ degrees and the half-field is $\Phi/2 = 7.37$ degrees. Therefore, we note immediately that it is a difficult optical design task to provide the required high resolution for 42 μrad IFOV across such a wide field. Opto-mechanical scanners have an advantage because they can scan a wide field with a telescope which is essentially operating on-axis or nearly on-axis. Examples are the Hughes object plane scanner and the Honeywell and Te image plane scanners. The Honeywell conical scanner scans an arc of an image at a preselected off-axis angle, but this circular arc is folded during scanning and brought on-axis and the telescope aberrations are corrected at the off-axis angle used. The non-scanning optics for a pushbroom multispectral scanner however, require a telescope whiich is corrected over the full field. Because of the inclusion of infrared bands, it is difficult to achieve this correction in the conventional manner using one or more refractive correctors. The most efficient design is an all reflective folded Schmidt with the folding mirror providing correction of a large spherical primary mirror. Subsequent correction in relay optics would then be required as stated in D.3.

Table D.1

BASELINE SYSTEM PARAMETERS

Ground Resolution	30 meters
Orbit	22 Dec. 0930 hrs, 30° Latitude (Florida)
Altitude	716 km to 900 km
Swath Width	185.2 km
Physical Envelope	36 in. dia x 72 in. long cylinder
Weight	400 lb max
Electrical Power Consumption	300 W peak
Cooling	Double Stage Passive Radiator at 200 °K and 100 °K

FOR 716 km SATELLITE ALTITUDE

IFOV,	42 μrad at 716 km
Suborbital Velocity, V	6740 m s^{-1}
Optical Total FOV,	14.74° for 185.2 km Swath width
Optics Speed	F/2.5
Aperture	24 inch (60.96 cm)

Table D.2

PERFORMANCE OF PUSHBROOM THEMATIC MAPPER USING ERIM RECOMMENDED SPECTRAL BANDS AND SPECTRAL RADIANCES

Band Number	λ_1 (μm)	λ_2 (μm)	$\Delta\lambda$ (μm)	Minimum L_λ ($W\ cm^{-2}\ sr^{-1}\ \mu m^{-1}$)	Minimum $N_{\Delta\lambda}$ ($W\ cm^{-2}\ sr^{-1}$)	IFOV 30 m at 716 km ω (rad)	Aperture for 24 in. dia A_c (cm^2)	Overall Optics Efficiency $\tau_o\ \alpha$	Detector Responsivity R_λ (AW^{-1})	Equivalent Noise Bandwidth Δfn (Hz)	Signal I_s (A) $x^8 10^{-11}$	S/N Ratio Or NEΔT Goal	S/N Ratio Or NEΔT Calculated
1	0.42	0.48	0.06	4.79×10^{-3}	2.87×10^{-4}	4.18×10^{-5}	2918.6	0.30	0.15	176.45	3.298	287	351
2	0.48	0.52	0.04	4.797×10^{-3}	1.919×10^{-4}	4.18×10^{-5}	2918.6	0.30	0.28	176.45	4.110	198	437
3	0.50	0.54	0.04	4187×10^{-3}	1.675×10^{-4}	4.18×10^{-5}	2918.6	0.30	0.30	176.45	3.845	170	409
4	0.52	0.58	0.06	3.683×10^{-3}	2.210×10^{-4}	4.18×10^{-5}	2918.6	0.30	0.32	176.45	5.409	146	576
5	0.58	0.64	0.06	2.589×10^{-3}	1.553×10^{-4}	4.18×10^{-5}	2918.6	0.30	0.36	176.45	4.277	100	455
6	0.62	0.68	0.06	2.224×10^{-3}	1.334×10^{-4}	4.18×10^{-5}	2918.6	0.30	0.39	176.45	3.980	88	425
7	0.69	0.74	0.05	1.609×10^{-3}	8.045×10^{-5}	4.18×10^{-5}	2918.6	0.30	0.41	176.45	2.523	67	269
8	0.8	1.1	0.3	1.102×10^{-3}	3.306×10^{-4}	4.18×10^{-5}	2918.6	0.30	0.22	176.45	5.564	33	592
9	1.55	1.75	0.2	1.428×10^{-3}	2.856×10^{-4}	4.18×10^{-5}	2918.6	0.25	0.62	176.45	11.29	130	1202
10	2.0	2.3	0.3	1.05×10^{-4}	3.15×10^{-5}	4.18×10^{-5}	2918.6	0.25	0.81	176.45	1.626	25	173
11	10.4	12.4	2.0	$\partial N/\partial T = 1.618 \times 10^{-5}$ for 250 °K BB	$W\ cm^{-2}\ sr^{-1}\ °K^{-1}$	4.18×10^{-5}	2918.6	0.20	$D^*_\lambda = 7.5 \times 10^9\ cm\ Hz^{1/2}\ W^{-1}$	176.45	-----	NEΔT = 0.25 °K	NEΔT = 0.50 °K (0.25 °K is achievable with 2-stage radiative cooler)

† Consensus 1 (Urban/Agricultural emphasis), Case 1; 22 Dec., 0930 Orbit, 30° Latitude (Florida), Worst Weather.

$$S/N = \frac{R_\lambda N_{\Delta\lambda} A_c \omega^2 \tau_o \alpha}{\sqrt{\Delta f_n \left\{ \left[V_A \left(\frac{2\pi \Delta fn}{1.111} \right) (C_i + C_f) \right]^2 + \frac{4kt}{R_f} + I_d^2 + I_A^2 \right\}}}$$

$$NE\Delta T = \frac{A_d^{1/2}\ \Delta f_n^{1/2}}{\left(\frac{\partial N}{\partial t}\right) \omega^2 A_c \tau_o \alpha D^*_\lambda} = \frac{4F\ \Delta f_n^{1/2}}{\pi \sqrt{2} \left(\frac{\partial N}{\partial T}\right) \omega D \tau_o \alpha D^*_\lambda}$$

where:

F = 2.5 optics speed

D = 24 in. = 60.96 cm aperture

where: $\frac{4kt}{R_f} = 1.656 \times 10^{-30}\ A\ Hz^{-1}$

$I_D^2 + I_A^2 \cong 1 \times 10^{-28}\ A\ Hz^{-1}$ for large arrays

$C_i + C_f = 1.02 \times 10^{-11}\ F$

$V_A = 2.2 \times 10^{-9}\ V\ Hz^{-1/2}$

The assumption is made that I_D^2 dominates and

$I_{Noise} = 1.3283 \times 10^{-13}\ A$

D.2.2.2 Electrical Bandwidth and Signal-to-Noise Ratio

From Table D.1 the suborbital track velocity is $V_{sot} = 6740\ ms^{-1}$ for a 716 km orbit altitude.

The line rate for 30 meter ground IFOV is

$$R = \frac{1}{\tau_d} = \frac{V_{sot}}{(IFOV)} \simeq \frac{6740}{30} = 225 \text{ line } S^{-1}$$

and the dwell time per line is

$$\tau_d = \frac{1}{225} = 4.45 \times 10^{-3} \text{ S}$$

The electrical bandwidth is

$$\Delta f = \frac{1}{2\tau_d} = \frac{224.66}{2} = 112.33 \text{ Hz}$$

and the equivalent noise bandwidth is

$$\Delta f_n = \frac{\pi}{2} \Delta f = \frac{\pi}{2} (112.33) = 176.45 \text{ Hz}$$

We thus note that the pushbroom version of a thematic mapper has a significant advantage over opto-mechanical scanners since the dwell time per IFOV is increased by a factor η_d/k over the dwell time in an opto-mechanical scanner where η_d is the number of IFOV or detectors in the horizontal pushbroom array which occupy one scan line and k is the number of detectors in vertical array needed to achieve satisfactory performance in the opto-mechanical scanner.

The total FOV is $\varphi = 14.74° = 2.572 \times 10^{-1}$ rad

The IFOV is $\omega = 42 \times 10^{-6}$ rad

so

$$n_d = \frac{\varphi}{\omega} = \frac{2.572 \times 10^{-1}}{4.2 \times 10^{-5}} = 6150 \text{ IFOV/line or Detectors/array}$$

In the Thematic Mapper Point Design Studies there were 16-element vertical arrays, so k = 16 and the Pushbroom Thematic Mapper (PTM) has an increased dwell time of

$$(\tau_d)_{PTM} = \frac{n_d}{k} (\tau_d)_{TM/SSR} = \frac{6150}{16} = 384.3 (\tau_d)_{TM/SSR}$$

C-2

and since bandwidth is the inverse of dwell time, i.e., $f = 1/2\tau_d$ the bandwidth of a pushbroom instrument is only approximately 1/384 that of an opto-mechanical scanner having comparable parameters.

The signal to noise ratio (SNR) will be improved by the square root of this factor, or $(SNR)_{PTM} = \sqrt{384.3}\,(SNR)_{TM/SSR}$ or

$$\frac{(SNR)_{PTM}}{(SNR)_{TM/SSR}} = 19.6$$

This improvement in signal to noise ratio is perhaps the main advantage of a pushbroom system in comparison to opto-mechanical scanners. It should be noted that the opto-mechanical scanners can increase the dwell time per IFOV and reduce their scanning rate by using more elements in vertical array. In so doing they are becoming a quasi-pushbroom design and thus begin to partake of the advantages and disadvantages of a pushbroom design. For example, the optics must provide high resolution over a wider field to cover the larger number of detectors, more signal channels are involved, etc.

D.2.2.3 MTF

The information bandwidth is low enough that signal-to-noise ratio performance will be satisfactory in all bands because the aperture must be large to minimize the diffraction effects on resolution in the thermal band. The criterion for resolution is to have 50% MTF at a 30 meter ground IFOV. This condition is called the EIFOV, the effective instantaneous field of view. Other criteria may, of course be applied. The Rayleigh criterion is

$$\alpha = \frac{2.44\ \lambda}{D}$$

where we choose $\lambda = 12.4 \times 10^{-6}$ meter, our longest wavelength. D is the aperture diameter in meters and α is in radians. Substituting D = 24 inch = 60.96 cm = 0.61 m gives

$$\alpha = \frac{2.44}{D} = \frac{(2.44)(1.24 \times 10^{-5})}{6.1 \times 10^{-1}} = 4.97 \times 10^{-5} \text{ rad} \cong 50\ \mu\text{rad}$$

The geometric angular subtense of a 30 meter ground footprint viewed from 716 km altitude is

$$\omega = \frac{30}{7.16 \times 10^{5}} = 41.8\ \mu\text{rad} \approx 42\ \mu\text{rad}$$

The achievement of the desired 50% MTF for 30 meter ground resolution (42 μrad subtense) in an actual design depends on the transfer functions of the detector and electronics as well as the OTF. The OTF itself is a function of the optical design especially when Cassegrain type telescopes with central obscurations are used or when non-standard aperture shapes are used as in the Honeywell or Te Co Thematic Mapper Point Designs. An MTF of 0.707 is generally assumed for the electronics and when the detector is sized to the IFOV an MTF of 0.64 is assigned to its aperture effect. These two MTF's multiplied together give 0.45 which must be multiplied by the OTF to give the overall system MTF. Since 0.45 is already less than the desired MTF of 0.50, it is necessary to increase the electrical MTF by a boost network and to increase the detector aperture MTF by narrowing the detector width in the scan direction. These two techniques will provide the desired MTF at the expense of a loss in signal to noise ratio. The detector is a rectangular aperture which has a portion of the image scanned across it. We are interested in the MTF of this convolution operation (sinusoid convolved with a rectangular aperture). The Fourier transform of a rectangular aperture is the detector aperture MTF.

$$(MTF)_d = G(f) = A \frac{\text{Sin } \pi \text{ WoF}}{\pi \text{ Wof}} = A \frac{\text{Sin } X}{X}$$

Where X is measured in radians and A can be normalized to unity. At $X = \pi/2$ we have $G(f) = 0.64$ which is the $(MTF)_d$ for the case when the detector aperture (detector size) just equals the geometric IFOV. Since the Pushbroom Thematic Mapper has adequate signal to noise ratio in all bands and inadequate MTF in the thermal band, it is worthwhile to trade signal to noise ratio for an increase in MTF by using an undersized detector width in the direction of scanning. If we use a mask and cut the width in half the detector MTF becomes the value of sin X/X at $\pi/4$ radians or $(MTF)_d = 0.90$. Since noise is proportional to A_d and signal is proportional to A_d the new signal to noise ratio which will occur when the detector width, w, is cut in half if found from the following relations:

$$\text{OLD: } \left(\frac{S}{N}\right) = \frac{kA_d}{A_d^{1/2}} = kA_d^{1/2} = k\sqrt{wh}$$

$$\text{NEW: } \left(\frac{S}{N}\right)' = k\sqrt{\frac{w}{2}}\,h = \frac{1}{\sqrt{2}}\left(\frac{S}{N}\right) = 0.707\left(\frac{S}{N}\right)$$

Therefore, the signal to noise ratio only degrades by a factor of $1/\sqrt{2}$ while the (MTF) increases from 0.64 to 0.90 which is a factor

of 1.41. The electronic system transfer function, $(MTF)_e$ is dependent on the choice of electrical filter and the resulting equivalent noise bandwidth, Δf_n. With a moderate amount of boost, the 2-pole Butterworth $(MTF)_e$ value of 0.707 can be increased to $(MTF)_e$ = 0.81 while the equivalent noise bandwidth changes from

$$\Delta f_n = 1.111\ \Delta f$$

to approximately

$$\Delta f_n' \cong 1.57\ \Delta f$$

so that signal to noise ratio degrades by the square root of this ratio:

$$\frac{1.111}{1.57} = 0.707 = 0.84$$

The Pushbroom Thematic Mapper overall MTF is thus $(MTF)_{sys}$ = (OTF) $(MTF)_e$ $(MTF)_d$ = (0.67)(0.81(0.90) = 0.49 which is very close to the desired MTF of 0.50 for the 30 meter ground subtense at 716 km altitude. Small increases in MTF can be still made by adding more elemctronics boost or by narrowing the detector mask. The SNR was degraded by a factor (0.707)(0.84) = 0.59 to achieve $(MTF)_{sys}$ = 0.49.

The value for the OTF of 0.67 assumes that the all-reflective Schmidt telescope is essentially a perfect diffraction limited system (OTF = 0.72) that is degraded by residual uncorrected aberrations (such as astigmatism) to the value 0.67. The spatial cutoff frequency at the focal plane for the thermal band (λ_c = 11.4 μm) is

$$v_o = \frac{1}{\lambda F} = \frac{1}{(11.4 \times 10^{-3})(2.5)} = 35.1\ \text{lp/mm}$$

The normalized spatial frequency is thus

$$\frac{v}{v_o} = \frac{7.8}{35.1} = 0.22$$

and OTF for a circular aperture is thus seen from tables or graphs to be approximately 0.72. A rectangular aperture has a somewhat higher OTF (OTF ≈ 0.80 in the scan direction) and an annular aperture is somewhat less depending on the obscuration ratio. An OTF of 0.67 is, therefore, not unreasonable for the thermal band using reflective optics. The MTF estimates made here only illustrate relationships. It is assumed in a detailed design that signal to noise ratio will be traded for MTF until desired values are achieved.

D.2.2.4 Detector Size and Chopping Amplitude

The detector size, s, is usually matched to the geometric IFOV,

$$s = f\omega = FD\omega$$

where f = focal length

F = optics speed = 2.5

D = aperture = 24 inch

ω = IFOV = 4.2×10^{-5} rad

substituting

$$S = (2.5)(24)(2.54)(4.2\times10^{-5}) = 6.4008\times10^{-3} \text{ cm} = 2.52 \text{ mil}$$

For the Pushbroom Thematic Mapper, we note that in the scan direction the thermal band detector is masked to one-half this width for purposes of improving MTF. The effective width is thus $\frac{2.52}{2}$ = 1.26 mil. Since all other bands have more than adequate signal-to-noise ratio, it is beneficial to mask all of the detectors in the other 10 bands to half width in the scan direction. A mechanical oscillating chopper can then be used to chop all bands equally with a minimum requirement for chopping amplitude. An oscillating chopper near the final focal plane need only move about 2 mils pk-pk in an oscillating motion which is parallel to the scan direction. The detectors are larger than the IFOV in this direction, so they may be located to the rear of the focal plane with no loss of MTF or no significant loss of signal-to-noise ratio.

D.3 OPTICS

As previously noted, the optics must be corrected out to 7.37 degrees half-field. A high OTF is essential if the thermal band is to achieve 50% MTF at 42 microradians IFOV. The use of refractive corrector elements is greatly restricted by the wide spectral coverage of 0.42 to 12.4 micrometers wavelength. These requirements suggest the use of an all-reflective Schmidt telescope using two main elements. An all-mirror telescope with only two mirrors is a great simplification over opto-mechanical scanners which use many mirrors. The primary is a large sphere with a 24-inch clear aperture. In order to achieve the wide field, the folding mirror

is placed at the center of curvature and the primary is oversize. The system is thus concentric and is a true Schmidt telescope. The spheric aberration of the primary is corrected by applying an aspheric correction surface to the folding mirror which also forms a stop for the system. Since the Schmidt telescope is a concentric system, the focal surface is also on a concentric spherical surface located midway between the primary mirror and the folding mirror. Because the full 14.74 degree field must only extend in the transverse (across-track or ACT) direction, it is not necessary that the correcting surface be rotationally symmetric nor is it necessary that the primary mirror be oversize in two dimensions. In order to save weight, it is possible to restrict its size to the 24 inch effective aperture. The system studied is shown in Figure D.1. The overall system operates at F/2.5 in order to simplify the relay optical design near the detector arrays and to allow use of practical detector sizes. The main Schmidt telescope must be faster than this because at F/2.5 a 24-inch aperture would have a 60-inch focal length and the spacing between the folding mirror and the primary would be 120 inches. If the telescope is operated at F/1.0, its focal length is 24 inches and its spacing between primary and folding mirror (primary radius of curvature) is 48 inches. It is then necessary to apply some optical power in the vicinity of the focal plane. A passive radiative cooler is required for the 100°K thermal band operating temperature and for Bands 9 and 10 (1.55-1.75 μm and 2.0 to 2.3 μm) a 200°K temperature is sufficient. This requires the use of a two-stage cooler. It is recommended that these bands be split off using a dichroic mirror or an aperture sharing folding mirror and relayed to the two-stage cooler because it is not practical to include the cooler in the curved Schmidt focal surface midway between the two telescope mirrors. Bands 1 through 8 could be located in the primary focal plane, but further correction is probably necessary. This could be accomplished by relay optics with appropriate refractive elements which also provide power to go from F/1.0 to F/2.5. Spectral band definition can be best achieved by individual optical bandpass filters over each array. The filters are placed in the F/2.5 beam rather than elsewhere because the filters can thereby be narrow in size and there will also be a minimum cone-angle (F/no.) widening of their bandpass.

The curvature of the field is not a serious design obstacle even though it is necessary to use a radiation chopper. It is recommended that a focal plane mask define each IFOV in the ALT (flight) direction. The detectors can be larger than this mask because there is adequate signal-to-noise ratio in all bands. It is

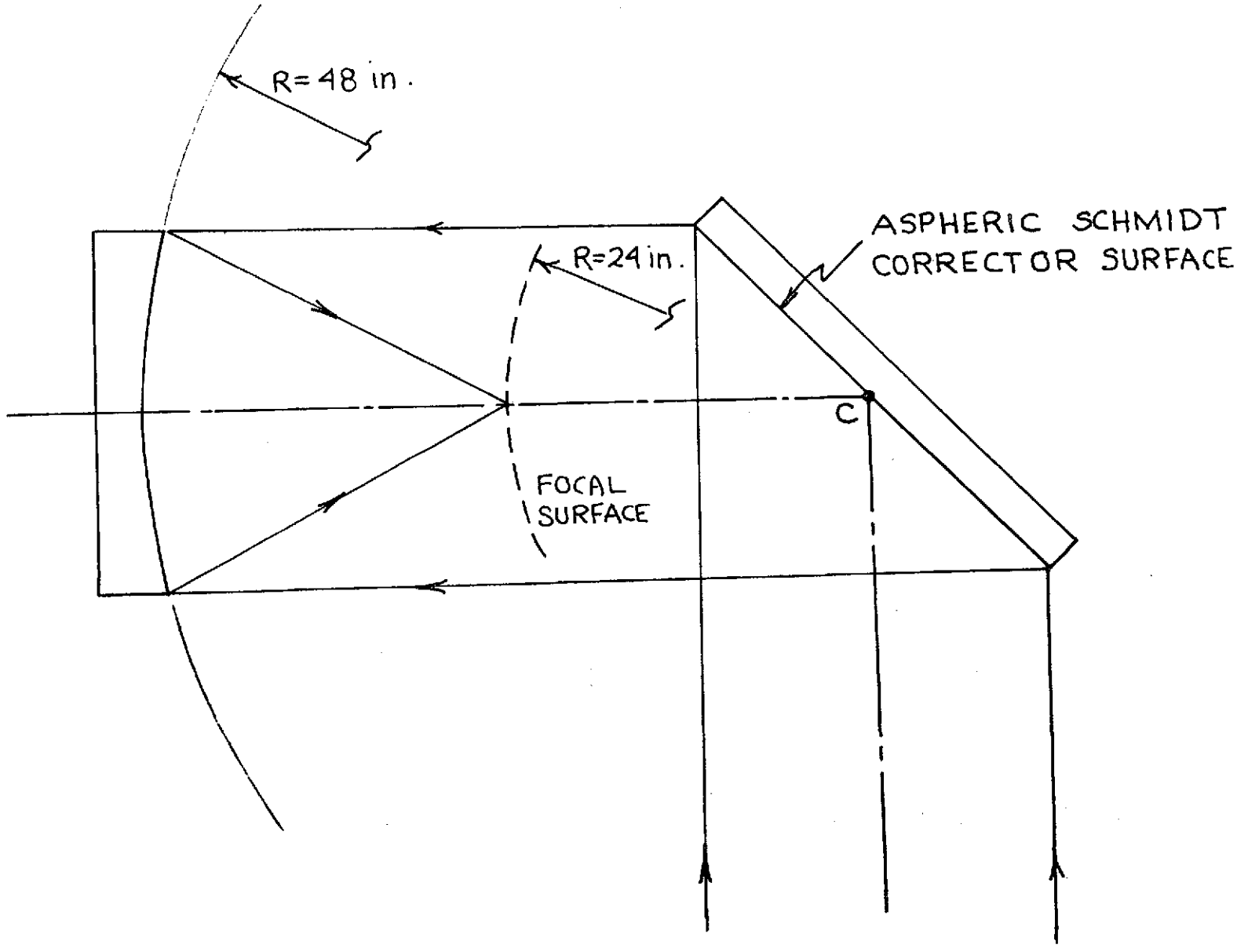

Figure D.1 REFLECTIVE SCHMIDT TELESCOPE

recommended that the detectors be made in linear array, but a staggered array may be required because of lead attachment requirements. With either linear or staggered arrays, the ALT dimension of each field mask opening would be made to be one-half of an IFOV so that the mechanically oscillating radiation chopper would move only about 2 mils peak-to-peak in order to chop the array mask. The focal plane arrangement shown in Figure D.2 is a candidate scheme. A further benefit of halving the ALT dimension is that the thermal channel OTF is thereby increased as stated in D.2.2.3. OTF improvements in the other ten spectral bands are not required, but the minimization of chopping amplitude increases reliability of the chopper and reduces the required electrical power to feed the losses in the mechanically resonant chopper structure.

It should be noted that with present detector array fabrication technology, it is not economic to produce all 6150 elements in a given array on a single monolithic substrate. It is better to provide modular groups of 100, 150 or 200 elements which are assembled to form the array. In assembly, it is possible to use a curved baseplate so that the array more or less follows the small curvature of the curved focal plane mask. The focal surface for a 24-inch F/1 Schmidt telescope is a sphere of 24-inch radius and a 14.74 degree field (7.37 degrees) occupies almost 6.2 inches in the ACT (transverse) direction. The sag at the center of the field is approximately

$$S = 24 - 24\cos 7.37^\circ = 0.2 \text{ inch.}$$

The use of a dichroic beamsplitter to separate the infrared from the remaining visible and near infrared bands allows a choice of reflecting or transmitting the infrared. The more efficient design is usually to reflect the shorter wavelengths and transmit the longer, but in this instance the layout is facilitated if the longer infrared wavelengths are reflected and relayed to a final focal surface on the inner stage of the two-stage radiative cooler. Any aberrations (such as chromatic aberration) which are introduced by the transmission part of the beamsplitter must be removed by subsequent optical elements. After the three infrared bands are split off, it is recommended that the need for physical splitting into three beams be eliminated by simply placing the three arrays side by side so that each array sees a given ground strip at a different time. Buffer storage during downstream data processing can then allow proper registering of all bands. In a similar manner, the other eight visible/near infrared bands could be placed side by side, but the designer also has the option of

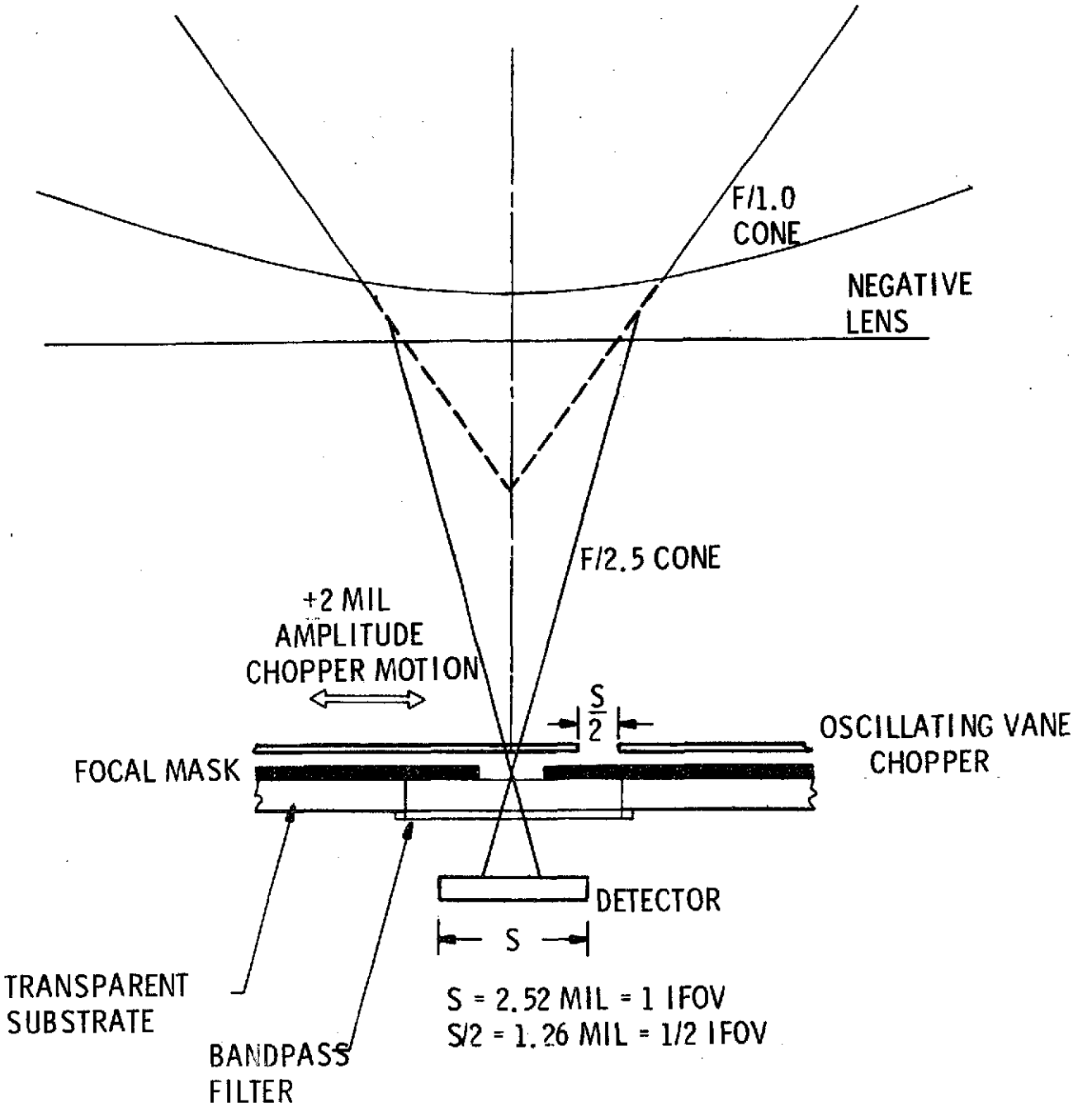

Figure D.2 CHOPPER AND FOCAL MASK

folding out portions of the beam to assist in spectral separation. This is possible because of the excess signal-to-noise ratio resulting from the large aperture. The large aperture, therefore, provides good MTF for the thermal band when its IFOV is made equal to the other ten bands and also provides good NEΔT performance even when the detectors are only cooled to 105°K and finally it allows the instrument and optical designers much more design freedom.

D.4 CHOICE OF DETECTORS

For the spectral bands between 0.42 μm and 1.1 μm (Bands 1-8), the best detectors are uncooled photovoltaic silicon diodes (PVSi). Silicon diode detector technology is the most advanced of all the detector technologies and arrays can be purchased from several vendors. Honeywell has found that the best single-element detector performance is found in the PIN-020A photodiodes made by United Detector Technology (UDT) of Santa Monica, California. Independent evaluations have been made by HRC which confirm the low noise current values quoted by the manufacturer's specification sheet. At the present time, no arrays from UDT have been evaluated, but arrays on 2 mil centers can be purchased from them. A planar diffusion process in a monolithic silicon slice is used to form array modules in groups of 50 or 100 so that it is expected by UDT that the low leakage current performance would be preserved in forming such an array module. The responsivity, R_λ, would vary as much as 200% from element to element or module to module, but this variation can be balanced out in the preamplifier array that is used to match the PV Si array to a CCD multiplexer.

The input to the preamplifier is a silicon JFET with low noise current. The best low noise single-element JFET types are made by TI, Ltd of England. The geometry of these devices and their method of production is compatible with monolithic silicon microcircuit fabrication techniques because they were first fabricated as process monitor devices in silicon microcircuits (LSI chips). Therefore, it will be feasible to obtain an array of such JFET devices. The variation from element to element is uncertain at this time but is expected to be acceptable. If an array of preamplifiers for the PV Si detector array is to be made in microcircuit form, there is need for development on making the preamplifier for a single channel in microcircuit form. A discrete component form of this preamplifier has been designed and evaluated by Honeywell, but no work has been done on forming microcircuit arrays of such JFET low noise high-impedance preamplifiers. Development work is also needed on interconnection techniques. Honeywell

has had favorable experience with a flip chip microcircuit interconnection method using raised pads and low-melting solder. This technique should be considered as a major candidate for connecting the detector arrays to the preamp arrays and for connecting each preamp array to its CCD multiplexer. The development of the CCD multiplexer is discussed in D.5 and in Appendix B.

The choice of detectors for the 1.55 to 1.75 μm band and for the 2.0 to 2.3 μm band is not as clear cut as in the shorter wavelength bands. Three types of detector could be used. The three applicable types are all photovoltaic diodes, either PV InSb, PV InAs, or PV (Hg,Cd)Te. Of the three types of material, PC InSb is the furthest in development. Arrays of PV InSb should be available with excellent uniformity. Ion bombardment doping can provide uniformity of about 15% in detectivity and leakage current across the arrays. There is a spectral fall-off of responsivity in the 1.55 to 1.75 μm band, but performance is still adequate even at 200°K operating temperature. The use of PC InAs should also be considered for these two bands because this material forms uniform arrays of high performance and detectivity is good in these spectral bands at 200°K operating temperature.

Similar comments apply to PV (Hg,Cd)Te arrays. This material is not as advanced in development, but by 1978 large arrays of PV (Hg,Cd)Te detectors will be available. For the thermal band between 10.4 and 12.4 μm, the best detector choice is PV (Hg,Cd)Te. Optimum operating temperature is approximately 100°K which requires a two-stage cooler with the outer stage operating near 200°K and the inner stage operating between 100 and 105°K. The design of the optical coupling between the telescope and detector arrays on the cold plate and the integration of a wide field multispectral optical system with a two-stage radiative cooler is a difficult task because for efficient cooler operation, only a small penetration is allowed in the multilayer insulation enclosing the inner radiator. This inner stage is thermally isolated from the outer stage and, therefore, is mechanically loose and very likely to shift during launch. This problem is aggravated in a 42 μrad system.

The dominant noise in the detectors for the first ten spectral bands is expected to be current noise from leakage at the detector or its preamplifier JFET so that the first equation in Table D.2 was used to estimate performance. For the thermal band the dominant noise is generation-recombination noise (GR noise); and, therefore, the second equation of Table D.2 was used. In Table D.2, the results are based on estimates of detector performance

expected from arrays. Selected single-element performance values are better than those used. For example, in Band 11, the thermal band, a D^*_λ of 7.5×10^9 cm Hz W^{-1} was used, but values in the 1×10^{10} region can be obtained in single elements. It is expected that arrays of PV_9(Hg,Cd)Te which will uniformly meet the D^*_λ value of 7.5×10^9 at 105°K operating temperature will be readily available by 1978. Some further development is required in order to make the performance routinely achievable. No theoretical problems or limitations are foreseen at this time.

D.5 CCD MULTIPLEXERS

Charge-coupled device (CCD) multiplexers are recommended as a candidate means of addressing the individual cells in the 6150 element pushbroom arrays so that telemetry channels or tape recorders can be efficiently used. Present Honeywell work and investigation is discussed in Appendix B. Hughes has also successfully matched CCD arrays to (Hg,Cd)Te cells. Present work at both Hughes and Honeywell is with only a few cells, but extensions to larger numbers of cells will occur as the development proceeds. Other laboratories are energetically investigating CCD and CID technology for computer and data processing applications, but the results will assist in developing the multiplexers for the pushbroom arrays. Direct development work is still needed for the devices themselves. By 1978 such multiplexers can be available providing that development continues at the present rate or is increased. Honeywell progress is encouraging in that multielement CCD modules with 99.9% charge transfer efficiency and S/N of 280 can be operated at 500 kHz.

RADIATION CHOPPER

Providing correction of short-term drifts in a dc coupled detector-preamplifier channel is a difficult problem in a pushbroom system with 11 bands and 6150 detectors per array. If dc restoration is not provided, certain users will object to the quality of the data and the resulting pictures. The most effective way to provide dc restoration is to use a radiation chopper with ac coupled electronics and clamping to a reference level. This is the conventional way to stabilize short-term drifts in infrared radiometers. In opto-mechanical scanners, it is possible to calibrate and clamp once every scan line during the dead-time of the scan cycle. In a non-scanning pushbroom system, this is not possible. The wide focal plane filed of the Pushbroom Thematic Mapper does not lend itself to including a rotating chopper wheel and such a rotating part violates the motivation for a pushbroom system. Because the

individual arrays for each spectral band are long and thin with each cell being only 1.26 mil wide in the flight (ALT) direction, an oscillating mechanically resonant focal plane chopper becomes an attractive solution. Motion required can be only a few thousandths of an inch as depicted in Figure D.2. Because the motion is of small amplitude, the device can be made very reliable. Pivots are flexural and bending is kept below the microyield point. The oscillating vane is maintained under tension at all times and the system is driven at its self-resonant frequency by magnetostrictive drivers. These drivers need only supply modest power because only the losses are supplied.

If the arrays are found to be quite stable with little short-term dc drift an occasional calibration and clamping on a command cycle should be considered. The command would be derived from time-countdown circuits and the vane chopper would be operated for one cycle. It would be spring loaded on one side only for automatic fail safe return.

In either manner of short-term calibration, the rear surface of the chopper vane would provide a reference level for clamping purposes. Because of the needs of the thermal channel, this surface should be black at the 11.4 μm wavelength region and the temperature should be reasonably constant.

D.7 LONG-TERM IN-FLIGHT RADIOMETRIC CALIBRATION

Calibration of all bands is a requirement of many users. Two classes of calibration source are involved, the visible/near infrared and the thermal. The best source for the visible/infrared spectral bands is still the tungsten quartz-halogen bulb (sometimes with integrating sphere or diffusing panel). Unfortunately, the bulbs blacken with use. The bulbs are "seasoned" or pre-aged and their output plotted with time. When the curve flattens somewhat, one hopes that changes are predictable by curve extrapolation. It is felt by many instrument designers that the silicon detectors and their preamplifiers are more stable than the source used to calibrate them. A possible solution is to include extra lamps for calibration checks of the "working" calibration lamp. Since the lamp used to check the aging of the working calibration lamp is itself only used occasionally, it will not age appreciably. Various optical means could be designed to introduce either source alternately or sequentially into the optical path. Perhaps the best method is to use a "polka dot" achromatic beam sharing (50% beamsplitter) mirror which transmits or reflects equally and is not likely to degrade in space. Such a beamsplitter

was used successfully by Honeywell on the Far Encounter Planet Sensor on the 1969 Mariner Mars mission. The beamsplitter only allows use of one or the other of the calibration lamps. Introduction into the pushbroom scanner optical system is best accomplished by a command motion of a folding mirror which is spring-loaded for fail-safe operation.

Calibration of the thermal band requires blackbody sources of controlled temperature. Honeywell has successfully flown such sources on the Skylab S192 Multispectral Scanner for NASA, JSC. The essential requirement of such a calibration source is that it has a stable emissivity and a stable known temperature. A stable emissivity is achieved by making the geometric form of the blackbody cavity the prime determining influence on emissivity so that postulated changes in emissivity of a high-emissivity surface coating will have only minor influence. Cavities are usually made of OFHC high purity copper and several temperature monitoring transducers are included on and within the blackbody. Both heating and cooling can be employed, but active cooling is not as reliable as heating.

D.8 SUMMARY AND RECOMMENDATIONS

The pushbroom version of a thematic mapper is a viable and attractive candidate system for missions in the post 1978 period. Development is required on photovoltaic mercury cadmium telluride arrays, on arrays of integrated field effect preamplifiers, and on charge coupled device multiplexers for all arrays. Optics and mechanical design tasks are difficult but feasible. Two two-foot aperture reflective Schmidt telescopes will be expensive and difficult to make. An oscillating mechanically resonant vane chopper is worthy of development to provide dc restoration. Performance of the 24-inch Pushbroom Thematic Mapper is excellent. The IFOV of the thermal band matches that of the other ten bands. Even though the scanner provides 30 meter ground resolution in all bands, the thermal channel still provides a 0.50°K NEΔT at 50% MTF when viewing a 250°K blackbody ground target. The 24-inch diameter aperture requirement was seen to result from diffraction influence on MTF in the thermal band. If resolution requirements are relaxed for this band, the aperture may be reduced. The device will fit within a 36-inch diameter by 72-inch long cylinder. Because of its attractions, the pushbroom multispectral scanner is worthy of further development.